

**Dissertation**

submitted to the

Combined Faculties of the Natural Sciences and Mathematics  
of the Ruperto–Carola-University of Heidelberg. Germany

for the degree of

Doctor of Natural Sciences

Put forward by

M.Sc. Yong Zhao

born in: Tianjin, Peoples Republic of China

Oral examination: 18th Nov. 2009



# Resonance Fluorescence and Electron Spin in Semiconductor Quantum Dots



Referees: Prof. Dr. Jian-Wei Pan  
Dr. Mete Atatüre



# Zusammenfassung

## Resonante Fluoreszenz und Elektronenspin in Halbleiter Quantenpunkten

In dieser Dissertation wird die erste Beobachtung von spinabhangiger resonanter Fluoreszenz eines einzelnen Quantenpunktes vorgestellt, sowie ihre Anwendung fuer die Bestimmung der Dynamik von Elektronenspins aufgezeigt.

Das Mollow-Triplett und das Mollow-Quintuplett, Kennzeichen resonanter Fluoreszenz, zeigen sich in dem nicht-spinaufgeloesten, respektive spinaufgeloesten resonanten Fluoreszenz-Spektrum. Ein vernachlaessigbarer Laserhintergrund, ein fast nur radiativ linienverbreitertes Spektrum sowie Photon Antibunching implizieren dass die Seitenband-Photonen hintergrundstrahlungsfreie und nahezu transformlimitierte einzelne Photonen sind. Dies ist ein vielversprechender Schritt in Richtung der Erzeugung einzelner Photonen und Bestimmung des Elektronenspins.

Anstatt das Spektrum aufzuloesen, wird ein alternativer Weg gezeigt den Elektronenspin auszulesen, welcher auf Photon Zaehlung der resonanten Fluoreszenz bei moderater Laserleistung beruht. Die Elektronenspindynamik wird mithilfe n-mal wiederholter zeitlich aufgeloester resonanter Fluoreszenz gemessen, um die Rueckwirkung der Messaktion auf den Elektronenspin sowie die Elektronenspinrelaxation zu bestimmen. Hyperfeinwechselwirkung und „Hole Mixing“ von leichten und schweren Loechern werden als die relevanten Mechanismen fuer die Rueckwirkung identifiziert, waehrend phononunterstuetzte Spin-Orbit Wechselwirkung die Spinrelaxation dominiert. Nach einer detaillierten Diskussion von Spin-Ladungskonfigurationen in gekoppelten Quantenpunktsystemen wird die Spinbestimmung in einer Einzelmessung vorgeschlagen.

## Abstract

## Resonance Fluorescence and Electron Spin in Semiconductor Quantum Dots

The work presented in this dissertation contains the first observation of spin-resolved resonance fluorescence from a single quantum dot and its application of direct measurement of electron spin dynamics.

The Mollow triplet and the Mollow quintuplet, which are the hallmarks of resonance fluorescence, are presented as the non-spin-resolved and spin-resolved resonance fluorescence spectrum, respectively. The negligible laser background contribution, the near pure radiative broadened spectrum and the anti-bunching photon statistics imply the sideband photons are background-free and near transform-limited single photons. This demonstration is a promising step towards the heralded single photon generation and electron spin readout.

Instead of resolving spectrum, an alternative spin-readout scheme by counting resonance fluorescence photons under moderate laser power is demonstrated. The measurements of n-shot time-resolved resonance fluorescence readout are carried out to reveal electron spin dynamics of the measurement induced back action and the spin relaxation. Hyperfine interaction and heavy-light hole mixing are identified as the relevant mechanisms for the back action and phonon-assisted spin-orbit interaction dominates the spin relaxation. After a detailed discussion on charge-spin configurations in coupled quantum dots system, the single-shot readout on electron spin are proposed.

---

# Preface

That was three years ago, my colleagues in Heidelberg demonstrated the first six-photon entanglement [1], meanwhile they approached the bottleneck on the brightness and fidelity of generating multiphoton entanglement through spontaneous parametric down conversion due to its probabilistic nature. In order to continue the legend of photonic qubits in implementing quantum information processing, the quantum memory and deterministic indistinguishable single photon source are expected. Since then, I started my PhD and chose to pursue the single photon generation from solid state system, especially the semiconductor quantum dots. To the end of this period, there turns out more than what I predicted. Photon, electron and the mesoscopic environment, they all come into the picture, make the role of quantum dots as the interface of flying qubits (photons) and stationary qubits (electrons) more and more vivid, and also bring me much more joy of research.

Before I started in this field, there has been plenty of work demonstrated that quantum dot can emit single photons, especially from single InAs/GaAs self-assembled quantum dots [2, 3, 4]. However the issue about how to make the photons indistinguishable, which is the crucial precondition for multiphoton manipulation, was still there [5, 6]. Although using photons generated from same quantum dot can fulfill the conditions of same central frequency, same bandwidth and same polarization which are required for being indistinguishable, the uncontrolled time jitter on the photon emission times, due to the nonradiative relaxation of excitons down to the lowest quantum dot state, diminishes the coherence of the emitted photons, makes the photons still distinguishable. A common feature in all the previous studies is the incoherent pumping of the transitions through optical exciton generation in either the host matrix such as GaAs or the quasi-continuum states above the higher lying confined states of the quantum dot. In an attempt to address this shortcoming, our attention focused on the resonant optical excitation of quantum dots, and it excitingly brought us our first result, spin-resolved resonance fluorescence [7], after

---

one year lab building in Cavendish. The resonance fluorescence photon is expected to be transform limited, i.e. follow the mechanism of pure radiative broadening, but our observation suggested about 80MHz upper-bound dephasing, which may come from the interactions between electron spin states to their mesoscopic environments, such as nuclear spin ensemble. More understanding of physics behind are required before we move on to any further single photon applications. Therefore, we pull back to carefully study the electron spin dynamics using new fluorescence technique we developed. It turns out the n-shot resonance fluorescence spin readout is much more powerful than traditional differential transmission measurement. However, in the single quantum dots system, the fast measurement induced back action is the obstacle for us to pursue the single-shot spin readout. Recently, we upgraded our system to coupled quantum dots, which opens up the exact way towards the single-shot spin readout using resonance fluorescence with the suppressed back action. Moreover, the coupled quantum dots system bring us some other new ideas such as the coherent generation of photon pairs and photon-electron entanglement base on two-qubit gate.

This thesis contains five chapters. *Chapter 1* is an introduction chapter, where the concept and basic optical properties of self-assembled InAs/GaAs quantum dots are presented. Photoluminescence and differential transmission are the main experimental technique for this chapter. In *Chapter 2*, we investigate resonance fluorescence spectrum of Mollow-triplet and Mollow-quintuplet. The single photon generation based on electron spin state is also discussed. *Chapter 3*, as one direct application of resonance fluorescence technique, we perform N-shot measurements to reveal electron spin dynamics in single quantum dots. *Chapter 4* is devoted to the study of coupled quantum dots, where theoretical model and current experimental progress are presented. An outlook is given in *Chapter 5*.



# Contents

<b>Abstract</b>	<b>i</b>
<b>Preface</b>	<b>iii</b>
<b>Contents</b>	<b>v</b>
<b>1 Quantum Dots — from cleanroom to quantum optics laboratory</b>	<b>1</b>
1.1 Growth of self-assembled quantum dots . . . . .	2
1.1.1 Self-assembly of single quantum dots . . . . .	2
1.1.2 Stacking of quantum dots . . . . .	4
1.2 Excitonic states and optical transitions . . . . .	5
1.2.1 The optical spectrum in single quantum dots. . . . .	5
1.2.2 Deterministically charging quantum dots . . . . .	7
1.2.3 Spins in single quantum dots . . . . .	10
1.2.4 Differential transmission . . . . .	11
<b>2 Spin-resolved resonance fluorescence from single quantum dots</b>	<b>15</b>
2.1 Resonance fluorescence in two-level atomic system . . . . .	16
2.1.1 Two level system driven by optical field . . . . .	16
2.1.2 Correlation functions of resonance fluorescence . . . . .	17
2.1.3 Fourier transform of the time dependent correlation function .	19
2.1.4 Dressed state picture . . . . .	21
2.2 Experimental setup and control abilities . . . . .	23
2.2.1 General optics . . . . .	23
2.2.2 Laser frequency and power control . . . . .	24
2.2.3 High resolution spectrometer . . . . .	26
2.2.4 Second order correlation function and lifetime setup . . . . .	27

2.3	Quantum dot spin-resolved resonance fluorescence . . . . .	27
2.3.1	Mollow triplet under laser power control . . . . .	28
2.3.2	Mollow triplet under laser frequency control . . . . .	31
2.3.3	Spin-selective dynamic Stark effect and Mollow quintuplet . . .	32
2.3.4	Photon correlation of resonance fluorescence . . . . .	35
2.4	Single photon generation and other applications . . . . .	36
2.4.1	Single photon generation . . . . .	36
2.4.2	Other applications . . . . .	37
<b>3</b>	<b>Direct electron spin readout in single quantum dots by resonance fluorescence</b>	<b>39</b>
3.1	Probing two-level system by counting resonance fluorescence photons	40
3.2	Environmental couplings of electron spin in single quantum dot . . .	42
3.2.1	Coupling of confined electron spin with nuclear-spin reservoir .	42
3.2.2	Coupling of confined electron spin with phonon reservoir . . .	44
3.2.3	Coupling of confined electron spin with Fermi sea . . . . .	45
3.2.4	Hole mixing . . . . .	46
3.3	Direct measurements of quantum dot spin dynamics . . . . .	46
3.3.1	Optically induced back action on electron spin — Spin pumping	47
3.3.2	Observed electron spin relaxation in single quantum dot . . .	53
3.3.3	Towards single-shot measurement of an electron spin . . . . .	55
<b>4</b>	<b>Charge and spin configurations in coherently coupled quantum dots</b>	<b>59</b>
4.1	Samples and methods . . . . .	60
4.2	The basic interactions . . . . .	62
4.2.1	One-electron ground states: $1e$ system . . . . .	62
4.2.2	Two-electron ground states: $2e$ system . . . . .	63
4.2.3	Direct and indirect excitons: $1e1h$ system . . . . .	67
4.3	Optical Transitions of the Multi-charge System . . . . .	72
4.3.1	Doubly charged exciton: $3e1h$ system . . . . .	72
4.3.2	Singly charged exciton: $2e1h$ system . . . . .	77
4.4	The gate-voltage map for charge and spin configurations in CQDs . .	84

<b>5 Outlook</b>	<b>87</b>
5.1 Towards single-shot measurement of an electron spin . . . . .	87
5.2 Probing nuclear-spin dynamics using resonance fluorescence . . . . .	89
5.3 More in the near future . . . . .	91
<b>Summary</b>	<b>93</b>
<b>Bibliography</b>	<b>95</b>
<b>List of figures</b>	<b>103</b>
<b>List of Tables</b>	<b>107</b>
<b>List of publications</b>	<b>109</b>
<b>Acknowledgement</b>	<b>111</b>



## Chapter 1

# Quantum Dots — from cleanroom to quantum optics laboratory

In the past decade, physical properties of low-dimensional solid-state structures is a field under intense study. This is because the gained knowledge is essential as the feature sizes of manufacturable semiconductor devices decrease, and also hold great promise as quantum systems with applications in the cutting-edge field of Quantum Information Processing (QIP). Among them, a zero-dimensional system, self-assembled quantum dot (QD) attracts more and more attention, which can provide three-dimensional confinement of carriers, show atom-like properties such as the discrete electronic states, strong photon antibunching [3, 4] and near transform-limited fluorescence [7, 8, 9, 10]. Moreover, the quantum dots (QDs) intrinsically locate within the matrix of the surrounding materials, and naturally form a potential trap for the electrons and holes. By integrating the diode structure onto the sample, we can deterministically charge the QDs and tune the interactions between electronic states. With the developed quantum optics techniques, a concept of the all-optically controlling[11, 12, 13, 14] and detecting[15, 16, 17] carriers' spin states in single QD has been widely demonstrated. In this chapter, we will firstly discuss the growth of self-assembled QDs, and then study the basic optical properties in QD by using photoluminescence (PL) and differential transmission (DT) technique. Both of them are carried out at the cryogenic temperature of about 4.2 K in either Helium flow cryostat or Helium bath cryostat.

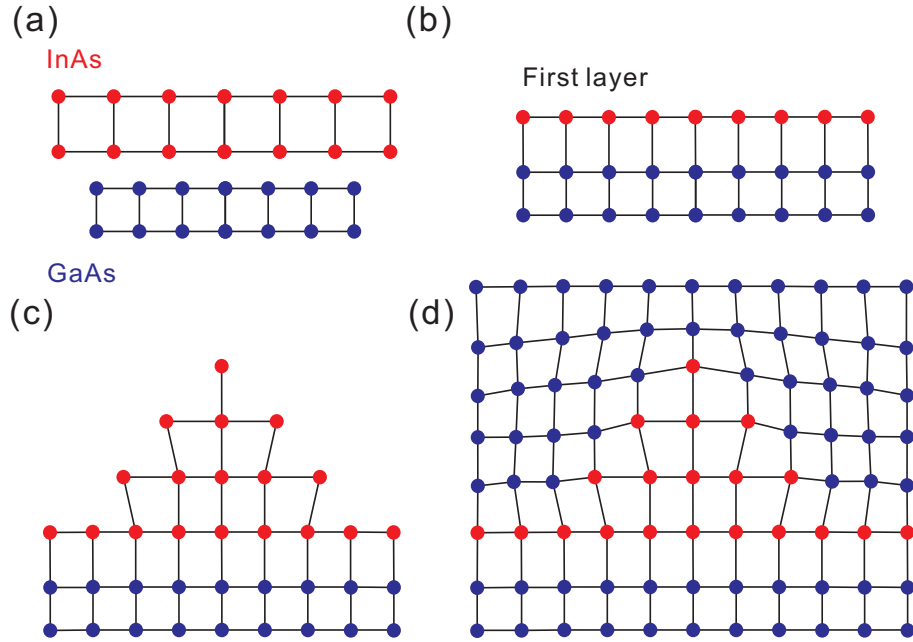
## 1.1 Growth of self-assembled quantum dots

The potential for an electron in the conduction band is given by the band edge, so is the potential of a hole in valence band. In this way, different materials can be combined to create a potential that is varying in space. In particular, a low-band-gap semiconductor in a larger band-gap semiconductor results in a trapping potential for the carriers. This is realized with semiconductors in a so called heterostructure. Depending on the hetero-structure trapping potential size, quantization effects occur.

### 1.1.1 Self-assembly of single quantum dots

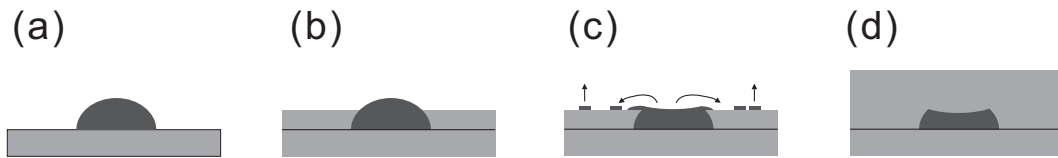
QDs are heterostructures of reduced dimensionality down to zero, providing three dimensional confinements in real space, while still maintaining the mesoscopic structure. Remarkably, this ultimate spacial confinement can be formed naturally by self-assembly in a strain-driven phase transition that takes place when combining two materials of different lattice constants during one material growth protocol. The particular materials covered in this work are Indium Arsenide (InAs) as the micro-crystallite islands and Gallium Arsenide (GaAs) as the surrounding matrix. There is 7% lattice constants mismatch between these two materials (Fig. 1.1 (a)). Applying molecular beam epitaxy (MBE) technique, crystal is grown through monolayer-by-monolayer formation of thin epitaxial films. As illustrated in Fig. 1.1 (b-c), in the Stranski-Krastanow growth mode [18], the growth initially occurs in forming the so-called *wetting layer* (Fig. 1.1 (b)). After the deposition of a few monolayers, the critical thickness is reached and the phase transition begins (Fig. 1.1 (c)). This growth mode is employed for growing QDs allowing relaxation of strain energy by island formation without dislocations. After the nucleation of the InAs island, the sample is annealed for 30 s at 545°C followed by GaAs overgrowth at the same temperature with at least 15 nm of capping layer (Fig. 1.1 (d)). The growth temperature can then be raised to its normal value for additional capping-layer deposition.

However, a practical difficulty for optical studies of InAs QDs in GaAs is the energy of the emitted photons which is lower than or close to the bandgap energy of silicon. This excludes the use of Si CCD cameras for detection of the luminescence. It turned out to be very practical to blue-shift the emission wavelength by adding annealing steps during the capping of the islands. Among the techniques developed



**Figure 1.1:** Illustrated formation of self-assembled InAs/GaAs QDs. (a) Lattice constants for InAs and GaAs. (b) The first layer growth of two materials, the wetting layer is about 1.7 mono-layers. (c) Nucleation of the InAs island. (d) Capping InAs island by GaAs.

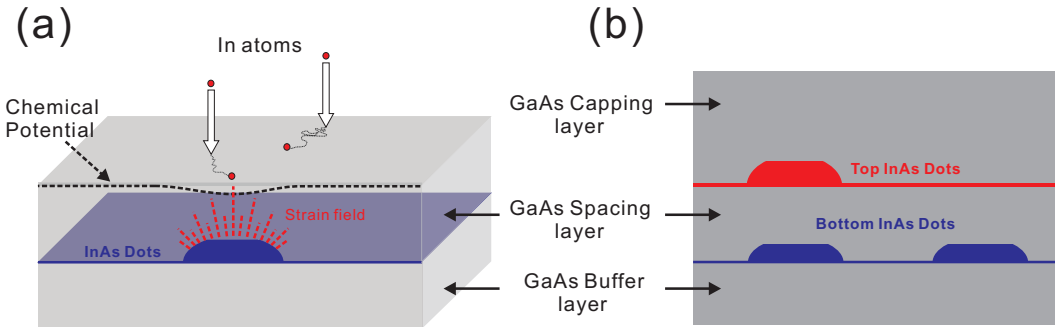
for this purpose, the partially covered island (PCI) [19] technique is used on the QDs covered in this work. The basic PCI process is shown in Fig. 1.2. After the annealing step mentioned above, a thin GaAs layer is grown for partially capping island and annealed once more for another 30s. The top section of the island diffuses onto the overgrown GaAs layer re-wetting the surface. The annealing allows for the evaporation of this local wetting layer and the re-melting of the island. The main results of this process are a decrease of the island height and an intermixing between Indium and Gallium.



**Figure 1.2:** Schematic diagram of the steps in the PCI technique for blue-shifting the emission from QDs. (a) The growth is interrupted after the nucleation of InAs island. (b) The InAs island is partially covered by a thin layer of GaAs. (c) Additional annealing process allows the InAs to reflow onto the new surface and evaporate shortly, thereby decreasing the thickness of the island. Finally, (d) the QD is capped completely.

### 1.1.2 Stacking of quantum dots

Recently, coupled quantum dots (quantum dot molecules) attracted more attention due to the much richer optical and electrical properties induced by either electron-electron coupling interactions or hole-hole coupling interactions, which benefit more sophisticated quantum control applications compared to single QDs system. The coupled quantum dots (CQDs) covered in Chapter 4 are the vertically stacked self-assembled QD pairs, which are grown by using self-aligning technique. This technique allows the sequent dots layer has the nucleation preferably on top of the QDs of the previous layer.



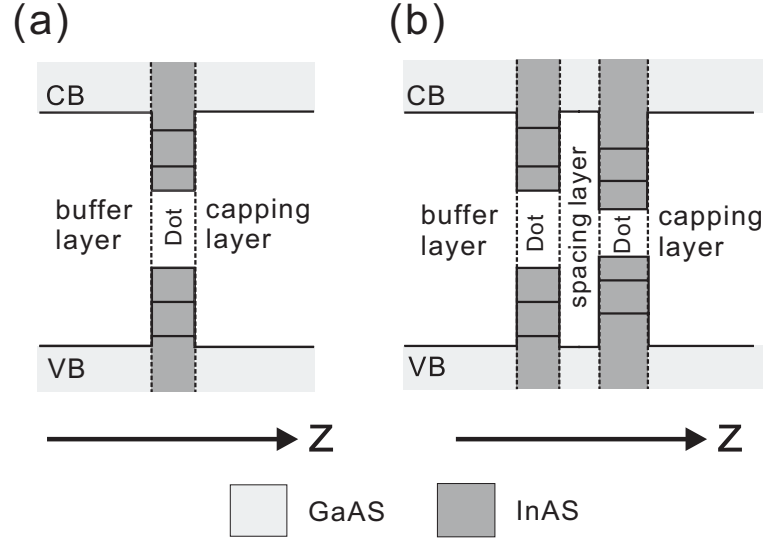
**Figure 1.3:** Schematic diagram of the stacking of quantum dots. (a) Self-aligning stacking process. The surface chemical potential (black dotted line) is decreased due to the strain field (red dotted line) induced by the buried QD. (b) QDs from top layer stacked onto QDs from bottom layer with certain probability.

Figure 1.3 shows a schematic view of the stacking of QDs. The larger lattice constant of InAs relative to bulk GaAs gives coherently strained islands. The strain in these islands is compressive, leading to tensile stress in the GaAs surrounding the island. The strain field (red dashed line in Fig. 1.3 (a)) on the surface of the spacer layer is maximum on top of the buried QD. This stress field reduces the surface chemical potential (black dashed line in Fig. 1.3 (a)) of InAs and seeds the nucleation: as an In adatom is physisorbed on the surface, it diffuses until it is chemisorbed on the most favorable site. The QDs in top layer are intrinsically bigger than bottom layer due to the preferable nucleation. We normally keep the top QDs layer optically red shifted with respect to the bottom QDs layer, even with PCI growth. We indicate the QDs from two layers with blue and red color as shown in Fig. 1.3 (b). The probability of stacking decreases with the thickness of the spacing layer increasing.



## 1.2 Excitonic states and optical transitions

Due to the 3D quantum confinement, the typical electronic band structure of semiconductor material is fully quantized to be discrete energy levels within QD region. The self-assembled QDs with PCI process covered in this thesis are lens-shaped with the in-plane diameter  $\sim 20$  nm and height  $\sim 4$  nm along crystal growth axis (defined as “z” axis), therefore the z-quantization energy largely exceed the in-plane quantization energy, so that the discrete energy level in QD is dominated along z direction. Figure 1.4 presents the typical diagram to indicate QD band structure along z direction. Not only the quantized band structure, the strain profile also takes part in determining the quantum dot states. Moreover the Coulomb interaction between the quantum confined carriers has to be taken into account.



**Figure 1.4:** Band structure diagram for single QD (a) and coupled QDs (b), respectively. The z direction corresponds to the vertical direction in Fig. 1.2 and Fig. 1.3. “CB” is the abbreviation for “Conduction Band” and “VB” is for “Valence Band”.

### 1.2.1 The optical spectrum in single quantum dots.

The lowest-lying optical transitions can be experimentally studied by using photoluminescence (PL) technique, which has been widely used in the field of QD spectroscopy within the last decade. Figure 1.5 illustrates the typical process of the PL measurements. The excitation laser with photon energy larger than the band gap of GaAs, creates electron-hole pairs in the host material. For seeking the lowest energy states, electrons and holes relax into QD region through non-radiative process and

end up at lowest states of conduction band and valence band respectively with the time scale about several tens of picosecond. Consequently, a recombination happens between paired electron and hole and result in a single photon emission with the time scale about several hundreds of picosecond.

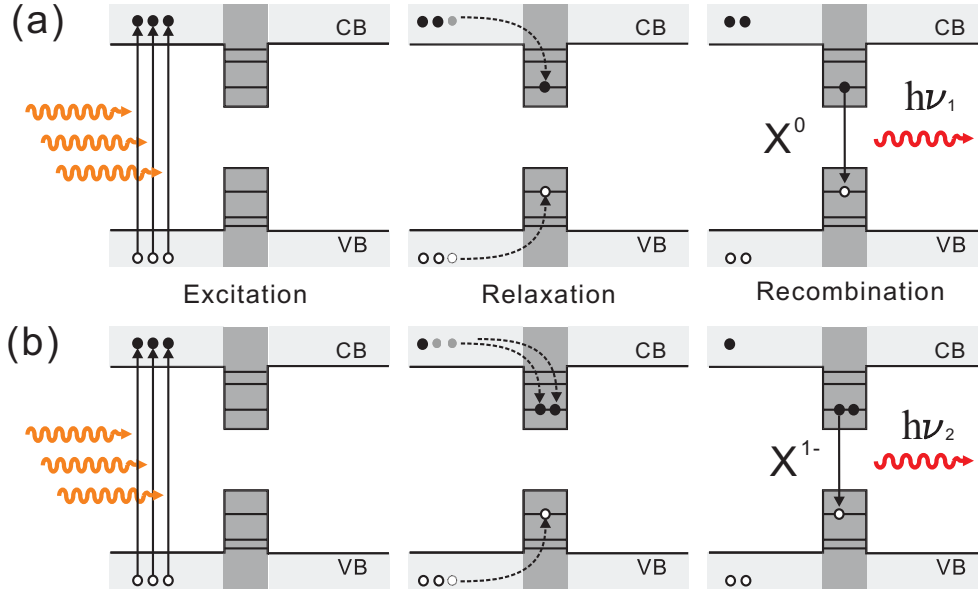


**Figure 1.5:** Processes in a photoluminescence experiment with (a) an exciton ( $X^0$ ) in single QD and (b) a trion ( $X^{1-}$ ) in single QD.

The non-radiative relaxation can lead to different charge configurations within QD. With the case that QD traps one electron and one hole, which are bound together with Coulomb interaction forming a quasi-particle “exciton” ( $X^0$ ), the photon emitted with frequency  $\nu_1$  through recombination as illustrated in Fig. 1.5 (a). With the case that QD traps two electron and one hole, the recombination of quasi-particle “trion” ( $X^{1-}$ ) gives photon with different frequency  $\nu_2$  due to the different Coulomb interaction from  $X^0$  case as illustrated in Fig. 1.5 (b). Other configurations, such as positive trion ( $X^{1+}$ ) with two holes and one electron and “Biexciton” ( $XX$ ) with two electron-hole pairs, have their characteristic emission frequencies as well. This frequency shift due to the Coulomb interaction is named as *Coulomb Renormalization*, and used to identify the charge states of QD. One typical PL spectrum of single QD is shown in Fig. 1.6. The *Coulomb Renormalization* is also the key feature used for selecting certain emission in traditional single photon generations [3, 4].

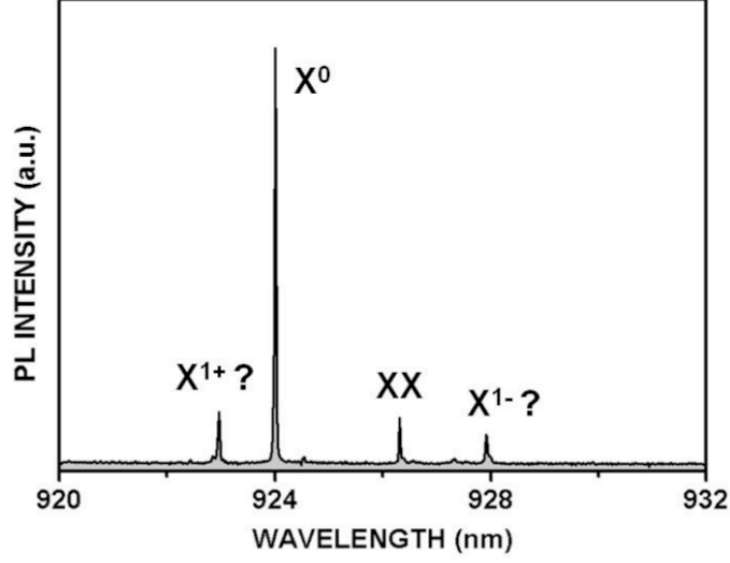


**Figure 1.6:** Typical photoluminescence spectrum from a single quantum dot with tentative identification of transitions, cited from [20]

### 1.2.2 Deterministically charging quantum dots

In order to eliminate the uncertainty of the charge states in QD as the tentative identification shown in Fig. 1.6, we incorporate the QD samples discussed above into the intrinsic part of a n-i-Schottky diode structure [21]. By tuning the electric field over the QDs, we realized the deterministic control of their charge states.

We show the cross-section of the gated single-layer QD sample in Fig. 1.7 (a). Differently from the samples we discussed above, one highly n-doped GaAs layer, as the electron sea as well as the part of the gate structure, need to be grown below the InAs QDs layer, with an intrinsic GaAs layer as the electron tunneling barrier in between. The diode structure consists of a back contact and a Schottky window, which are fabricated after the MBE growth. The back contact is processed by, firstly wet-etching a certain area of the sample from the surface down to a certain depth before touching n-doped layer, secondly, evaporating alloy (Ni, Au, Ti) into the etched region, and thirdly annealing the alloy so that the alloy can reach the n-doped layer by diffusing and forming an ohmic contact which provides linear and symmetric voltage-current (V-I) characteristics between the different attached materials. The Schottky window is one semi-transparent Titanium layer ( $\sim 4$  nm thickness) directly evaporated onto the GaAs surface functioning as the top contact without annealing. For compensating the different work functions of different materials, the

direct attaching of metal-semiconductor for Schottky window results in a negative potential barrier ( $\sim -0.7$  V) respect to the Fermi level of the back contact. The intrinsic semiconductor layers between the two contacts is about 200 nm thick in the samples covered here, therefore the response of the band structure to the potential difference is treated linearly.

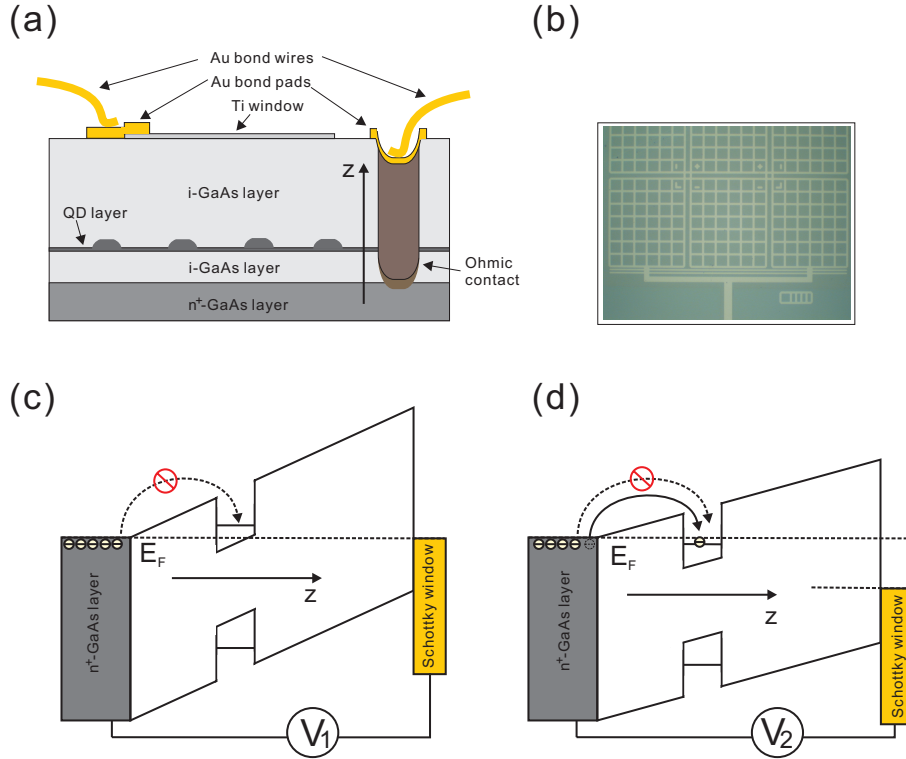


**Figure 1.7:** Schematic of the charge controlling device. (a) the cross section diagram of the n-i-Schottky diode structure. (b) The microscope picture for the gold grids structure fabricated on top of the titanium Schottky window, for mapping the sample surface and marking the working QD in-plane locations. The minimum square box indicates an area of  $20\mu\text{m} \times 20\mu\text{m}$ . (c) and (d) band structure diagram for gated sample. (c) the voltage  $V_1 = 0$ , QD is favorable for non electron residence, (d) the voltage  $V_2 > V_1$ , where QD is favorable for single electron residence.

By applying DC gate voltage to the diode structure, we can tune the quantized energy levels of QDs respect to the Fermi level of the electron sea. When the QD levels are above the Fermi level, the QDs remains empty (Fig. 1.7 (c)). At a different voltage the QD levels are tuned below the Fermi level and it is energetically favored to have an electron trapped in (Fig. 1.7 (d)). Moreover, the confinement-induced Coulomb interaction strongly inhibits the tunneling of an additional electron into the quantum dot, unless the extra cost of charging energy ( $\sim 20$  meV) is provided by means of energy level difference. As a result, the different charge states correspond

to different voltage ranges, which are utilized to deterministically control the charge number in QDs.

Figure 1.8 (a) presents the typical discrete steps in the PL spectrum where essentially only one type of emission is linked to a particular charge configuration at any given gate voltage value. However, in some cases, although the QDs are indeed deterministically charged, depending on the thickness of the tunneling barrier between the n-doped layer and QDs, as well as the power of above-band-excitation laser, PL does not present the one-to-one map between the spectra and the charge states as an example shown in Fig. 1.8 (b). The competition among the mechanisms of electron tunneling, charge relaxation and charge recombination determines the PL behavior. With thick tunneling barrier and high excitation power, the electron tunneling rate is not fast enough to equilibrium the trapped electrons with the Fermi sea of back contact before the charge relaxation and recombination, the overlap of the PL charge plateaus happens. However, if the excitation is resonant with the lowest excited QD levels, no electron-hole pair generated somewhere else but at these levels, the initial equilibrium charge states determine the transitions, so that the plateau overlap, i.e. the uncertainty of the charge states, can be eliminated.

All the charge plateaus in Fig. 1.8 have slopes which are due to the DC-Stark shift of the permanent dipole in a linearly varying electric field.

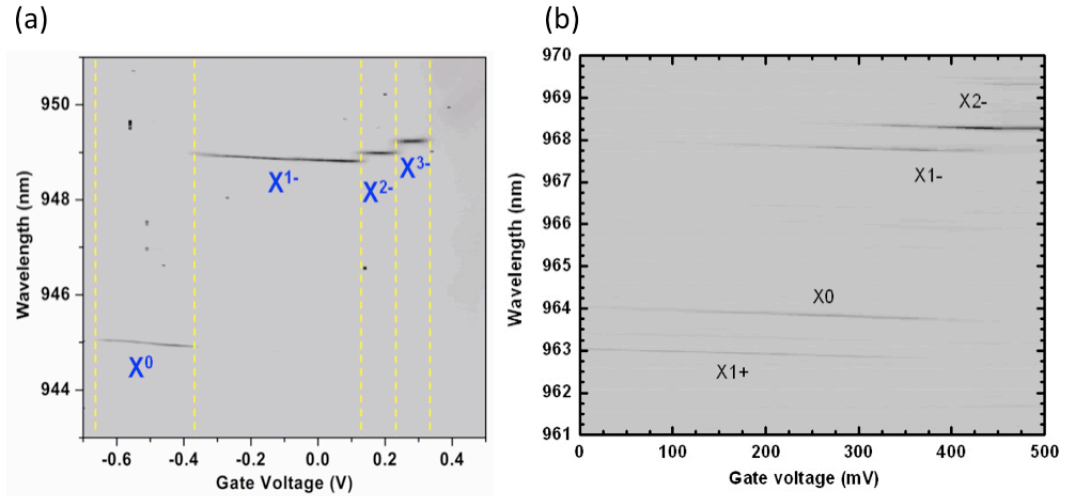


**Figure 1.8:** Voltage sweep of photoluminescence spectrum for different samples. Both present voltage dependent behaviors. (a) presents clear one-to-one map between charge plateaus and voltage ranges, cited from [22], (b) presents the big overlap of charge plateaus due to the different sample growth and excitation parameters.

### 1.2.3 Spins in single quantum dots

As we learnt from the PL measurements discussed above, each optical transition corresponds to a particular charge configuration, moreover, it also carries the information of spin for all the charge carriers involved. Electrons' wavefunctions in lowest conduction band have s-wave symmetry sustaining a twofold spin-degeneracy of  $(S_e, S_{e,z}) = (1/2, \pm 1/2)$ . On the other hand, wavefunctions in highest valence band have p-wave symmetry sustaining sixfold pseudo-spin-degeneracy formed by quadruplet of  $(J_e, J_{e,z}) = (3/2, \pm 3/2 \pm 1/2)$  and doublet of  $(J_e, J_{e,z}) = (1/2, \pm 1/2)$ . However, the doublet is dramatically separated from the quadruplet due to the spin-orbit coupling, forming so called spin-orbit levels. Further splittings also happen within the quadruplet, where the degeneracy is lifted since heavy hole ( $J_{h,z} = -J_{e,z} = \pm 3/2$ ) and light hole ( $J_{h,z} = \pm 1/2$ ) experiencing different strain confinement due to their different effective masses.

According to the optical selection rules, which require the angular momentum transferred to single photon is  $M_z = \pm 1$ , the recombination can only be allowed between the electron with spin  $S_{e,z} = -1/2$  ( $S_{e,z} = 1/2$ ) in the conduction band and the hole with pseudo-spin  $J_{h,z} = 3/2$  ( $J_{h,z} = -3/2$ ) in valence band. The electron-hole pairs with  $M_z = S_{e,z} + J_{h,z} = \pm 1$  form twofold “bright” excitons, on the other hand, the electron-hole pairs with  $M_z = S_{e,z} + J_{h,z} = \pm 2$  form twofold “dark” excitons which do not result in recombination. Moreover, for neutral excitonic state  $X^0$ , there are nonzero electron-hole spin exchange interactions that firstly lift the energetic degeneracy of the bright and dark states forming separate subspaces and secondly mix the states in each subspace [23] leading to further level splitting as the fine structures. For example, in the twofold bright-exciton subspace, the new eigenstates are two superposition states of original degenerate states with  $|M_z\rangle = |\pm 1\rangle$ , which result in the lift of level degeneracy and the change of emission polarization from circular ( $\sigma_+ : |1\rangle$ ,  $\sigma_- : |-1\rangle$ ) to linear ( $x : |1\rangle + |-1\rangle$ ,  $y : |1\rangle - |-1\rangle$ ). Details about spin exchange interactions for neutral exciton will be discussed in Chapter 4. For charged exciton, such as trion  $X^{1-}$ , because of the pairing of the electrons, the total spin for electron pair is zero and the spin exchange interactions are shielded.

The resonant excitation is the reverse of recombination, moreover it is the direct way to address the optical transition without any non-radiative relaxation. During the process, the electron from the valence band is excited to conduction band and leave a hole behind in the valence band. The generated electron-hole pairs have the

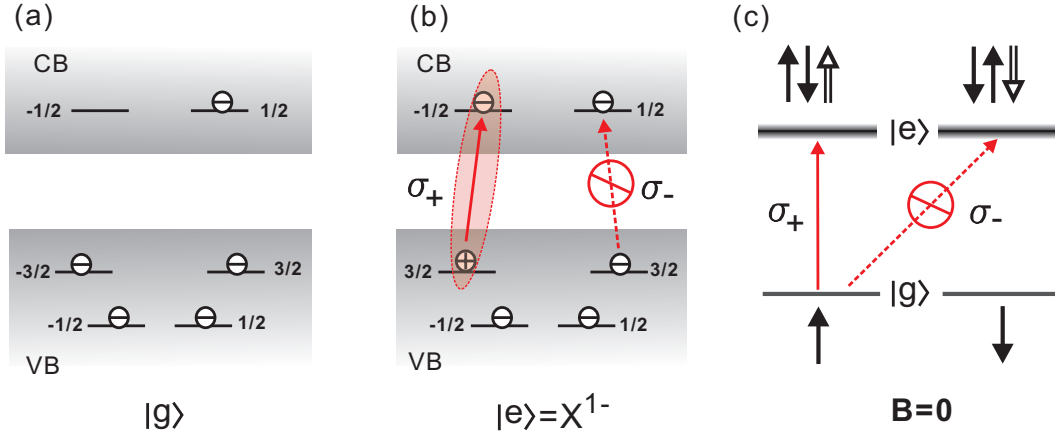


**Figure 1.9:** Resonant excitation of singly charged QD. (a) The initial state of QD is single electron with spin state  $|g\rangle = |1/2\rangle = |\uparrow\rangle$ . (b) The excited state of QD is trion state with total spin state  $|e\rangle = |3/2\rangle = |\uparrow\downarrow\uparrow\rangle$ . (c) The level diagram indicates the excitation.

total spin states  $|M_z = \pm 1\rangle$ , but no dark excitons can be generated. For the case of one electron charged QD initial states, the optical allowed transitions are strict with the initial spin states of electrons. Taken initial state of electron  $|1/2\rangle$  (indicated as  $|\uparrow\rangle$ ) as an example, as shown in Fig. 1.9 (a), the excited electron can only reach  $|-1/2\rangle$  (indicated as  $|\downarrow\rangle$ ) forming a trion  $X^{1-}$  ( $|\uparrow\downarrow\uparrow\rangle$ ) by absorbing  $\sigma_+$  polarized photon due to the *Pauli blockade* as shown in Fig. 1.9 (b) (c). Here, hole spin states  $|3/2\rangle$  and  $|-3/2\rangle$  are indicated as  $|\uparrow\rangle$  and  $|\downarrow\rangle$ , respectively.

The experimental techniques for resonantly studying QDs covered in this thesis are the “differential transmission” (DT) and the “resonance fluorescence”. We will finish this chapter by the following discussion about DT and start next chapter with resonance fluorescence.

#### 1.2.4 Differential transmission

In recent years, the differential transmission (DT) becomes a very powerful technique for resonantly studying the quantum dipole system. Especially on the studies of QDs. most of the recent significant studies on QD spins benefit from DT, such as [11, 12, 13, 16, 24, 17, 25, 26] for single electron spin, and [27, 28] for hole spin. Compared with the typical spectral resolution  $\sim 30\mu\text{eV}$  for PL, DT can provide high spectral resolution typically as 2 MHz ( $\sim 0.01\mu\text{eV}$ ) in our setup, which is crucial for resolving the lineshape of the QD transitions ( $\sim 2\mu\text{eV}$ ) and any other fine structures.

For measuring the transmission signal of single dipole like quantum dot, the

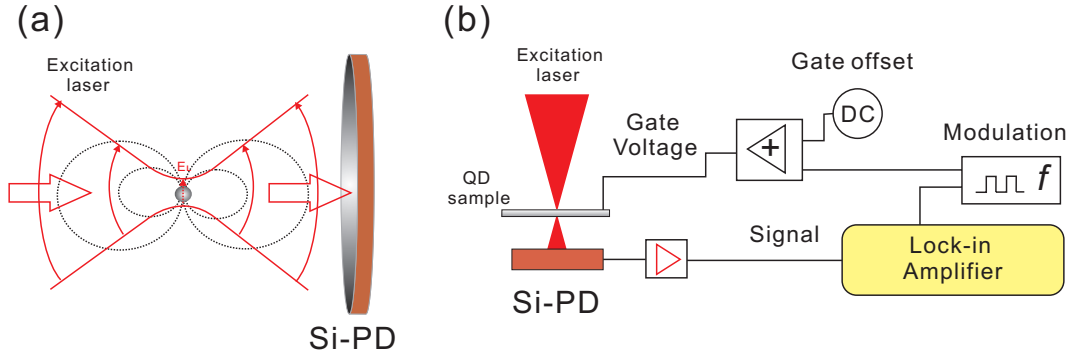


**Figure 1.10:** Detecting coherently scattered photons by differential transmission. (a) The illustration of detecting interference between the focused laser and the dipole field. (b) The schematic of the lock-in technique for detecting QDs transmission signal.

forward-scattered photons are in the single-photon level that is negligible compared with the laser background along the excitation axis. Intuitively, such small signal is difficult to be distinguished. However, there are two features of DT that make the small signal visible. The first one is the interference. As we will discuss the whole spectra of the resonance fluorescence in the next chapter, the scattered photons are consist of two components, the coherent part and incoherent part. The coherently scattered photons have the same spectral properties as the excitation laser, therefore they can interfere with the background laser, as we see in Fig. 1.10 (a). The total intensity of the light seen by the detector is:

$$I_{total} = I_L + I_{incoh} + I_{coh} + I_{ed}, \text{ with } I_{ed} \propto E_L E_{coh} f(\psi), \quad (1.1)$$

where  $I_L$ ,  $I_{incoh}$  and  $I_{coh}$  are the intensities of laser, incoherent scattered photons and coherent scattered photons, respectively.  $I_{ed}$  is the interference where the small amplitude of coherent photon can be amplified by laser amplitude with certain phase condition ( $f(\psi)$ ). A detailed study about transmission spectroscopy of QDs can be found in [29]. However, the coherent scattered photons only dominate the emission in weak excitation regime. From the calculation in [29], the transmission signal under weak excitation can be estimated as:

$$T = 1 - \alpha_0 \frac{\Gamma_{sp}^2}{4\Delta^2 + \Gamma_{sp}^2}, \quad (1.2)$$

where  $\alpha_0$  is the effective absorption strength,  $\Delta$  is the laser detuning respect to the QD transition,  $\Gamma_{sp}$  is the spontaneous rate. Experimentally, a significant challenge lies in the fact that  $\alpha_0$ , determined by laser focusing area and the dipole oscillating



strength, is typically with the order of 0.005. Considering the normal experimental noise floor, this small proportion signal is still difficult to be extracted. The second feature of DT is the lock-in technique, which can filter out the signal from the noisy environment. The schematic drawing of the lock-in detection is shown in Fig. 1.10 (b). According to the DC-Stark shift, the transition of QD can be turned on or off respected to the laser excitation by tuning the gate voltage applied on the sample. We modulate the gate with a square wave at a small frequency ( $\sim 2$  KHz) far away from the noise zoo in frequency domain, so that the transmission signal is only detected at the modulation frequency. A lock-in amplifier synchronized with the modulation is used to filter out and amplify the signal only at the set modulation frequency.

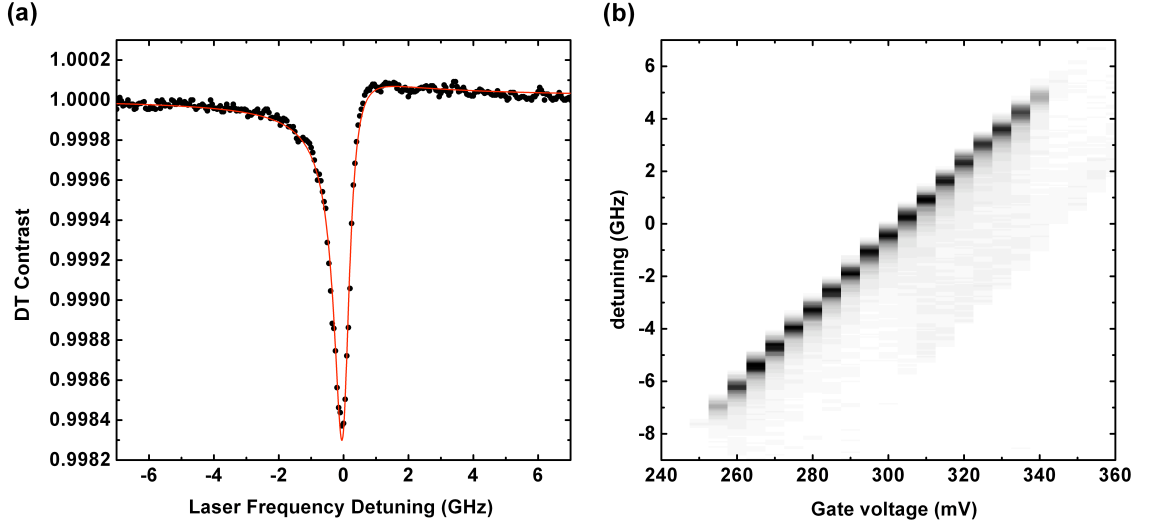


**Figure 1.11:** Typical DT data for  $X^{1-}$  transition. (a) 1D DT data obtained by scanning laser frequency across the QD transition with fixed gate offset. (b) 2D frequency-gate mapping of the  $X^{1-}$  plateau.

Figure 1.11 (a) shows one typical DT data for  $X^{1-}$  transition by scanning laser frequency with a fixed gate offset. The lineshape of transmission signal is not a symmetric Lorentzian but with a little dispersion, that is the result of the certain phase difference between two interfering fields. We fit the data with a detailed formula for the normalized total intensity:

$$I_{total}(\Delta) = 1 + A\mathcal{L}(\Delta) + B\mathcal{L}(\Delta)\left(\frac{2\Delta}{\Gamma} \cos \psi + \sin \psi\right), \quad (1.3)$$

where,

$$\mathcal{L}(\Delta) = \frac{1}{4\Delta^2 + \Gamma^2}$$

is a Lorentzian profile,  $\Gamma$  is the homogeneous linewidth.  $A$  and  $B$  are the extra fitting parameters. We fit out the phase  $\psi = 1.57$  rad and  $\Gamma = 574$  MHz. Figure 1.11 (b) is the 2D scan of  $X^{1-}$  plateau with the gate offset swept. The whole plateau has the frequency span about 13 GHz and gate span about 90 mV, the DC-Stark shift is then estimated as 144 MHz/mV.

So far, we have discussed the material structure and growth techniques of InAs/GaAs self-assembled QDs and their basic optical properties through PL and DT measurements. Especially DT is such a powerful tool which is the most mature technique in our lab and also widely used in most of the leading QD research groups around the world. It keeps producing interesting and significant work. However, we see its drawbacks. Firstly, DT signal relies on the interference between the photon and background laser, intrinsically, we don't have the access of the photon for further applications. Secondly, for extracting DT signal, modulation is added on the gate in our case, so during the measurements the QD transitions are constantly driven to jump back and forth, which limits further applications, for example one requires to continuously tune transitions by gate. Thirdly, the time resolution of DT readout is limited by time constant of lock-in amplifier and the modulation frequency, which limits the studies of any fast dynamics. For addressing those shortcomings, we are motivated to get access of the resonance fluorescence photons, it turns out to be our discussions in the following chapters.

## Chapter 2

# Spin-resolved resonance fluorescence from single quantum dots

In this chapter we report the first observation of spin-resolved photon emission from a resonantly driven QD transition. The hallmark of resonance fluorescence, i.e. the Mollow triplet [30] in the scattered photon spectrum when an optical transition is driven resonantly, is presented as a natural way to spectrally isolate the photons of interest from the original driving field. We go on to demonstrate that the relative frequencies of the two spin-tagged photon states are tuned independent of an applied magnetic field via the spin-selective dynamic Stark effect induced by the very same driving laser. This demonstration is a promising step towards the realization of heralded single photon generation for linear optics quantum computing, challenging tasks such as electron spin readout, and spin-photon entanglement. <sup>1</sup>

---

<sup>1</sup>This chapter is based on publication [3]

## 2.1 Resonance fluorescence in two-level atomic system

As a preparation of our experimental observations, we discuss basic understandings of resonance fluorescence (RFL) in two-level atomic system driven by the resonant or near resonant optical field in this section.

### 2.1.1 Two level system driven by optical field

As the singly charged QD discussed in chapter 1, under zero external magnetic field, the electron spin states are degenerate and as well as the two trion states, so that we have an effective two level system (states  $|e\rangle$  and  $|g\rangle$ ) with non-polarization selective transition (with frequency  $\omega = \omega_e - \omega_g$ ). The Hamiltonian of the system is written as

$$H = H_0 + H_I, \quad (2.1)$$

where  $H_0$  and  $H_I$  represent the unperturbed and interaction parts, respectively. By quantizing the QD electron system but classically treating the light field [31],  $H_0$  represents the atomic part  $H_0 = \hbar\omega_g|g\rangle\langle g| + \hbar\omega_e|e\rangle\langle e|$ , and  $H_I$  represents the interaction of atomic system with radiation field in dipole approximation:

$$H_I = -e\mathbf{x} \cdot \mathbf{E}(t) = -(\mathfrak{D}_{ge}|g\rangle\langle e| + \mathfrak{D}_{eg}|e\rangle\langle g|) \cdot \mathbf{E}(t), \quad (2.2)$$

where  $\mathfrak{D}_{ge} = \mathfrak{D}_{eg}^* = e\langle g|\mathbf{x}|e\rangle$  is the matrix element of the electronic dipole moment, and  $\mathbf{E}(t)$  is the field at the atomic system. If we assume a linearly polarized light field along x direction, we can write  $E(t) = \varepsilon \cos(\omega_L t)$ , and define the Rabi frequency as  $\Omega_R = |\mathfrak{D}_{ge}|\varepsilon/\hbar$ .

The further derivation of the Hamiltonian is to apply a unitary transform  $U(t) = \exp(-\frac{i}{\hbar}H_0 t)$  to the system, so that we can assign the time dependence of the state vector due only to the interaction energy. With the rotating wave approximation and in a frame rotating at the laser frequency ( $\omega_L = \omega + \delta$ ), the Hamiltonian of the system now reads:

$$H_s = \frac{\hbar\delta}{2}(|g\rangle\langle g| - |e\rangle\langle e|) + \frac{\hbar\Omega_R}{2}(|e\rangle\langle g| + |g\rangle\langle e|). \quad (2.3)$$

We use density matrix to describe the system state as:

$$\begin{aligned} \rho &= |\psi\rangle\langle\psi| \\ &= \rho_{gg}|g\rangle\langle g| + \rho_{ge}|g\rangle\langle e| + \rho_{eg}|e\rangle\langle g| + \rho_{ee}|e\rangle\langle e|. \end{aligned} \quad (2.4)$$

The motion of density matrix is given by Master equation

$$\dot{\rho} = -\frac{i}{\hbar}[H_s, \rho] + \mathcal{L}_{relax}[\rho], \quad (2.5)$$

which includes the Lindblad term which is the dumping term due to the coupling to the reservoir. In the case of two level system here, we consider the coupling to the vacuum mode fluctuation only, i.e. the spontaneous emission ( $\Gamma_{sp}$ ).

$$\mathcal{L}_{relax}[\rho] = \frac{\Gamma_{sp}}{2}(2\sigma_{ge}\rho\sigma_{eg} - \sigma_{ee}\rho - \rho\sigma_{ee}), \quad (2.6)$$

where  $\sigma_{ge} = \sigma_{eg}^\dagger = |g\rangle\langle e|$ , and  $\sigma_{ee} = |e\rangle\langle e|$ . Therefore, the motion equations for all the components of  $\rho$  are:

$$\dot{\rho}_{gg} = -\dot{\rho}_{ee} = \frac{i\Omega_R}{2}(\rho_{ge} - \rho_{eg}) + \Gamma_{sp}\rho_{ee}, \quad (2.7)$$

$$\dot{\rho}_{ge} = \dot{\rho}_{eg}^* = \frac{i\Omega_R}{2}(\rho_{gg} - \rho_{ee}) - (i\delta + \Gamma_{sp}/2)\rho_{ge}. \quad (2.8)$$

### 2.1.2 Correlation functions of resonance fluorescence

The coherent properties of the light emitted by a single atomic system in free space can be conveniently calculated with use of the source-field expression [32]. The electric field at point  $\mathbf{r}$  radiated by the atomic system at  $\mathbf{r}_0$  is given as:

$$\mathbf{E}(\mathbf{r}, t) = \mathbf{E}^+(\mathbf{r}, t) + \mathbf{E}^-(\mathbf{r}, t) \quad (2.9)$$

with retarded time term

$$\mathbf{E}^+(\mathbf{r}, t) = -\frac{e\omega_0^2}{4\pi\epsilon_0 c^2} \frac{\mathcal{D}_{ge} \cdot (\mathbf{r} - \mathbf{r}_0)}{|\mathbf{r} - \mathbf{r}_0|^2} \sigma_{ge} \left( t - \frac{|\mathbf{r} - \mathbf{r}_0|}{c} \right). \quad (2.10)$$

Using the field operator above, we derive the normalized first and second correlation functions as:

$$\begin{aligned} g^{(1)}(\tau) &= \frac{\langle \mathbf{E}^-(\mathbf{r}, t) \mathbf{E}^+(\mathbf{r}, t + \tau) \rangle}{\langle \mathbf{E}^-(\mathbf{r}, t) \mathbf{E}^+(\mathbf{r}, t) \rangle} \\ &= \frac{\langle \sigma_{eg}(t) \sigma_{ge}(t + \tau) \rangle}{\langle \sigma_{eg}(t) \sigma_{ge}(t) \rangle}, \end{aligned} \quad (2.11)$$

$$\begin{aligned} g^{(2)}(\tau) &= \frac{\langle \mathbf{E}^-(\mathbf{r}, t) \mathbf{E}^-(\mathbf{r}, t + \tau) \mathbf{E}^+(\mathbf{r}, t + \tau) \mathbf{E}^+(\mathbf{r}, t) \rangle}{\langle \mathbf{E}^-(\mathbf{r}, t) \mathbf{E}^+(\mathbf{r}, t) \rangle^2} \\ &= \frac{\langle \sigma_{eg}(t) \sigma_{eg}(t + \tau) \sigma_{ge}(t + \tau) \sigma_{ge}(t) \rangle}{\langle \sigma_{eg}(t) \sigma_{ge}(t) \rangle^2}. \end{aligned} \quad (2.12)$$

The correlation functions are mapped to the expectation values of the two-time products of atomic projection operators. However, the expectation values of the single-time projection operators not the two-time ones can be directly calculated.

$$\begin{aligned}\langle \sigma_{ge}(t) \rangle &= \text{Tr}\{\rho \sigma_{ge}\} \exp(-i\omega_L t) \\ &= \rho_{eg}(t) \exp(-i\omega_L t),\end{aligned}\tag{2.13}$$

$$\langle \sigma_{eg}(t) \rangle = \rho_{ge}(t) \exp(-i\omega_L t),\tag{2.14}$$

$$\langle \sigma_{eg}(t) \sigma_{ge}(t) \rangle = \rho_{ee}(t),\tag{2.15}$$

here the density matrix is the solutions of the master equations (2.7) and (2.8) in a rotating frame with laser frequency. With the help of *quantum regression theorem* [33], the  $t + \tau$  dependent operators can be written as a linear superposition of the  $t$  dependent operators, therefore, we can eventually calculate the correlation functions using the single-time density matrix elements[32].

When the laser is resonant with the transition, we get  $g^{(1)}$  for RFL as:

$$\begin{aligned}g^{(1)}(\tau) &= \exp(-i\omega\tau) \left\{ \frac{\Gamma_{sp}^2}{\Gamma_{sp}^2 + 2\Omega_R^2} + \frac{1}{2} \exp\left(-\frac{\Gamma_{sp}\tau}{2}\right) \right. \\ &\quad \left. + \frac{(\Gamma_{sp} - 4i\lambda)^2 \exp[-i\lambda\tau - (3\Gamma_{sp}\tau/4)]}{16i\lambda(3\Gamma_{sp} + 4i\lambda)} + (\lambda \rightarrow -\lambda) \right\},\end{aligned}\tag{2.16}$$

where  $\lambda = (\Omega_R^2 - \frac{1}{16}\Gamma_{sp}^2)^{1/2}$ , and the fourth term in the large bracket is as same as the third term with the sign of  $\lambda$  reversed.

For  $g^{(2)}$ , in the weak incident field limit ( $\Omega_R \ll \Gamma_{sp}$ ) we got,

$$g^{(2)}(\tau) = (1 - \exp(-\Gamma_{sp}\tau/4))^2,\tag{2.17}$$

and for the case of  $\Omega_R > \Gamma_{sp}/4$ , we got

$$g^{(2)}(\tau) = 1 - [\cos(\lambda\tau) + (3\Gamma_{sp}/4\lambda) \sin(\lambda\tau)] \exp(-3\Gamma_{sp}\tau/4).\tag{2.18}$$

Simulations of  $g^{(2)}$  are shown in Fig. 2.1, which indicate the nonclassical effects such as photon anti-bunching and sub-Poissonian statistics. However, an oscillatory dependence on time delay  $\tau$  and Rabi frequency makes it unique from the single photon emission by above band excitation [2, 3, 4]. We will come back to this later in Subsection 2.1.4.

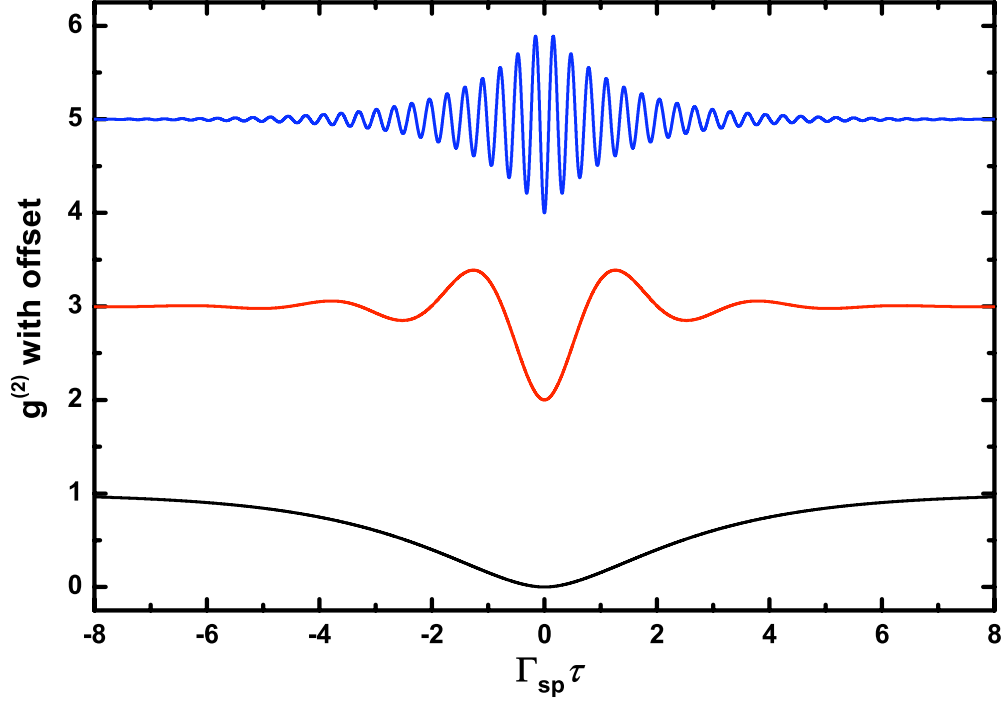


**Figure 2.1:** Simulations for time delay  $\tau$  dependence of resonance fluorescence second correlation function for zero detuning and different Rabi frequencies. The black curve corresponds to the case of  $\Omega_R \ll \Gamma_{sp}$ , the red curve corresponds to the case of  $\Omega_R = 2.5\Gamma_{sp}$ , and the blue curve corresponds to the case of  $\Omega_R = 20\Gamma_{sp}$ .

### 2.1.3 Fourier transform of the time dependent correlation function

The correlation functions discussed in last section reveal the coherent properties of RFL, while from the other perspective, the RFL spectrum reveals more direct information of the source, the atomic system. According to *Wiener-Khintchine theorem* [34], the spectrum  $F(\mathbf{r}, \omega_{sc})$  is obtained by taking the Fourier transform of the first order correlation function with respect to  $\tau$ ,

$$F(\mathbf{r}, \omega_{sc}) = \frac{1}{\pi} \text{Re} \int_0^\infty d\tau \langle \mathbf{E}^-(\mathbf{r}, t) \mathbf{E}^+(\mathbf{r}, t + \tau) \rangle \exp(i\omega_{sc}\tau). \quad (2.19)$$

From Eq. (2.10), we have,

$$\langle \mathbf{E}^-(\mathbf{r}, t) \mathbf{E}^+(\mathbf{r}, t + \tau) \rangle = I_0(\mathbf{r}) \langle \sigma_{eg}(t) \sigma_{ge}(t + \tau) \rangle, \quad (2.20)$$

where

$$I_0(\mathbf{r}) = \left( \frac{e\omega_0^2}{4\pi\epsilon_0 c^2} \frac{\mathfrak{D}_{ge} \cdot (\mathbf{r} - \mathbf{r}_0)}{|\mathbf{r} - \mathbf{r}_0|^2} \right)^2. \quad (2.21)$$

Hence, with the light field resonant with the transition ( $\omega_L = \omega$ ), we have the spectrum [31],

$$\begin{aligned}
 F(\mathbf{r}, \omega_{sc}) &= \frac{1}{\pi} I_0(\mathbf{r}) \text{Re} \int_0^\infty d\tau \langle \sigma_{eg}(t) \sigma_{ge}(t + \tau) \rangle \exp(i\omega_{sc}\tau) \\
 &= \frac{I_0(\mathbf{r})}{4\pi} \left( \frac{\Omega_R^2}{\Gamma_{sp}^2 + 2\Omega_R^2} \right) \left[ \frac{4\pi\Gamma_{sp}^2}{\Gamma_{sp}^2 + 2\Omega_R^2} \delta(\omega - \omega_{sc}) \right. \\
 &\quad + \frac{\Gamma_{sp}}{(\omega - \omega_{sc})^2 + (\Gamma_{sp}/2)^2} + \frac{a_+}{(\omega + \lambda - \omega_{sc})^2 + (3\Gamma_{sp}/4)^2} \\
 &\quad \left. + \frac{a_-}{(\omega - \lambda - \omega_{sc})^2 + (3\Gamma_{sp}/4)^2} \right], \tag{2.22}
 \end{aligned}$$

where  $a_{\pm} = \frac{3\Gamma_{sp}}{4}P \pm (\omega \pm \lambda - \omega_{sc})Q$ , and

$$P = \frac{2\Omega_R^2 - \Gamma_{sp}^2}{2\Omega_R^2 + \Gamma_{sp}^2}, \quad Q = \frac{\Gamma_{sp}}{4\lambda} \frac{10\Omega_R^2 - \Gamma_{sp}^2}{2\Omega_R^2 + \Gamma_{sp}^2}. \tag{2.23}$$

Although the equation above gives a complicate formula for the spectrum, it is clear that we can decompose it into two categories. The first term of the four is one delta function which indicates the dipole oscillating with the driving field and emitting monochromatic radiation at this frequency  $\omega_L$ . This term is denoted by the coherent part or the elastic scattering part of the spectrum, which has the same spectral properties as the driving laser. The rest three terms of the spectrum formula is denoted by the incoherent part or the inelastic part, and it becomes more pronounced with the strong field limit when  $\Omega_R \gg \Gamma_{sp}/4$ , produce the striking character of RFL, the Mollow-triplet,

$$\begin{aligned}
 F(\mathbf{r}, \omega_{sc}) &= \frac{I_0(\mathbf{r})}{8\pi} \left[ \frac{\Gamma_{sp}}{(\omega - \omega_{sc})^2 + (\Gamma_{sp}/2)^2} + \frac{3\Gamma_{sp}/4}{(\omega - \Omega_R - \omega_{sc})^2 + (3\Gamma_{sp}/4)^2} \right. \\
 &\quad \left. + \frac{3\Gamma_{sp}/4}{(\omega + \Omega_R - \omega_{sc})^2 + (3\Gamma_{sp}/4)^2} \right], \tag{2.24}
 \end{aligned}$$

which has three Lorentzian peaks located at frequencies of  $(\omega - \Omega_R, \omega, \omega + \Omega_R)$ , with linewidths of  $(3\Gamma_{sp}/2, \Gamma_{sp}, 3\Gamma_{sp}/2)$ , the peak height ratio of  $1 : 3 : 1$  and the integrated intensity ratio of  $1 : 2 : 1$ . One simulation is shown in right-bottom panel of Fig. 2.2.



### 2.1.4 Dressed state picture

Dressed state picture [35] is the more physical aspect to understand the RFL spectrum, especially for the strong field case. The concept of “dress” comes from the coupling between the atomic system and light field. For more convenient discussion, we quantized the light field and rewrite the Hamiltonian (2.3),

$$H_s = -(1/2)\hbar\delta\sigma_z + \hbar g(a^\dagger\sigma_{ge} + a\sigma_{eg}), \quad (2.25)$$

where  $\sigma_z = |e\rangle\langle e| - |g\rangle\langle g|$ ,  $g = e(\omega_L/2\varepsilon_0\hbar V)^{1/2}\mathbf{e}_L \cdot \mathbf{D}_{ge}$  is the coupling strength,  $a^\dagger$  and  $a$  are the creation and annihilation operators for laser field, respectively. Without

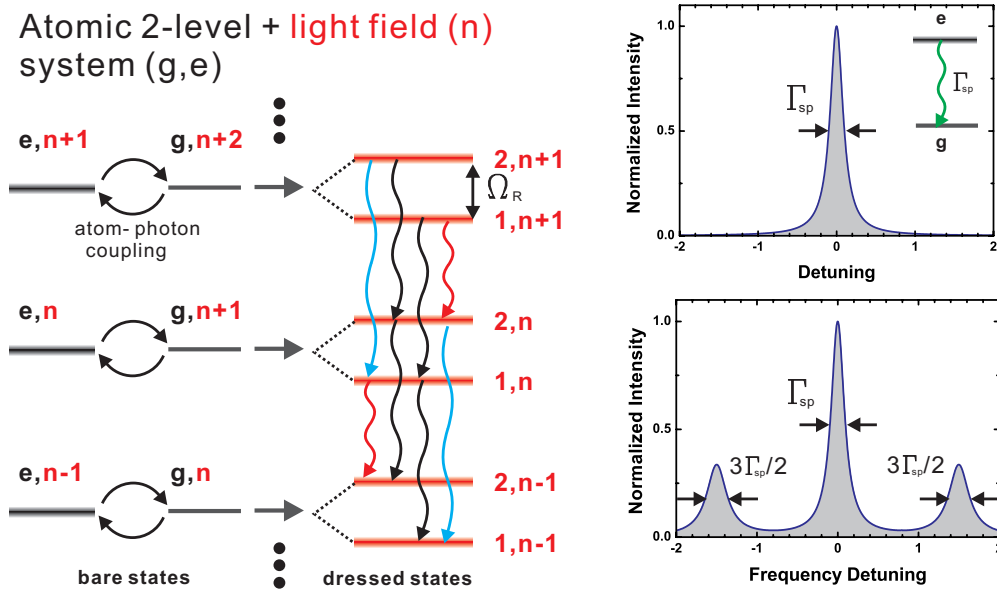


**Figure 2.2:** Schematic of dressed states for a two-level system resonantly driven by a single mode light field. The bare states are denoted by state  $|g, n\rangle$  and  $|e, n\rangle$  with photon number  $n$  of the light field. The dressed states are denoted by  $|1, n\rangle$  and  $|2, n\rangle$ . The two panels on the right side are the single Lorentzian decay spectrum of two level system and Mollow-triplet spectrum of dressed states, respectively.

the atom-light coupling, i.e. the second term of the Eq.( 2.25), the Hamiltonian only has diagonal term, the eigenstates of the system are labeled by atomic discrete level  $e$  and  $g$  associated with laser photon number  $n$  as  $|e, n\rangle$  and  $|g, n+1\rangle$ , and named by “bare states”. However, when the light coupling term is taken into account, which brings the off-diagonal term to the Hamiltonian making the bare states no longer the eigenstates, the atomic system is “dressed” by the light field. The eigenstates  $|1, n\rangle$  and  $|2, n\rangle$  of the dressed system are the superpositions of the bare states, and

named by “dressed states”.

Under the basis of manifold  $\{|e, n\rangle, |g, n+1\rangle\}$ , the matrix of Eq.( 2.25) is,

$$H_s = \frac{\hbar}{2} \begin{pmatrix} -\delta & \Omega_R \\ \Omega_R & \delta \end{pmatrix} \quad (2.26)$$

where  $\hbar\Omega_R/2 = g\sqrt{n+1}$  with the large photon number approximation, so that  $n-1 \approx n \approx n+1$ . Considering the coupling strength  $g$  is extremely small due to the large mode volume, so that any observable coupling effects need huge number of photons, which supports the classical treatment of the light field in previous three subsections.

The dressed states are:

$$|1, n\rangle = \sin\theta|g, n+1\rangle + \cos\theta|e, n\rangle, \quad (2.27)$$

$$|2, n\rangle = \cos\theta|g, n+1\rangle + \sin\theta|e, n\rangle, \quad (2.28)$$

where  $\tan 2\theta = -\Omega_R/\delta$ . The two states are separated by an interval

$$\hbar\Omega = \hbar\sqrt{\delta^2 + \Omega_R^2}, \quad (2.29)$$

which is also the definition of effective Rabi frequency.

In the case of resonant atom-light coupling ( $\delta = 0$ ,  $\Omega = \Omega_R$ ), we have the level schematic in Fig. 2.2. Jaynes-Cummings ladder [36] is shown there. The incoherent emission comes from the spontaneous cascade decay between the dressed-state manifolds. There are four decay paths, two of them carry the central frequency  $\omega_L$ , and other two are symmetrically blue- and red-shifted from the central frequency with the detuning  $\Omega_R$ , respectively. Moreover, the dressed states are the superpositions of bare states with equal coefficients ( $\sin\theta = \cos\theta = \sqrt{2}/2$ ), so that the four decay channels have the same strength, which results in the integrated intensity of the three peaks as 1 : 2 : 1 and is consistent with the conclusion made in subsection 2.1.3.

More generally, with nonzero detuning  $\delta$ , the three peaks located at  $(\omega_L - \Omega, \omega_L, \omega_L + \Omega)$ , and the intensity of the three peaks can be derived by solving the steady states from Master equations with Hamiltonian (2.25) and the Lindblad term

of  $\Gamma_{sp}$  [35].

$$\Gamma_{blue} = \Gamma_{red} = \frac{\sin^4 \theta \cos^4 \theta}{\sin^4 \theta + \cos^4 \theta} \frac{\Gamma_{sp}}{2}, \quad (2.30)$$

$$\Gamma_{central} = \frac{2 \sin^4 \theta \cos^4 \theta}{\sin^2 \theta \cos^2 \theta + \cos^2 \theta \sin^2 \theta} \frac{\Gamma_{sp}}{2}. \quad (2.31)$$

Now, under the dressed state picture, we revisit the  $g^{(2)}$  discussion in Subsection 2.1.2, where the unique oscillating photon correlation is presented. The photon emission process could be understood as projecting the upper  $(n+1)$  manifold dressed states to  $|e, n+1\rangle$  and lower  $(n)$  manifold dressed states to  $|g, n+1\rangle$ . After one photon emitted, the atomic system starts state oscillation between  $|g, n+1\rangle$  and  $|e, n\rangle$  with the Rabi frequency  $\Omega$  reforming dressed states. If the Rabi frequency is much faster than the decay rate, we expect to observe the oscillation within  $g^{(2)}$  valley as shown in Fig. 2.1. Therefore, the oscillating second order correlation implies the photon cascade decay process between dressed states.

## 2.2 Experimental setup and control abilities

Our aim is to demonstrate RFL in single QD system. The two-level system selected is the single electron spin states and their related trion states ( $|g\rangle = |\uparrow\rangle, |e\rangle = |\uparrow\downarrow\uparrow\rangle$ ) or ( $|g\rangle = |\downarrow\rangle, |e\rangle = |\downarrow\uparrow\downarrow\rangle$ ). With the case of zero external magnetic field  $B = 0$  and erasing the polarization information ( $\sigma_+, \sigma_-$ ) of their optical transition ( $X^{1-}$ ), this two two-level systems are degenerate, and can be treated as one two-level system, as shown in Fig. 2.3 (a). For driving the two level system, one CW laser with power and frequency controlled is required. For measuring the spectrum, photon lifetime and photon number statistics, one high resolution spectrometer, one femtosecond pulse laser and one  $g^{(2)}$  setup are required, respectively. In the following subsections, they will be introduced in turn. Starting from this section, all the frequencies applied are in the linear definition.

### 2.2.1 General optics

The QD operating system is shown in Fig. 2.3 (b). The QD sample is gated, housed in a magneto-optical bath cryostat and cooled to 4.2 K. A cubic zirconia solid immersion lens (SIL) is mounted on the epitaxial sample surface in order to improve both the light focusing and light gathering power of the fiber-based confocal microscope. The beam-splitter (BS) used here has 4% reflectivity, therefore its reflection

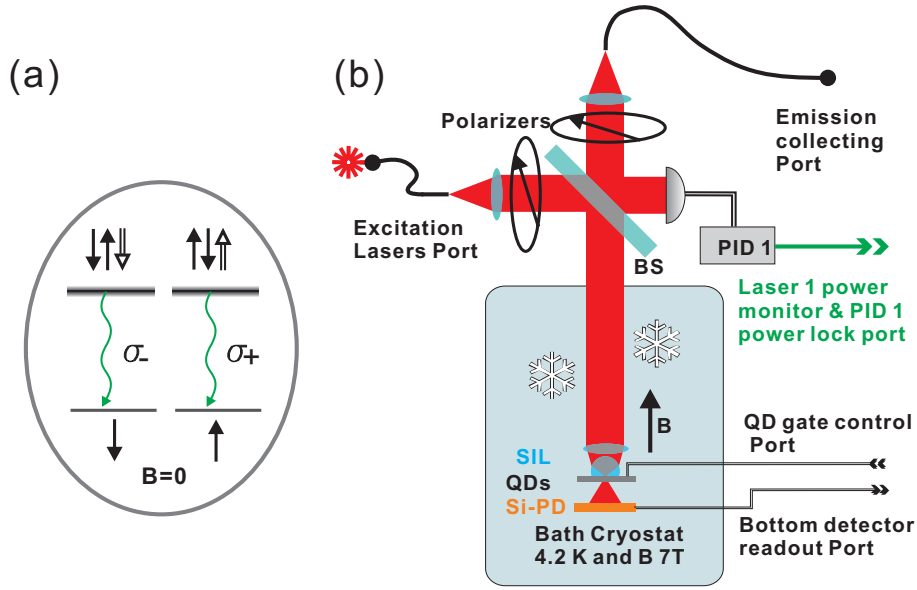


**Figure 2.3:** Degenerate two two-level systems in singly charged QD (a), and control-measure interface of QD operating system (b). The input ports of the system are: excitation laser port and QD sample gate control port. The output ports of the system are: emission collecting port, bottom detector readout port and laser power monitor port.

arm is used for excitation and transmission arm is for collection. For exciting the degenerate two-level system, we pass the excitation laser through one linear polarizer. Another polarizer is mounted on the emission collecting arm but with perpendicular axis to the one in excitation arm. The two polarizers form the dark field measurement geometry, which can in principle block the strong excitation laser background from the emission. In our case, half of the emission can pass through the linear polarizer, meanwhile, their circular polarization information is erased. The bottom detector is used for DT, which can assist us to find transition resonance. The 96% transmission CW excitation laser through the BS is monitored by one photodetector, which is connected to one PID for sending feedback signal to stabilize the laser power.

### 2.2.2 Laser frequency and power control

In our experiments, the gate voltage, laser frequency and laser power are the key knobs for tuning atomic-light coupling. The gate on the sample can both control the charge status and tune the transition respect to the laser through DC-Stark shift, where the laser frequency need to be locked. On the other hand, when gate voltage is fixed, we need the control of both the tunability and stability of the laser

frequency. Laser frequency can be controlled by applying DC/AC voltage to the piezo in the diode laser head<sup>2</sup> to control its outer cavity.

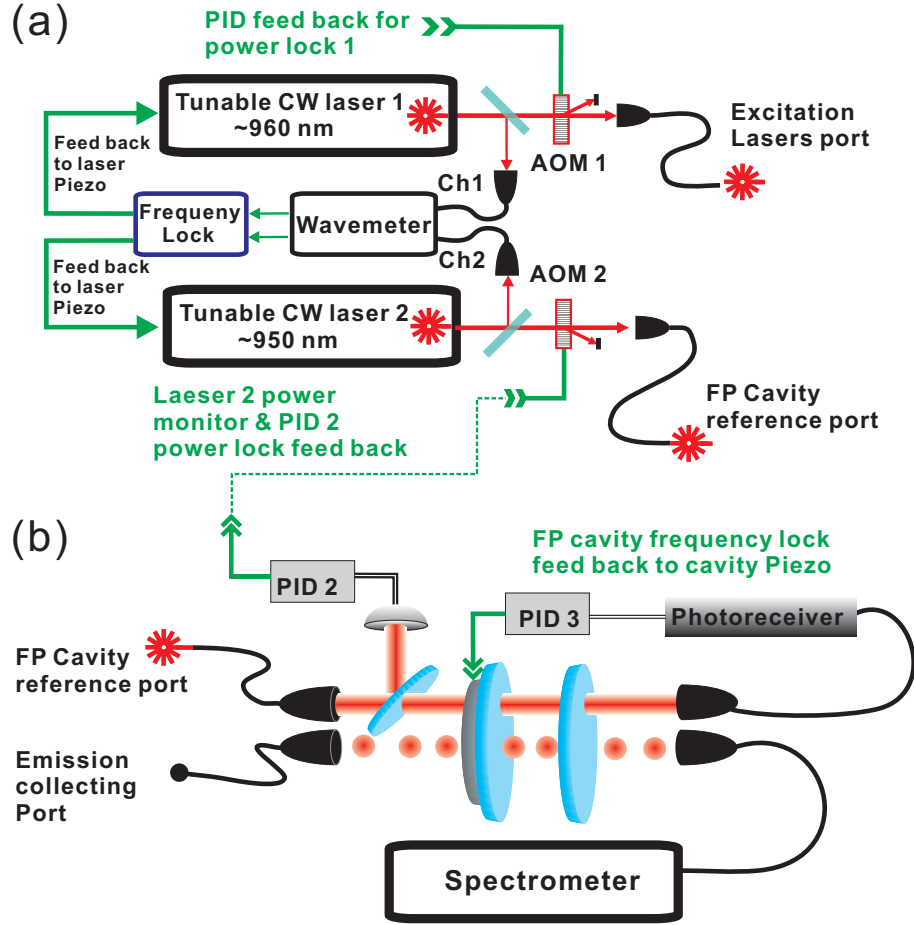


**Figure 2.4:** Tunable CW laser frequency and power control system (a) and Fabry Perot cavity based high resolution spectrometer (b). Laser 1 is for QD excitation and laser 2 is for locking Fabry Perot cavity. The frequency of the laser is locked by home made multichannel frequency lock system. The power of the laser is locked by PID circuits sending feedback signal to control the intensity portion of the zero order diffraction of the AOM.

As shown in Fig. 2.4 (a), one multichannel wavemeter<sup>3</sup> is used for monitoring laser frequencies, its outputs are sent to one home made multichannel frequency digital lock system and compared with the setpoints, which are either constant values or varying values from a function, and then the fast feedback signals are sent to the piezos of each laser head. Our frequency lock system has the channel capacity of 4, the locking stability of around 1MHz (Fig. 2.5), and the ability of arbitrary function scan.

<sup>2</sup>New Focus “Velocity” laser, Toptica DL pro940 laser

<sup>3</sup>HighFinesse SW-U wavemeter

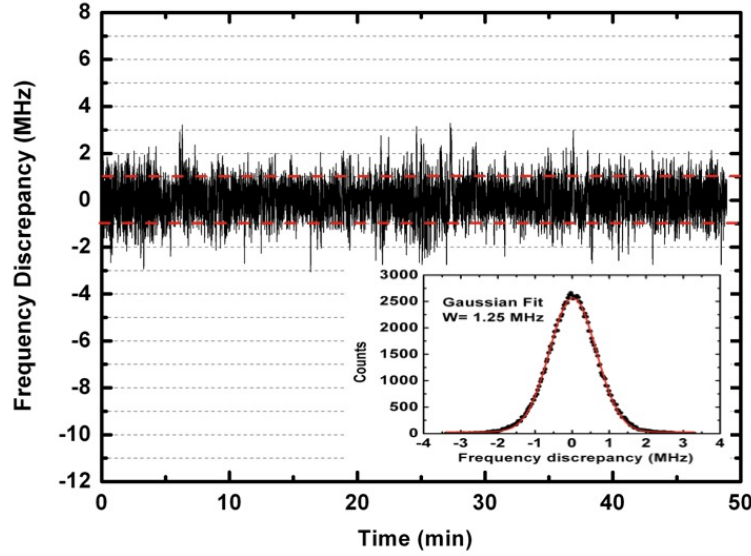


**Figure 2.5:** Laser frequency stabilization. The frequency is monitored by wavemeter and recorded for 50 minutes. The insert is the histogram of the frequency record, which is fitted by Gaussian function with the width of 1.25MHz.

One laser power locking system consists an Acousto-Optic modulator (AOM)<sup>4</sup>, a photodetector and a PID circuits<sup>5</sup>. In Fig. 2.4, each laser beam is passing through one AOM and the zero-order diffraction is coupled into a fiber for following applications. The photodetector (the one is connected with PID1 in Fig. 2.3 (b) or the one is connected with PID2 in Fig. 2.4 (a)) monitor the laser power after the last output fiber coupler for each beam path so that power varying due to both laser itself and fiber transmission are taken into account. The measurements of photodetector are sent to PID (PID1 or 2), where the measured values are compared with the setpoint, then feedback signals are sent to AOM to adjust the power portion in its zero-order diffraction. Our typical power stability is about 0.5%.

### 2.2.3 High resolution spectrometer

For resolving the resonance fluorescence spectrum, we need spectral resolution to be smaller than  $\Gamma_{sp}$  (typically several hundred MHz). A two-mirror Fabry Perot cavity (FP cavity) is set up for this purpose. This cavity can function as one tunable spectral band pass filter with the tunability of 30 GHz (Free Spectral Range) and the spectral window of about 35 MHz (Fig. 2.6). The throughput of the transmission peak is about 30%. The control scheme for the FP-cavity transmission frequency

<sup>4</sup>AA Opto-Electronic, MT80-A1,5-IR

<sup>5</sup>Stanford Research Systems, SIM900

is shown in Fig. 2.4 (b). We send a frequency controlled and power stabilized laser beam as the reference passing through the cavity aside from the RFL signal path. The reference transmission signal is monitored and the middle point on its slope is selected as the setpoint of PID circuits (PID3), so that by sending feedback signal to the piezo of the cavity mirror we can lock the FP cavity onto a certain transmission frequency with a certain detuning from the reference laser. So, tuning cavity transmission frequency is equivalent to tuning the reference laser frequency.

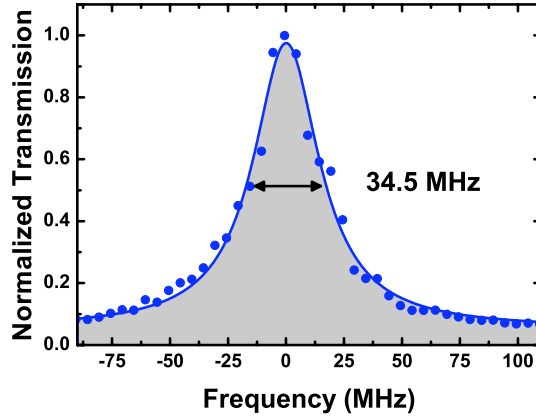


**Figure 2.6:** The measured transmission linewidth of the FP cavity as it is scanned across frequency locked laser with the uncertainty about 1.25 MHz.

#### 2.2.4 Second order correlation function and lifetime setup

In Fig. 2.7, we present the experimental setup for  $g^{(2)}$  and lifetime measurements. Three lasers are used for different tasks: the frequency and power controlled CW laser is used for resonant excitation scheme. the 780-nm CW laser is used for the above-band excitation and the Ti:Sa pulsed laser is used for direct lifetime measurement, where APD3 is triggered by the pulsed laser to give start signals and APD1 measures the PL photon to give the time delayed stop signals.

### 2.3 Quantum dot spin-resolved resonance fluorescence

In this section, we discuss our spectrum measurements of RFL from single QD. With zero external magnetic field, we observed the excitation power and frequency dependent RFL spectrum. With nonzero external magnetic field in Faraday configuration, i.e. the orientation of the magnetic field is along z direction, we observed spin-resolve

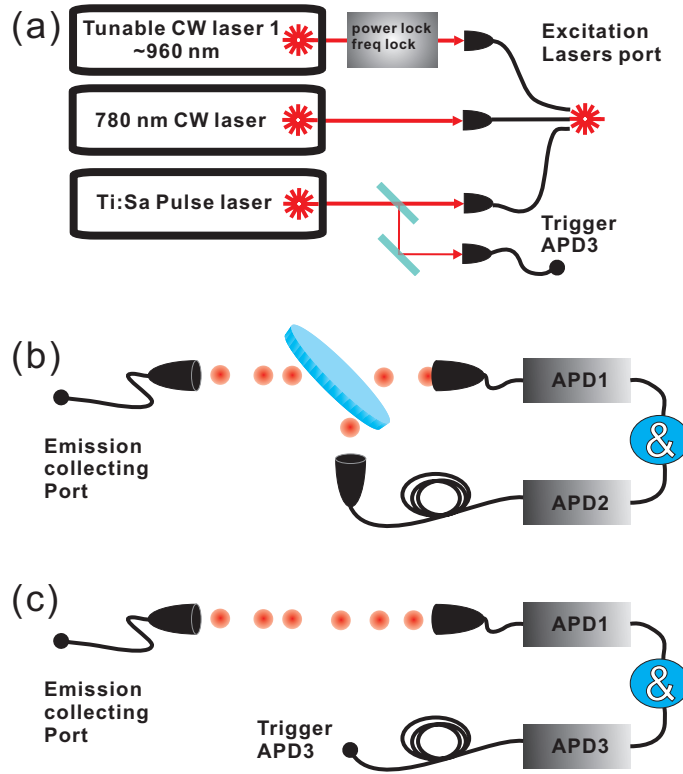


**Figure 2.7:** The experimental scheme for  $g^{(2)}$  and photon lifetime measurements. (a) The excitation laser setup, (b) The  $g^{(2)}$  setup. (c) The lifetime setup.

RFL spectrum. We note the linear-frequency symbols used in this section from their circular counterparts:

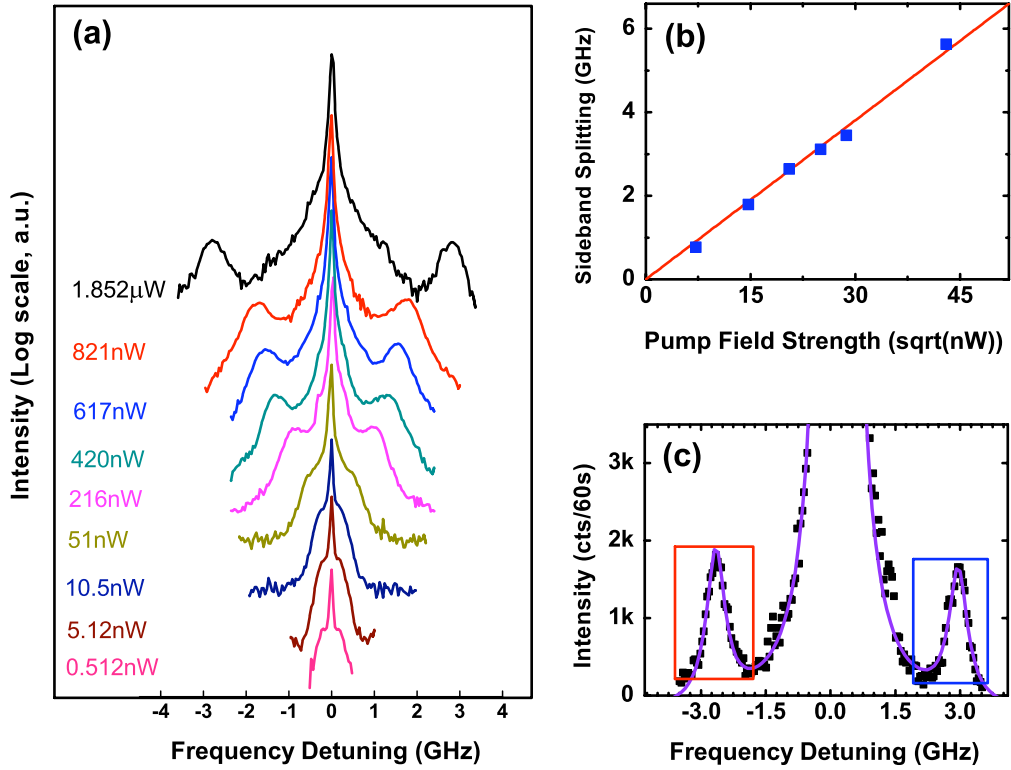
$$\omega \rightarrow \nu, \quad \omega_L \rightarrow \nu_L, \quad \Omega_R \rightarrow \Omega_R, \quad \Omega \rightarrow \Omega, \quad \delta \rightarrow \Delta. \quad (2.32)$$

### 2.3.1 Mollow triplet under laser power control

By using the setup presented in Fig. 2.3 (b) and Fig. 2.4, under zero magnetic field we record the scattered light intensity as a function of FP cavity transmission frequency. Figure 2.8 (a) presents  $X^{1-}$  RFL spectra on a linear-log scale for a range of driving laser power from 0.512 nW ( $\Omega_R \approx 0.13\Gamma$ ) to 1.825  $\mu$ W ( $\Omega_R \approx 8\Gamma$ ). The laser is set to be resonant with the doubly degenerate bare  $X^{1-}$  QD transition frequency, which was determined from our DT measurements. For laser powers above 216 nW, two equal weight sidebands emerge, which, together with the central feature, constitute the Mollow triplet. The two sidebands arise from radiative transitions between the outer (blue arrow) and inner (red arrow) rungs of the Jaynes-Cummings ladder in Fig. 2.2. The strong central feature is the result of the unsuppressed residual



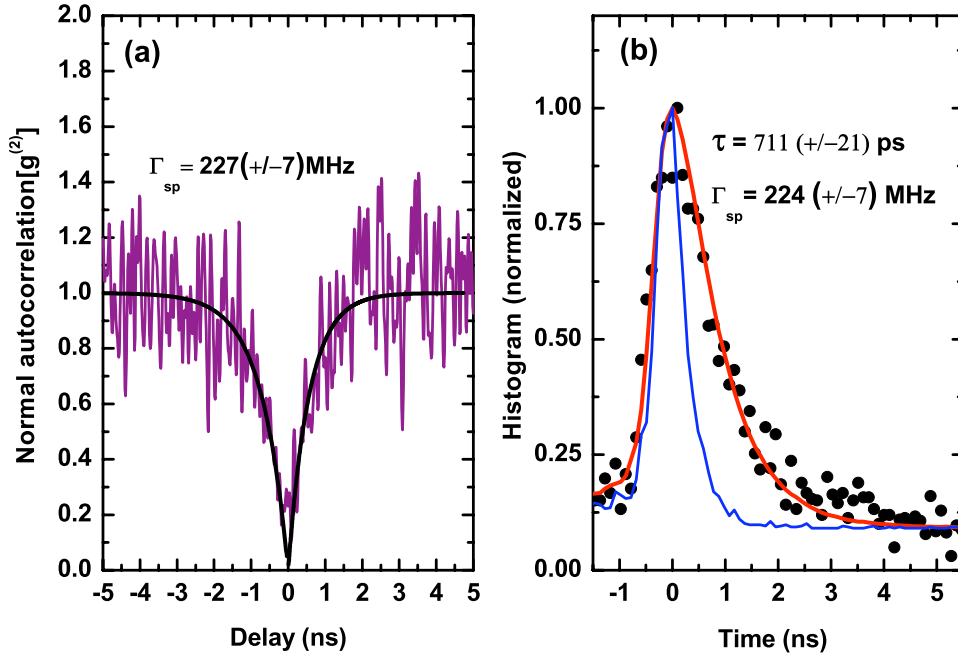
laser leaking through our cross-polarizer instrumentation. Peak-to-peak sideband splittings determined from this data set are plotted in Fig. 2.8 (b) against the square-root of the laser power. In the strong excitation regime of  $\Omega_R \geq \Gamma_{sp}$ , the linear fit with a slop of  $0.127 \text{ GHz}/\sqrt{\text{nW}}$  indeed confirms the expected dependence of the sideband splitting on the bare Rabi frequency, or the square-root of the laser power [30].



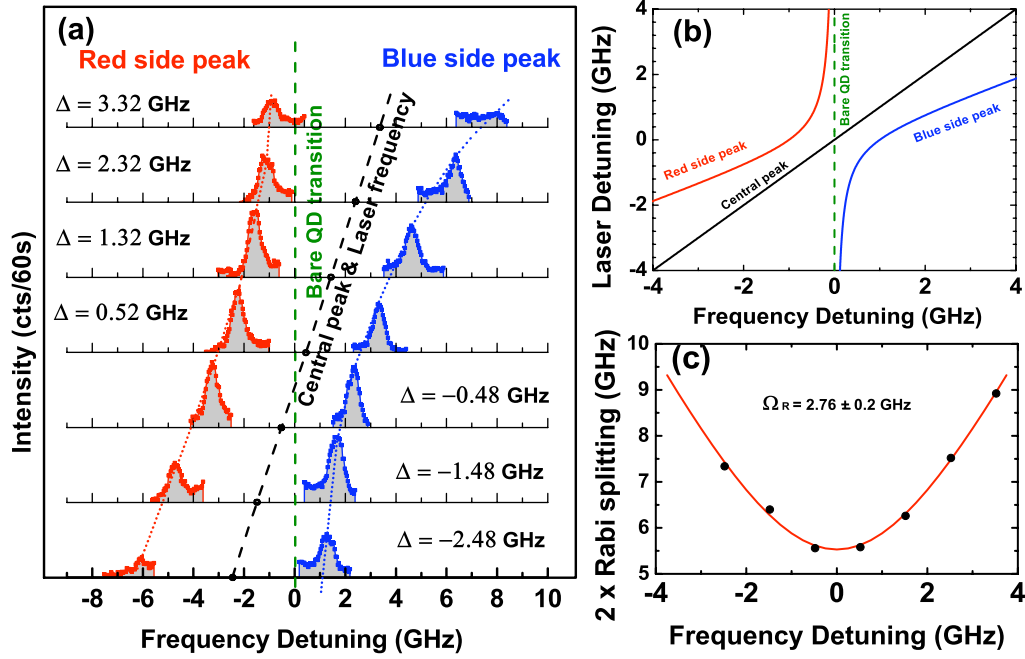
**Figure 2.8:** Power dependent resonance fluorescence. (a) Evolution of the Mollow triplet spectrum as the resonant laser power is increased from 0.512 nW to 1.852  $\mu\text{W}$  under zero magnetic field. The intensity of the spectrum is plotted in logarithmic scale. Each data point is recorded for 60 seconds. (b) Extracted sideband splitting as a function of pump field strength with a linear fit. (c) Zoom-in plot of the 1.852  $\mu\text{W}$  fluorescence spectrum sidebands with a linear intensity scale. The boxes highlight the sidebands from which we extract a transition linewidth of  $343(\pm 39) \text{ MHz}$ . and a collected photon rate of about 45,000 per second per sideband.

Figure 2.8 (c) is a linear-linear scale zoom-in to highlight the two Mollow sidebands when  $X^{1-}$  is driven by a 1.852- $\mu\text{W}$  laser. When fitted with the expected multi-Lorentzian RFL spectrum, a transition linewidth  $\Gamma$  of  $343(\pm 39) \text{ MHz}$  per

sideband can be extracted. For comparing this linewidth with the pure spontaneous emission rate, we apply the indirect (above band excitation  $g^{(2)}$ ) and direct lifetime measurements as shown in Fig. 2.9 (a) and (b) respectively. There we get the  $\Gamma_{sp}$  is about 225 MHz. In the presence of additional fast dephasing Markovian mechanisms, the transition linewidth is no longer determined by the pure spontaneous emission rate and is broadened to  $\Gamma = \Gamma_{sp} + 2\gamma_{\text{dephasing}}$ . The fitted sideband linewidth suggests that such dephasing mechanisms, if they at all exist in this regime of operation, are bounded by about 80MHz maximum possible rate, which suggests that emission from the triplet sidebands of the optically dressed QD transition is a predominantly radiative broadened process yielding near transform-limited photons; a pre-requisite for all proposed linear optics QIP applications.



**Figure 2.9:** Indirect and direct life-time measurement. (a) Second order correlation function measurement with above band excitation at a power well below the saturation level and carrier capture effects displays the true radiative lifetime of the excited state. The  $\Gamma_{sp}$  is fitted as  $227(\pm 7)$  MHz (b) Lifetime measurement. The blue curve is the instrument response function, the black circles are the measured raw data and the red curve is the best fit to the measured data obtained by convolving the instrument response function with an exponential function with a decay time of  $711(\pm 21)$  ps, which corresponds to  $\Gamma_{sp} = 224(\pm 7)$  MHz.



**Figure 2.10:** Dependence of resonance fluorescence on laser detuning. (a) Measured sidebands of the Mollow triplet as a function of laser detuning from the bare  $X^{1-}$  resonance under zero magnetic field. The laser power is fixed at  $1.852 \mu\text{W}$ . The red and blue dashed curves tracing the side bands are guides to the eye commensurate with the red and blue curves in (b). (b) Simulation of the scattered photon frequencies (red and blue solid curves) for the dressed states of an  $X^{1-}$  transition as a function of laser detuning. The dashed green line corresponds to the bare  $X^{1-}$  transition and the black dashed line indicates both the laser frequency and the central peak of fluorescence. (c) Side band splitting as a function of laser detuning.

### 2.3.2 Mollow triplet under laser frequency control

In addition to the laser power, the sideband spectrum may be tuned by controlling another externally accessible degree of freedom; the laser frequency. In Fig. 2.10 (a) the measured  $X^{1-}$  RFL spectra, driven by  $1.852 \mu\text{W}$  laser power ( $\Omega_R \approx 8\Gamma$ ), are plotted for a set of laser frequency detunings ( $\Delta$ ). For comparison, Fig. 2.10 (b) plots triplet peak frequencies

$$\nu_{\text{blue}} = \nu + \Delta + \Omega, \quad \nu_{\text{center}} = \nu + \Delta, \quad \nu_{\text{red}} = \nu + \Delta - \Omega \quad (2.33)$$

as a function of the laser frequency detuning at fixed laser power. Measuring the spectral separation of the red sideband, when the laser is red detuned by 2.48 GHz, to the blue sideband, when the laser is blue-detuned by 3.32 GHz, it is possible to achieve photon emission across a frequency band of 14 GHz. This is 40 times

larger than the 356-MHz spontaneous emission rate, and is by no means an upper limit, but can be further increased by laser power and detuning. In order to relate this range to other tuning mechanisms, we emphasize that 13 GHz is the range obtainable via DC stark shift of the  $X^{1-}$  transition throughout the whole single electron charging plateau [12]. Alternatively, this is the same frequency shift that each of the two degenerate  $X^{1-}$  transitions experiences under an applied magnetic field of 1 Tesla [23]. The sideband splittings extracted from the data set of Fig. 2.10 (a), are plotted in Fig. 2.10 (c) as a function of laser detuning. The red fit curve with the two times effective Rabi frequency ( $2\sqrt{\Omega_R^2 + \Delta^2}$ ) can be used to determine a bare Rabi frequency of  $2.76(\pm 0.2)$  GHz. From this value we determine a dipole moment of  $27.8(\pm 0.2)$  Debye in agreement with our DT measurements.

### 2.3.3 Spin-selective dynamic Stark effect and Mollow quintuplet

The final part of this section is on optical access to a QD spin, via RFL, where a finite magnetic field splits the electronic spin ground states lifting the  $X^{1-}$  spin degeneracy. A reproduction of Fig. 2.10 (b) under finite magnetic field and accounting for spin is presented in Fig. 2.11 a. The two dressed Zeeman split sidebands (the blue and red solid lines) are directly correlated to the spin state of the electron and their frequency splitting is controlled by laser detuning beyond that manifested by the magnetic field. In what follows all frequencies are referenced to the zero magnetic field QD  $X^{1-}$  resonance. First, a 50 mT external magnetic field is applied in the Faraday configuration. In Fig. 2.11 b the RFL spectrum of the blue-detuned sideband (the blue box in Fig. 2.11 a) is plotted for laser detunings of 1.75, 1.25, and 0 GHz, from left to right. By varying the laser detuning, at constant power, the Zeeman splitting of the transitions induced by the magnetic field can be altered (Fig. 2.11 b panels 1 & 2) and even cancelled (Fig. 2.11 b panel 3).

What we have demonstrated is a combined outcome of the Zeeman and dynamic Stark effect [37, 38, 39, 40], which allows us to tune independently the energy splitting of the ground and excited states. For InGaAs QDs, the electron and hole g-factors are known to be around -0.6 and 1.4 [23]. Therefore, the ground and excited state manifolds respond differently to the external magnetic field. The dynamic Stark effect, however, is independent of either manifold's Landé factor. Consequently, the two state manifolds in this regime display level splittings corresponding to an effective Landé factor tuned by the properties of the laser. The essence of this

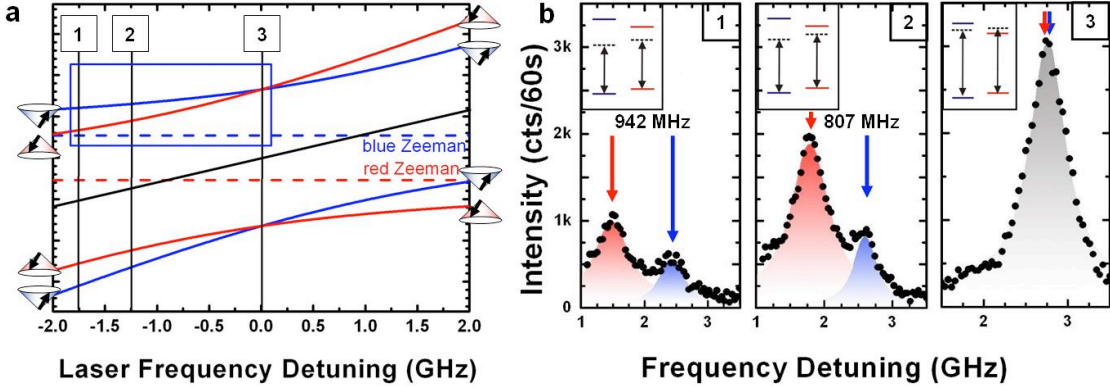


**Figure 2.11:** Spin-selective dynamic Stark effect. (a) The simulated scattered photon frequencies for the 1-GHz Zeeman split  $X^{1-}$  transitions under a 50-mT external magnetic field. The blue solid lines are the dressed sidebands corresponding to the blue shifted bare Zeeman transition (dashed blue line) and the red solid lines are the dressed sidebands corresponding to the red shifted bare Zeeman transition (dashed red line). The ends of each line are decorated with an illustration indicating the specific QD spin ground state for each transition. The blue box and the vertical solid black lines highlight the spectral window and laser detunings we experimentally investigate in panel (b). (b) The evolution of the blue-detuned Mollow sideband spectrum for a series of laser frequency detunings. The inset in the upper left corner illustrates how the laser detunes from the blue (red) Zeeman split transition. The number in the upper right corner designates the corresponding line cut indicated in panel a. The external magnetic field for all spectra is fixed to 50 mT, and the change in spin-splitting originates from laser detuning only.

effect lies in the imbalance of the effective Rabi frequencies experienced by the two spin transitions. In this work we utilize the  $\Delta$ -dependence to enforce this imbalance and show the cancellation of the magnetic field induced spin-splitting. The condition given in panel 3 of Fig. 2.11 b is particularly interesting, since both the ground and the excited states are identically split resulting in an effective Landé factor of 0.4. The consequence is the generation of photons with full spectral overlap, but well-defined spin tags in their circular polarization state for any applied magnetic field strength.

Finally, laser detuning and magnetic field are used to imprint the spin information onto the RFL in the form of a clear, background-free, spectrally distinguished sideband doublet. Figure 2.12 (a) is a linear-log plot of the full emission spectrum of another QD under 100 mT magnetic field, 13.2  $\mu$ W laser power ( $\Omega_R \approx 17\Gamma$ ) and 2.5 GHz red laser detuning. The plot exhibits a distinctive five-Lorentzian structure in the RFL spectrum beyond the previously discussed triplet and each sideband transition is now a clear doublet linked with a QD electronic spin state. In total there are 6 features in the spectrum, but, much like the Mollow triplet, the central

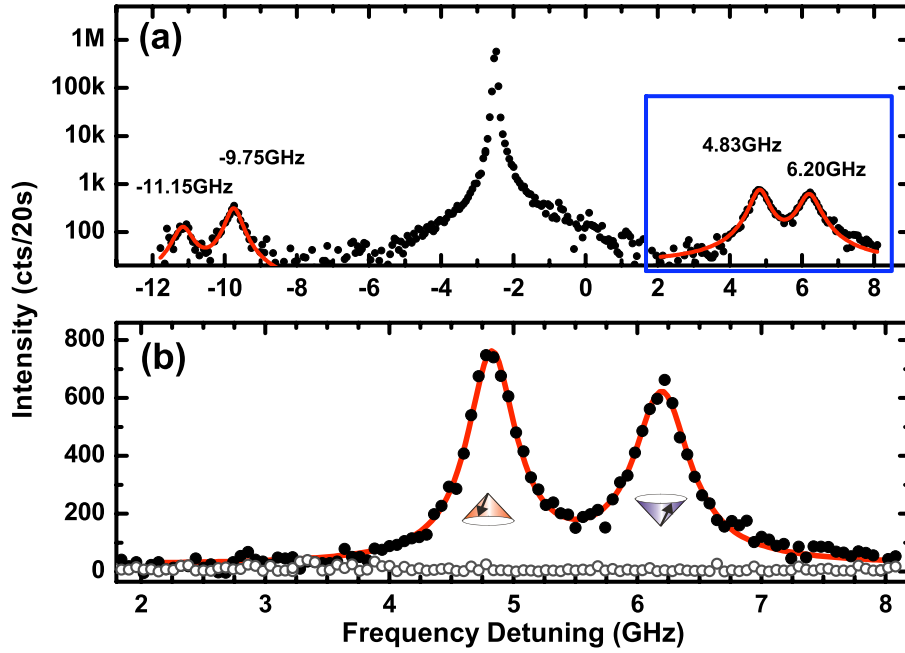


**Figure 2.12:** Mollow quintuplet and spin-resolved fluorescence. (a) The full span of the resonance fluorescence spectrum under application of a 100 mT magnetic field and a 2.5 GHz red detuned laser at a power of  $13.2 \mu\text{W}$  ( $\Omega_R \approx 17\Gamma$ ) plotted in a linear-log scale (blue circles). The number above each sideband peak indicates its central frequency with respect to the bare QD transition identified as the origin. (b) A zoom-in of the blue sideband spectrum plotted on a linear-linear scale. The data (black circles) are fit to two Lorentzian profiles (red curve) with a splitting of 1.38 GHz. The background is measured for identical conditions without the  $X^{1-}$  resonance (open circles).

line is comprised of two degenerate transitions locked to the detuned laser frequency yielding a spectral signature for the Mollow quintuplet. A zoom-in plot of the blue sideband doublet, indicated by the blue rectangle, is presented in Fig. 2.12 (b) in linear-linear scale. The red curve is a fit of two Lorentzians and the open circles represent the recorded signal in identical conditions except the single electron in the QD is unloaded back to the reservoir eliminating the  $X^{1-}$  transitions (The closest possible QD transition is detuned 1290 GHz from the laser frequency). This background signal constitutes less than 2% of the total signal. We note here that for all laser powers above 617 nW, when the two sidebands are clearly separable, the total number of photons collected per sideband remains constant confirming the absence of significant laser background in the above-quoted photon number.

### 2.3.4 Photon correlation of resonance fluorescence

Photon correlation measurement is also important for RFL study, however, we did not focus on this too much, partially because observing spectrum is more challengeable and has the benefit for revealing the spin-tagged information, and the other reason is that the time resolution (jitter) of our APDs, which is about 500 picosecond, is insufficient for solving oscillations for high Rabi frequency as we expected in Fig 2.1. We note that Flagg *et. al.* [8] and Ates *et. al.* [10] have demonstrated nice measurements on photon correlations.

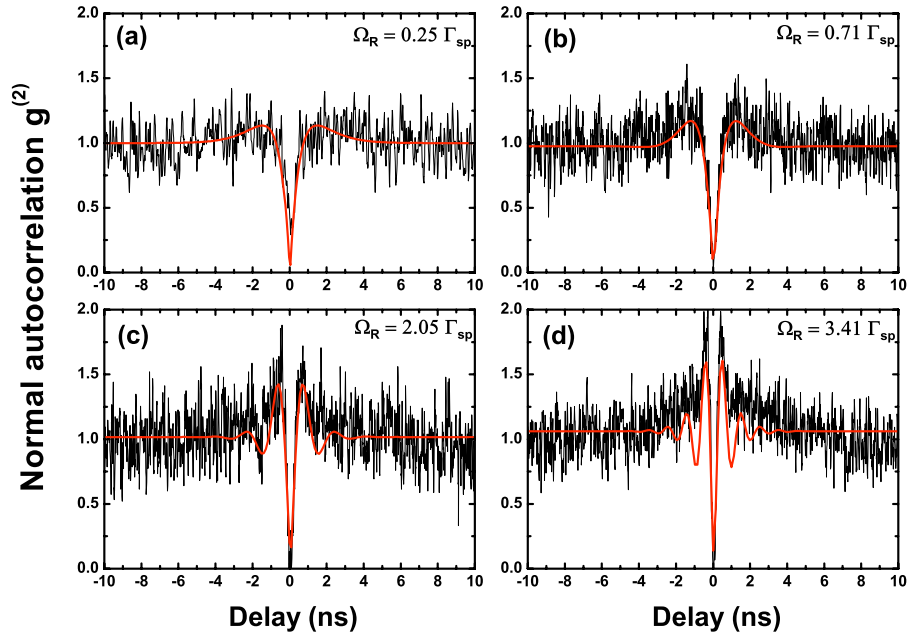


**Figure 2.13:** Second-order correlation function for RFL. From (a) to (d), the laser power is increasing. Panel (b), (c) and (d) are subtracted with the laser-leakage background and normalized with signal floor far from the time origin, panel (a) is only normalized without background subtraction. The red curves are the fitting from Eq. 2.18 with the parameters  $\Omega_R = 0.25\Gamma_{sp}$  for (a),  $\Omega_R = 0.71\Gamma_{sp}$  for (b),  $\Omega_R = 2.05\Gamma_{sp}$  for (c) and  $\Omega_R = 3.41\Gamma_{sp}$  for (d), respectively.

We measured the second order correlation function  $g^{(2)}$  with several laser powers by using the setup presented in Fig. 2.7, where no spectral resolution of the photon is required. Figure 2.13 only shows four results, among them, panels (b), (c) and (d) are subtracted with their laser-leakage background and normalized by the signal from large time delay, panel (a) is only normalized without subtraction, which strongly indicates the single photon character. The data are fitted by Eq. 2.18. We noticed

that we could not observe clear oscillation in  $g^{(2)}$  when Rabi frequency is larger than the spontaneous decay rate, however for smaller Rabi frequency, our measurement matches the theory very well.

## 2.4 Single photon generation and other applications

Coherently generating single photons from QDs motivated us from the beginning for realizing RFL, which is expected to provide transform-limited photons with high indistinguishability suitable for QIP applications. Moreover, due to the spin tagged character of our protocol, plenty of applications based on spin-photon interface of QDs become available, benefit both the QIP and the study of mesoscopic system.

### 2.4.1 Single photon generation

For single photon generation, we have some notes,

1. The photons from RFL are single photons. this has been demonstrated in Fig. 2.13, especially in panel (a).
2. We did not execute Hong-Ou-Mandel type measurement to examine the indistinguishability. The extracted transition linewidth from the sidebands of Mollow-triplet in our measurements suggests an upper bound about 80 MHz for non-radiative dephasing, so that we only claim our RFL photon is near-transform limited. Soon after we published the results, another group demonstrated the indistinguishability about 90% of RFL photons from QDs by two-photon-interference measurements [10], which shows the significant progress compared with previous incoherent-excitation approach [5]. For further improvements, we need to investigate more possible mechanisms effecting the photon emission in QD mesoscopic system.
3. In our RFL scheme, we need light field constantly drive the system forming sidebands, where we can collect background free single photons, therefore, CW laser is required. We have no control of when to generate photon, i.e. the generation is not deterministic. Realizing RFL sideband photons by pulsed laser is quite challengeable, however, resonantly driving one transition of a three-level  $\Lambda$  system, collecting stokes or anti-stokes photons might be a good choice for deterministic single photon generation in coherently pumping regime [41].



Alternatively, we would like to point out another interesting regime obtained via detuning. When the excitation laser frequency ( $\nu_L = \nu + \Delta$ ) is considerably far red-detuned, the red (blue) sideband frequency approaches  $2\nu_L - \nu$  ( $\nu$ ). This is indeed the analogous regime studied by Aspect *et al.*, on single atomic transitions [42]. In this seminal work, photon correlation measurements between these two sidebands revealed that the emission dynamics of the two sidebands in this regime is substantially different from that obtained in the near-resonant laser excitation. Specifically, the red-sideband photon has to be generated from two virtual states, while the blue-sideband photon is emitted from the two real atomic states. Due to the complex nature of this scattering process, the first photon to be emitted is hence always in the blue sideband, followed instantaneously by a photon in the red sideband. This regime of operation has immediate impact on heralded (on-demand) generation of single photons from the red-detuned sideband, when triggered by the detection of a photon from the blue-detuned sideband.

Last, for QIP applications, collection efficiency is as important a factor as spectral purity, so we present an estimate of the photon number collected from the sideband emission. At 13.2  $\mu\text{W}$  excitation power, more than 98% of the emission is coming from the sidebands. Integrating across the blue sideband within the 4 to 7 GHz window (book-keeping for the cavity transmission and detector efficiencies) we estimate that 48,000 photons per second per spin-sideband reach the input of our two-mirror cavity. We note that the emission from the two spin-sidebands is anticorrelated determined by the electron spin. Therefore, by matching the cavity transmission spectrum to a spin-sideband, QD spin measurements with above unity signal-to-noise ratio can be performed within a time integration of around 1 millisecond. While this timescale is already at the threshold of single-shot spin readout regime, straightforward technical improvements in photon collection efficiency [43] will further better this figure of merit.

### 2.4.2 Other applications

Most straight forward and expected application of our spin-resolved RFL is the electron spin readout. By simply collecting the RFL photons in moderate light-driving regime, we already achieved electron spin readout, which we will devote the whole next chapter to discuss. Another scheme is to select sideband photons with

their spin-tagged character, such as the spin-selectivity of the sideband in Mollow-quintuplet. For this scheme, we need the FP cavity with broad transmission bandwidth. One more interesting application is the spin-photon entanglement, which came to our mind at the first time we observed the Zeeman-splitting cancellation in Mollow-quintuplet spectrum. It will definitely strengthen the candidate-ship of QDs as the promising interface of flying- and stationary- qubits in QIP. However, in our present setup, we can not go further on this application, since the cross polarizer settings remove the polarization information of emitted photons. Alternative experimental designs can overcome this issue, such as in the work [8, 10], microcavities are fabricated around QDs, which can enhance the photon collection perpendicular to the excitation laser without any polarizers as filters. Unfortunately, they have no gate control on the QDs, so no control of electron spin states. Integrating gate structure to microcavity will be our common task in the near future.

## Chapter 3

# Direct electron spin readout in single quantum dots by resonance fluorescence

In this chapter, we present an important application following last chapter, probing optical transitions by counting resonance fluorescence photons without spectral resolution, which is widely applied in many other systems such as trapped single ion. More interestingly, probing the spin-selective transitions provides us a technique for electron spin readout which is one of the most crucial requirements for both quantum information processing and the study of mesoscopic system. For studying the dynamics of confined electron spin in QDs, we carry out the first n-shot time-resolved resonance fluorescence (TRRFL) measurements. Firstly, we study the back action on the electron spin states induced by optical measurements to quantify the characteristic time  $T_{BA}$ , which denotes the time an optical field can cycle a spin-selective dipole transition before a spin-pumping event happens. We study the explicit dependence of the spin-pumping Raman scattering timescale on the properties of the magnetic field and show that this process is mediated by ground-state mixing due to electron-nuclei coupling up to 0.6 Tesla, while the excited-state mixing due to the hole spins mediates the same process for higher magnetic fields. Secondly, we study the electron spin relaxation process to quantify the characteristic time  $T_1$ . We further demonstrate the spin relaxation rate ( $1/T_1$ ) can vary more than two orders of magnitude following the magnetic field dependence expected from spin-orbit interaction inducing a ground-state spin admixture. In the last section we discuss the time resolution, or fastest experimentally accessible timescale of TRRFL in the

context of single-shot readout of spins in QDs.<sup>1</sup>

### 3.1 Probing two-level system by counting resonance fluorescence photons

Before we study the electron spin dynamics, we carry out the measurement to calibrate the ability of probing optical transitions on spin-free states. With zero external magnetic field, the singly charged state and the trion state are selected to form the two level system as shown in the inset of Fig. 3.1. Fixing the gate voltage applied

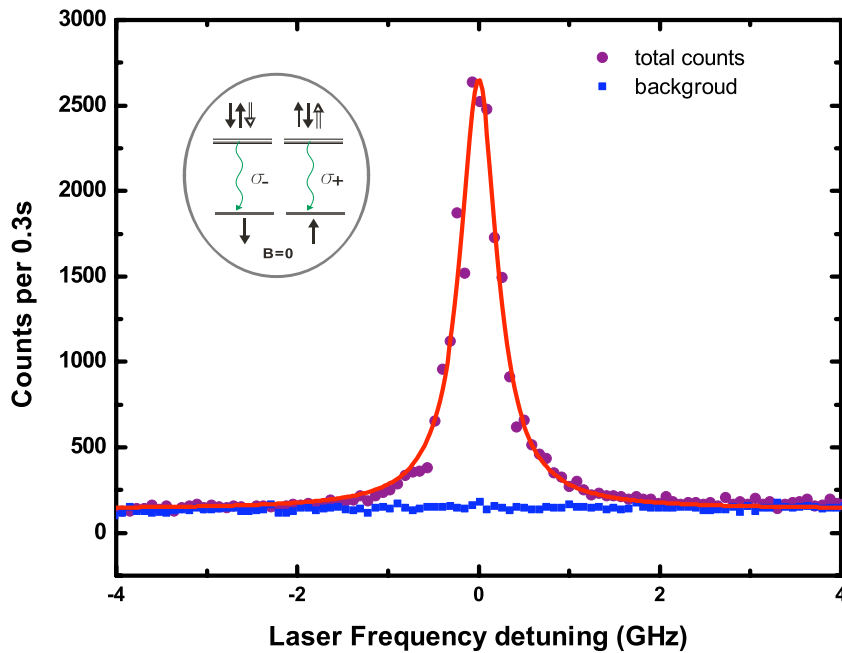


**Figure 3.1:** The integrated resonance fluorescence (purple circles) from the  $X^{1-}$  transition as a function of laser detuning. The laser power is about the spontaneous emission rate ( $\Omega_R \sim \gamma_{sp} \approx 227$  MHz). Each data point corresponds to 300 ms of integration. The blue squares indicate the background level when the transition is far detuned via gate voltage. There is no external magnetic field and the insert is the schematic of the degenerated two level system of  $X^{1-}$ .

on the QD sample, we scan the laser frequency across the transition and collect the resonance fluorescence photons at each data point for 300 ms integration. The data indicate a symmetric Lorentzian lineshape which directly reflects the properties of the dipole transition<sup>2</sup> we probed as shown in Fig. 3.1. The signal-to-noise ratio (SNR) reach 190 (with the noise level of 13) which is larger than DT measurements

<sup>1</sup>This chapter is based on publication [1]

<sup>2</sup>As long as the lineshape of the total signal is symmetric, the interference term between the coherent scattering and the laser leakage carries the same spectral properties as the dipole transition probed as we shown in Eq. (1.3).

with even longer integration time<sup>3</sup>, the signal-to-background ratio (the background data is shown as the blue square in the Fig. 3.1) is 18, and the linewidth is 492 MHz. More systematic calibrations are shown in Fig. 3.2. Panel (a) shows the linewidth

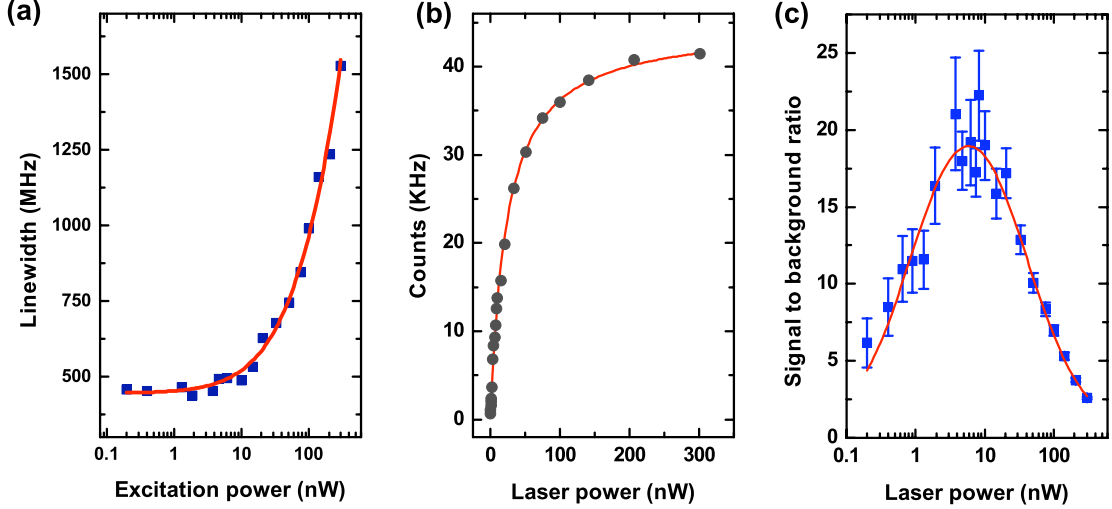


**Figure 3.2:** The systematic calibrations of the transition readout using resonance fluorescence as a function of laser power. (a) The linewidth measurement indicating the power broadening mechanism. (b) The saturation curve of the the peak counts of the transition, where the laser background is subtracted. (c) The signal-to-background ratio.

increasing as the excitation power is increased, which indicates the power broadening mechanism ( $\text{FWHM} = (\Gamma_{sp}^2 + 2\Omega_R^2)^{1/2}$ ). Panel (b) is the saturation curve of the peak counts of the transitions, which corresponds to the population of the excited states ( $\rho_{ee} = \Omega_R^2 / (\Gamma_{sp}^2 + 2\Omega_R^2)$ )<sup>4</sup>. Panel (c) is the dependence of the signal-to-background ratio (SBR) on the excitation power, and the fitting function is actually the ratio between the saturation curve from panel (b) and the linear corresponds of the leakage background to the laser power

$$\text{SBR}(P_{laser}) = \frac{\text{Signal}(P_{laser})}{\text{Leakage}(P_{laser}) + \text{DarkCounts}} \quad (3.1)$$

here,  $P_{laser}$  is the power of the excitation laser. After these calibrations, we will move on to reveal the electron spin dynamics in the next two sections.

<sup>3</sup>In chapter 1, Fig. 1.11 implies the SNR of DT is about 30 for the time constant of 100 ms and 24 dB/oct, which corresponds to the time resolution as 1s.

<sup>4</sup>With zero laser detuning ( $\Delta = 0$ ) and subtracting the laser leakage counts, Eq. (1.3) is proportional to  $\rho_{ee}$

## 3.2 Environmental couplings of electron spin in single quantum dot

As we introduced in Chapter 1, self-assembled QD provides us a physical environment with the effectively reduced dimension down to zero, but it still keeps the mesoscopic structure. The carriers trapped inside have different couplings with the environment. The electron spin dynamics studied here are the results of these couplings. Among them, the coupling with nuclear-spin environment, the coupling with phonon environment and the coupling with the Fermi sea of the back contact mainly dominate the electron behaviors, and will be studied in the following subsections.

### 3.2.1 Coupling of confined electron spin with nuclear-spin reservoir

As the lattice atoms constructing InAs/GaAs self-assembled QD, the Arsenic atom and Gallium atom both have the nuclear spin  $I_{As} = I_{Ga} = 3/2$ , and Indium atom has the nuclear spin  $I_{In} = 9/2$ . The hyperfine interaction considered is the Fermi contact interaction of an electron spin with a surrounding nuclear spin ensemble, the interaction Hamiltonian is written as: [44]

$$H_{hyp} = \nu_0 \sum_i^N A_i |\varphi^e(\mathbf{R}_i)|^2 (\mathbf{I}_i \cdot \mathbf{S}). \quad (3.2)$$

The sum runs over all nuclei  $i \in N$  in the lattice.  $\nu_0$  is the volume of a unit cell of the dot material,  $\varphi^e(\mathbf{R}_i)$  is the electron envelope wavefunction at the  $i$ th nucleus,  $\mathbf{I}_i$  and  $\mathbf{S}$  are the spin operators of nuclear and electron spins, respectively.  $A_i$  is the hyperfine coupling strength. If we span the electron spin subspace with two z-direction electron spin states  $|\downarrow\rangle$  and  $|\uparrow\rangle$  as the basis, the Hamiltonian above can be separated into two parts as the z component and the in-plane component, respectively.

$$H_{hyp} = \nu_0 \sum_i^N A_i |\varphi^e(\mathbf{R}_i)|^2 \left\{ I_{iz} S_z + \frac{1}{2} (I_{i+} S_- + I_{i-} S_+) \right\}. \quad (3.3)$$

Here, the in-plane part indicate the spin flip-flop process between the nuclear and electron spins. From the view of electron, this hyperfine interaction can also be treated as an effective magnetic field from the collective behavior of nuclei, which is

commonly referred to *Overhauser field* with the form of

$$\mathbf{B}_N = \frac{\nu_0}{\mu_B g_e} \left\langle \sum_i^N A_i |\varphi^e(\mathbf{R}_i)|^2 \mathbf{I}_i \right\rangle_N. \quad (3.4)$$

Here,  $\langle \dots \rangle$  is the quantum average over  $N$  nuclei in the ensemble. The nucleus number  $N$  is about  $10^4 \sim 10^5$  for InAs/GaAs dot.

We assume that the electron spin sees a static Overhauser field, so that the  $z$  component  $B_{Nz}$  will introduce a Zeeman splitting to the electron spin states along  $z$  direction, while the in-plane component  $B_{Nxy}$  will coherently couple the two spin states with the coupling strength  $\Omega_H$  [13] defined as:

$$\hbar\Omega_H = \frac{g_e \mu_B B_{Nxy}}{2}. \quad (3.5)$$

Statically, this coupling dresses the bare states ( $|\downarrow\rangle$  and  $|\uparrow\rangle$ ) to form the new eigenstates for the electron spin subspace in the form of

$$|\tilde{\downarrow}\rangle = \cos\phi |\downarrow\rangle - \sin\phi |\uparrow\rangle, \quad (3.6)$$

$$|\tilde{\uparrow}\rangle = \sin\phi |\downarrow\rangle + \cos\phi |\uparrow\rangle, \quad (3.7)$$

with  $\phi = \Omega_H/\omega_z$ , and  $\hbar\omega_z = g_e \mu_B (B_z + B_{Nz})$ .  $B_z$  refers the external magnetic field in Faraday configuration. The coefficients  $\cos\phi$  and  $\sin\phi$  in the form of above admixture states imply the hyperfine interaction induced electron spin dynamics can be suppressed under high external magnetic field, which can be understood as the portion of the Overhauser field in the total magnetic field becomes negligible.

In reality, due to the dipolar-dipolar interactions between nearby nuclear spins and electron spin mediated spin-flip events between distant nuclear spins [45], the Overhauser field fluctuates all the time. The correlation time of the nuclear spin is on the order of milliseconds, which is expected to be similar to the decay time of nuclear spin polarization in the presence of an electron in QD [46]. However, the assumption above of the static hyperfine field seen by electron spin is appropriate as long as the electron spin dynamics occur on a time scale much shorter than the nuclear spin correlation time. That is always the case when we optically excite the electron spin in InAs/GaAs self-assembled QDs, where the excitonic state has the lifetime on the order of hundred picosecond as we studied in Chapter 2. Therefore the fluctuation of Overhauser field is frozen for each excitonic event. Statistically,

the Overhauser field for each frozen moment follows a Gaussian distribution

$$f(\mathbf{B}_N) = \frac{1}{(2\pi)^{3/2} B_{nuc}^3} \exp\left(\frac{-|\mathbf{B}_N|^2}{2B_{nuc}^2}\right), \quad (3.8)$$

which gives

$$\begin{aligned} \langle \mathbf{B}_N \rangle &= 0 \\ \langle |\mathbf{B}_N|^2 \rangle &= 3B_{nuc}^2. \end{aligned} \quad (3.9)$$

The rms value  $B_{nuc}$  is typically estimated as 15 mT [13] for each spacial component of  $\mathbf{B}_N$  through our discussion in this thesis.

In terms of non-optical dynamics of electron spin in ground states, the fluctuation of the Overhauser field is the main cause for the dephasing of the electron spin states. We also note that the Fermi contact interaction relies on a finite Bloch wavefunction at the sites of the nuclei. Differently from the s-like symmetry of electron wavefunction, the p-like symmetry of wavefunction isolates hole from such interaction.

### 3.2.2 Coupling of confined electron spin with phonon reservoir

Besides the hyperfine interaction, spin-orbit (SO) coupling can also admix the spin ground states. The spin-orbit Hamiltonian ( $H_{SO}$ ) couples the states with both different orbital and different spin parts [47]

$$\langle nl \downarrow | H_{SO} | n'l' \uparrow \rangle \neq 0, \quad (3.10)$$

Here, the quantum numbers ( $nl$ ) and ( $n'l'$ ) indicate different orbital states. With first order perturbation, the non-normalized eigenstates due to the spin-orbit interaction can be written as [48]:

$$|\widetilde{nl \uparrow}\rangle = |nl \uparrow\rangle + \sum_{n'l' \neq nl} \frac{\langle n'l' \downarrow | H_{SO} | nl \uparrow \rangle}{E_{nl} - E_{n'l'} - \Delta E_z} |n'l' \downarrow\rangle, \quad (3.11)$$

$$|\widetilde{nl \downarrow}\rangle = |nl \downarrow\rangle + \sum_{n'l' \neq nl} \frac{\langle n'l' \uparrow | H_{SO} | nl \downarrow \rangle}{E_{nl} - E_{n'l'} + \Delta E_z} |n'l' \uparrow\rangle. \quad (3.12)$$

Here  $\Delta E_z = \hbar\omega_z = g_e\mu_B B_z$  is the unperturbed spin splitting. It is clear that electric field can not cause transitions between pure spin states, however, with the SO interaction, as the admixtures of spin and orbital states, the eigenstates can be coupled by electric field, and electric-field fluctuation can lead to the spin relaxation [47].



In semiconductors, the electric-field fluctuation comes from the phonon reservoir. First, deformation potential phonons inhomogeneously deform the crystal lattice, therefore altering the band gap in space, which gives the fluctuation of electric field. Second, in polar crystals such as GaAs, the homogeneous strain also leads to electric fields through piezoelectric effect. The spin-relaxation rate can be described by Fermi's golden rule [48],

$$\kappa_{phonon} = \frac{2\pi}{\hbar} \sum_{n,l} |\langle \widetilde{nl} \downarrow | H_{e,ph} | \widetilde{nl} \uparrow \rangle|^2 \mathcal{D}(\Delta E_z). \quad (3.13)$$

$H_{e,ph}$  is the Hamiltonian of electron-phonon coupling,  $\mathcal{D}(E)$  is the density of phonon states of energy  $E$ . With the typical magnetic field value of several tesla used in our lab for studying the spin relaxation process, we have the condition of  $g_e \mu_B B z \gg k_B T$ , the approximation below is valid [47, 49],

$$|\langle \widetilde{nl} \downarrow | H_{e,ph} | \widetilde{nl} \uparrow \rangle| \propto (g_e \mu_B B z)^{3/2}. \quad (3.14)$$

The density of the phonon states is proportional to the square of the energy. So the final dependence of spin-relaxation rate on the magnetic field is:

$$\kappa_{phonon} \propto (g_e \mu_B B z)^5. \quad (3.15)$$

For the small magnetic field case, where  $g_e \mu_B B z \ll k_B T$ , the dependence is replaced by  $\kappa_{phonon} \propto (g_e \mu_B B z)^4$ .

We notice that, neither SO coupling or electron-phonon coupling can individually result in the spin-relaxation. SO coupling provides the states admixtures so that phonon can couple the spin ground states and provide the energy cost to realize the dissipative spin flip. It also has been proposed that phonon assisted hyperfine interaction can lead to the spin relaxation [50]. There the dependences of  $\kappa_{hypp} \propto B^2$  and  $\kappa_{hypp} \propto B^3$  are predicted according to the different magnetic field ranges. However, the rate  $\kappa_{hypp}$  will be less than 1 Hz at 1 Tesla considering the large quantization energy of our InAs/GaAs dot, which can be neglected compared with phonon assisted SO interaction. Any other mechanisms leading to the slow spin relaxation are not considered here either.

### 3.2.3 Coupling of confined electron spin with Fermi sea

In our sample, under the QDs layer, we have one highly n-doped GaAs layer as the back contact of our diode structure. This n-doped layer is also the nearest Fermi sea

around the QDs. The first order coupling interaction between QD and Fermi sea is the electron tunneling, which is utilized to charge and de-charge the QDs. The second order coupling interaction is the exchange process between the electrons in the QDs and the Fermi sea, respectively. This coupling is named as “cotunneling” and reaches its maximum rate at the intersection where the charge states in QD are switched, and gets strongly suppressed when the charge state is stable [13]. Involving the Fermi sea as the electron spin reservoir, cotunneling leads to the electron spin relaxation process [51, 52], which can be utilized to randomize the spin states.

### 3.2.4 Hole mixing

Although the valence-band mixing in QDs is dramatically reduced compared with the case of quantum well, it is still, nevertheless, expected to play a role in QD dynamics. The hole mixing discussed here is referred as mixing between heavy holes and light holes in the valence band, for example,

$$|\widetilde{\uparrow}\rangle = | + 3/2\rangle + \epsilon_+ | + 1/2\rangle + \epsilon_- | - 1/2\rangle, \quad (3.16)$$

and we define  $|\epsilon_{hl}|^2 = |\epsilon_+|^2 + |\epsilon_-|^2$  as the hole mixing strength, which is estimated on the order of few percent for InAs/GaAs QD [53].

Through optical transitions, electron spin and hole spin can be linked together. The hole mixing results in the admixture of excited states respect to the electron spin ground states, which implies an important role of hole mixing in electron spin-flip process. For example, by absorbing  $\sigma_+$  photon, electron spin  $|\uparrow\rangle$  state is excited to form a trion state as  $|\uparrow\downarrow\widetilde{\uparrow}\rangle$ . Then, through the decay channel involving light hole spin  $| + 1/2\rangle$  and electron spin  $|\uparrow\rangle$ , the excited QD emits one  $\sigma_+$  photon and leaves an electron spin  $|\downarrow\rangle$  state as the ground state. So that the electron spin is flipped.

## 3.3 Direct measurements of quantum dot spin dynamics

In this section, we apply n-shot time-resolved resonance fluorescence (TRRFL) measurements to reveal the electron spin dynamics discussed in last section. To investigate the spin dynamics of singly confined electron in single QDs, a finite magnetic field is required to lift the spin degeneracy. In our case, the external magnetic field is applied in Faraday configuration. What we are concerning about the measurements in this section are the time scales, which includes the measurement time  $T_m$ , the

characteristic time  $T_{BA}$  for the back action induced by the measurements, and the characteristic time  $T_1$  for spin relaxation. With the condition of

$$T_m < T_1 < T_{BA}, \quad (3.17)$$

we can reveal the spin relaxation dynamics before inducing the back action to the system; with the condition of

$$T_m < T_{BA} < T_1, \quad (3.18)$$

although we can still reveal the back-action dynamics, the spin relaxation is fully affected by the measurement and no natural properties can be extracted. The worst case for the study of spin dynamics is

$$T_{BA} < T_m, \quad (3.19)$$

where, the measurement fully erases the information of any spin-dynamics.

About the measurement  $T_m$ , we can make an estimation by analyzing our instruments involved. In the experimental setup, after the background suppression polarizer (seen in Fig. 2.3 (b), the polarizer on the collection arm before the fiber coupler), RFL photons are directly coupled into a fiber and led to an avalanche photodiode (APD), which is set in free-running mode. There is one switch circuit<sup>5</sup> with the time resolution about 6 ns between APD and the data acquisition system<sup>6</sup>. The data acquisition system has the time resolution 800 ns. We will see in the next subsection, the time resolution of n-shot TRRFL is only limited by the switch circuit, so we can set  $T_m$  any value larger than 6ns. From previous studies [12, 13, 47, 49], the  $T_{BA}$  is estimated on the order of microseconds and spin-relaxation time  $T_1$  is normally on the order of milliseconds, so at least we can avoid the condition (3.19) to study some of the electron spin dynamics.

### 3.3.1 Optically induced back action on electron spin — Spin pumping

Firstly, we would like to study the dynamics of measurement induced back action on electron spin in single QDs by quantifying the time scale of  $T_{BA}$ . This back action results in the spin-flip event of electron, thereby it is also referred to “Spin Pumping” which was studied recently by using DT technique [12].

Here, we revisit the DT measurements first, and then provide our RFL solution

---

<sup>5</sup>Mini-Circuits, ZYSWA-2-50DR

<sup>6</sup>National Instruments, PCIe-6259

for a direct measurement on the spin-pumping timescale  $T_p$ , which represents  $T_{BA}$  in this particular case. As shown in Fig. 3.3 (a), with zero external magnetic field, we got the whole  $X^{1-}$  transition plateau by two dimensional DT scan. With finite

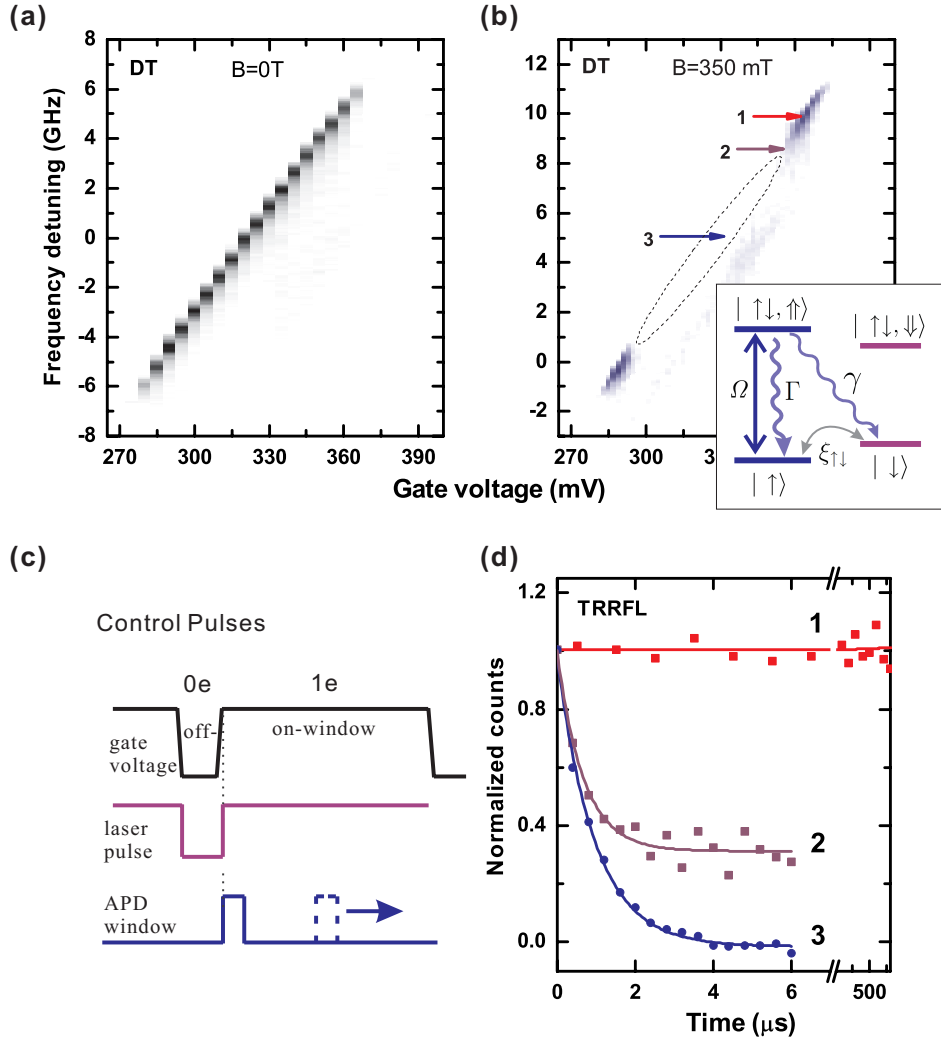


**Figure 3.3:** Electron spin pumping and time-resolved resonance fluorescence measurement. (a) 2D DT of  $X^{1-}$  transition plateau at zero magnetic field. (b) The blue Zeeman branch of  $X^{1-}$  transition under 350 mT magnetic field. The insert shows the reduced four-level system in our single QD system and the relative transitions. Here we didn't specify the admixing states from pure spin state by different labels. (c) The control traces of gate, laser and APD for the n-shot TRRFL measurement. (d) The TRRFL data for three locations labeled in panel (b).

external magnetic field in Faraday configuration, we have the Zeeman splitting, but the middle part of the each Zeeman transition is missing, for example the blue transition as shown in Fig. 3.3 (b). That is the result of spin pumping, which can be described through the insert of Fig. 3.3 (b). As we discussed in Chapter 1, in this

reduced four level system. in principle, only the direct optical transitions are allowed as  $|\uparrow\rangle \leftrightarrow |\uparrow\downarrow\uparrow\rangle$  and  $|\downarrow\rangle \leftrightarrow |\downarrow\uparrow\downarrow\rangle$ . However, these rely on the assumption that both the ground states and excited states are the un-coupled states. From the discussion in Subsection 3.2.1, we know the hyperfine interaction results in the admixture of the electron spin ground states. From the discussion in Subsection 3.2.4, we know the hole mixing results in the admixture of the excited states. Both the ground states mixing and the excited states mixing can enable the indirect transition channel in the insert of Fig. 3.3 labeled by the decay rate  $\gamma$ . Back to our measurement, when we optically drive the blue transition for example, after several direct cyclings, the electron spin will end up at the other spin state. For DT measurement, enough transition cycling is required for getting the signal out of the noise floor. Normally, the indirect transition has the strength 1000 times weaker as direct transition, but thousand cyclings is far from enough to get DT signal, so we miss the middle part of the transition plateau. The two edges of the plateau are in the situation we discussed in Subsection 3.2.3, where the electron in the QD can exchange its spin with the electron reservoir in the back contact by cotunneling. Through this process, the electron spin can be randomized so that the direct transition cyclings can be preserved with a certain rate and the DT signal is visible.

For determining the time scale of this spin-flip process, we carry out the n-shot TRRFL measurement with the merit of much more fine time resolution down to 6 ns compared with DT which is intrinsically limited by lock-in technique. Figure. 3.3 (c) shows the temporal control traces for gate, laser and APD respectively. For each cycle ( $T_{cycle}$ ) of the n-shot, we control the gate to switch from off-window to on-window, where the off-window corresponds to the case of no electron in QD and the on-window corresponds to the case of single electron charging, so that we can artificially randomize the electron spin in a control way. Simultaneously with the gate switched to on-window, the laser is switched on as well and set to be resonant with one of the transitions, for example the blue transition in our discussion here. The large repetition number ( $n \sim 10^5$ ) guarantees the enough photon counts with small integration time of APD and meanwhile fulfill the condition  $n \times T_{cycle} > 800$  ns for getting rid of the acquisition time limitation. We walk the APD on-window within the gate on-window, pin down the scattered photon numbers statistically before the spin flipped at different time delays, eventually, we map out the TRRFL as shown in Figure. 3.3 (d). There we present three sets of data corresponding to the

three locations labeled as 1,2,3 in the 2D-DT of Figure. 3.3 (b). Location 1 is the middle of cotunneling region where the fast electron spin exchange blocks any spin-pumping effort resulting in the time independent RFL data (red square) as shown in Fig. 3.3 (d). Location 2 is the edge of the cotunneling region, where the spin exchange can only partially block the spin-pumping process resulting in the purple square data in Fig. 3.3 (d). We fit the data by solving the master equation of three-level system [13] to extract the cotunneling rate as  $\xi_{\uparrow\downarrow} = 2\pi \times 37$  KHz. Location 3 is the middle of the  $X^{1-}$  plateau, where the electron spin can be efficiently pumped to  $|\downarrow\rangle$  state as the exponential decay data shown in Fig. 3.3 (d) (blue square), and the spin-pumping time ( $T_p$ ) or the spin-pumping rate ( $1/T_p$ ) can be directly extracted here.

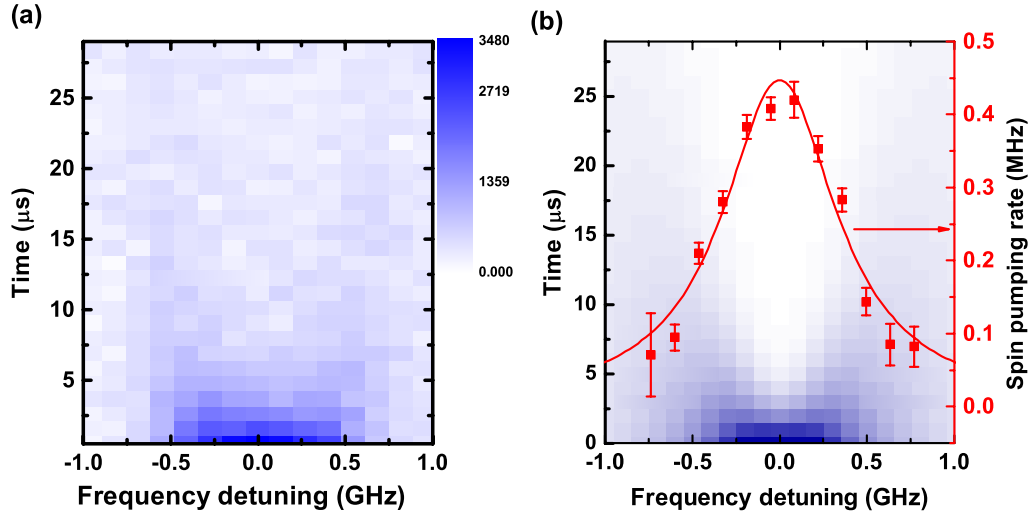


**Figure 3.4:** Dependence of the spin-pumping rate as a function of the excitation laser frequency detuning for a fixed laser power of 4nW. The magnetic field is 350 mT in Faraday configuration. (a) A two-dimensional map of the recorded time-resolved resonance fluorescence photon counts for a range of excitation laser frequency detuning. (b) The blue density 2D plot is the simulation of panel (a) by solving master equations, the red data and the red fitting curve are the extracted spin-pumping rates and their Lorentzian fit, respectively.

By fixing laser power and gate voltage applied on the sample, we measure the spin-pumping rate versus laser detuning as shown in Fig. 3.4. Panel (a) records the raw data of TRRFL for different laser detuning. Panel (b) shows the 2D simulation of panel (a) by calculating three-level master equations. The extracted spin-pumping rates (red square data) are also shown in panel (b) and fitted by a Lorentzian (red curve).

Through above two-dimensional TRRFL measurements, we can determine the resonance for certain excitation power, and then we carry out power dependent TRRFL measurements resonantly as shown in Fig. 3.5. By increasing excitation power, the spin-pumping time becomes shorter, or equivalently the spin-pumping rate becomes larger, and tends to reach saturation.

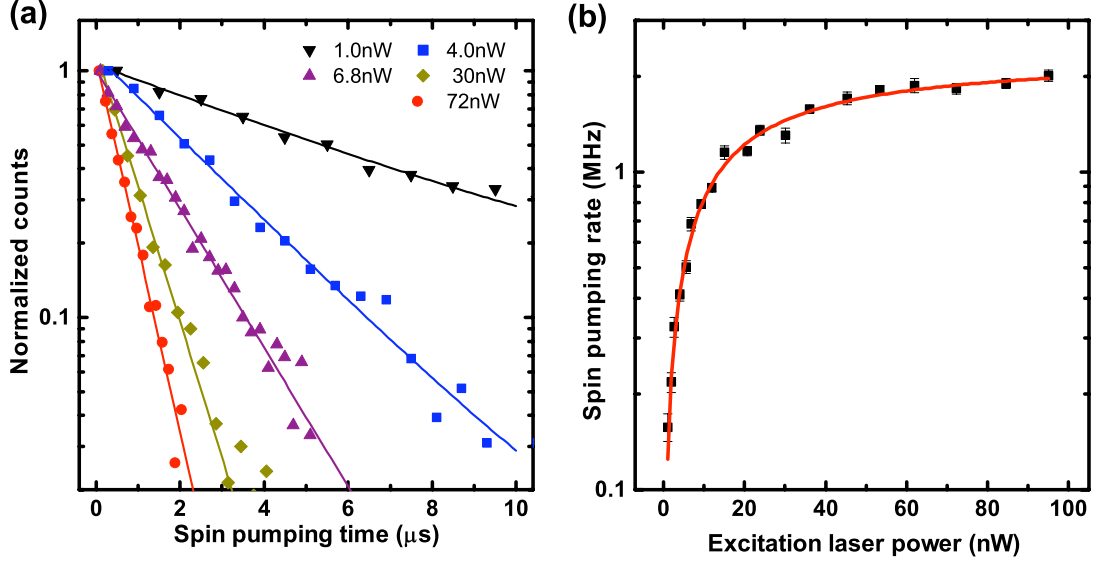


**Figure 3.5:** Dependence of the spin-pumping rate as a function of the excitation laser power. The magnetic field is 350 mT in Faraday configuration. (a) The raw data of the time-resolved resonance fluorescence for a range of different laser powers. The laser frequency is on resonance with the  $X^{1-}$  transition. (b) The extracted spin-pumping rate, which tend to saturation with the excitation power increasing.

For quantitatively studying the spin flip, we define a branching ratio  $\eta$  as  $\eta = \gamma/(\gamma + \Gamma)$  [13], which quantifies the normalized number of photons scattered by the transition before the electron flips its spin. With a fixed branching ratio, the spin-pumping rate is determined by the population of the excited state  $|\uparrow\downarrow\uparrow\rangle$ , which has been demonstrated above by the measurements of the dependence of spin-pumping rate on laser detuning and power under a fixed magnetic field. To elucidate the two physical mechanisms which mediate the optical induced spin flip, we study the magnetic field dependence of  $T_p$  ( $1/T_p$ ). The laser power is set well above the saturation power, the laser is resonant with transition and gate voltage are fixed at the position 1 in Fig. 3.3 (b) for each magnetic field value. Figure 3.6 presents the magnetic field dependence of spin-pumping rate. Each data point is extracted from TRRFL on resonance. The fitting curve includes the functional

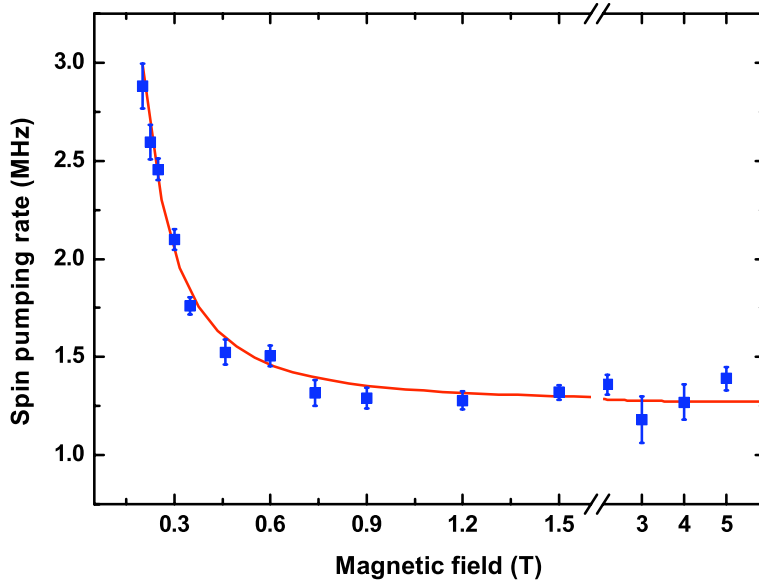


**Figure 3.6:** The magnetic field dependence of the spin-pumping rate with a fixed laser power of 60 nW. The lowest magnetic field value of selected to ensure the electronic ground states are split by  $\sim 1.5$  GHz which is 3 times the transition linewidth.

dependence on magnetic field of hyperfine interaction and hole mixing that admix the spin states coherently. In the low magnetic field limit, the hyperfine interaction efficiently mediates the spin-flip events and result in a quadratic variation of the spin-pumping time with applied external magnetic field according to  $(B_{nxy}/B_{ext})^2$ . Whereas, for magnetic field beyond 0.6 T, hole mixing mediates the spin-pumping process and contributes a constant spin-pumping rate about 1.27 MHz independent of the external magnetic field. The theoretical curve is obtained using an RMS in-plane nuclear field  $B_{nxy} = 15$  mT. The corresponding heavy-light hole mixing strength is  $|\epsilon_{hl}| = 2.8\%$ , which is within the estimated range based on previous reports using DT measurements [13]. We do note that the value of hole-mixing strength will vary among QDs due to the shape anisotropy and the large variation of hole-spin g-factor.

As a short summary, we note that the back action induced by measurement on single electron spin confined in single QD is the spin pumping. The n-shot TRRFL is a type of measurement with  $T_m \ll T_P(T_{BA})$ , which let us reveal the back-action dynamics.



### 3.3.2 Observed electron spin relaxation in single quantum dot

The electron spin relaxation happens between two electron eigenstates, and the idea of measuring spin relaxation is to initialize the electron spin in one of the eigenstates first and then statistically measure the spin-flip events to the other eigenstate. The temporal control traces for gate, laser and APD are shown in Fig. 3.7 (a), respectively. For each control cycle, we randomize the electron spin states by switching the

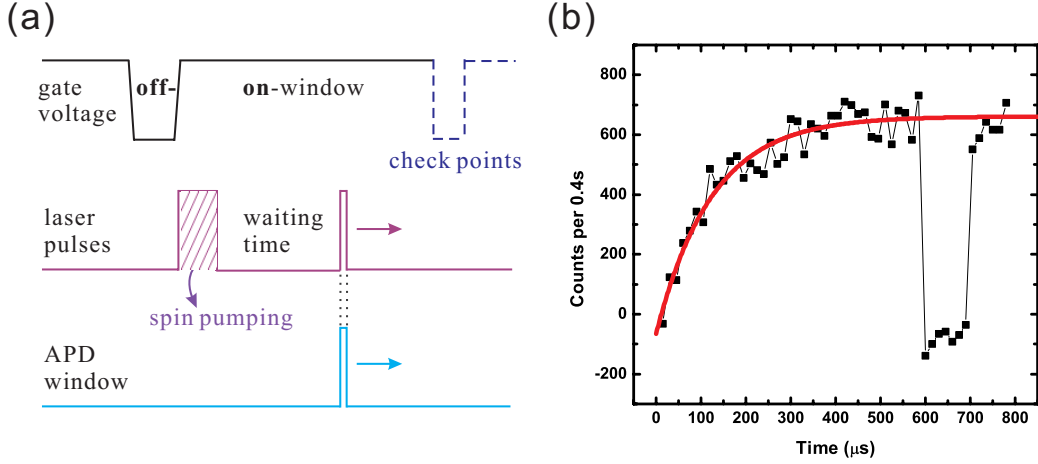


**Figure 3.7:** The n-shot TRRFL measurement for electron spin relaxation. (a) The temporal control traces for gate, laser and APD. (b) The TRRFL data for electron spin relaxation at 6 T. The red curve is fitted to the data for extracting the  $T_1$  time.

gate between off- and on- window. When the gate is in on-window, laser is turned on immediately to be resonant with blue transition ( $|\uparrow\rangle \leftrightarrow |\uparrow\downarrow\uparrow\rangle$ ) here for a time duration  $50\ \mu\text{s}$  to ensure the electron spin being initialized to spin-down state ( $|\downarrow\rangle$ ) through spin pumping process. Then the electron is left in the dark for a waiting time spanning  $0 \sim 20\ \text{ms}$ . The laser is then turned back on for  $5\ \mu\text{s}$  coinciding in time with the APD detection window. An optional check-points gate window is set to check both the background and the RFL counts corresponding to the electron spin thermalization which could be our reference for data fitting. One set of TRRFL data in Fig. 3.7 (b) shows the measured signal recovery under 6 T magnetic field. Initially, electron still resides in the dark spin down state  $|\downarrow\rangle$  and no photon scattering occurs. As time progresses, and the probability that the electron has flipped its spin increases, the probability to scatter photons also increases. Using the function:

$$\rho_{\uparrow\uparrow} \sim a(1 - e^{-t/T_{eff}}), \quad (3.20)$$

we can extract a corresponding effective spin-flip time for this certain magnetic field. The spin-relaxation time  $T_1$  can then be extracted from  $T_{eff}$ , and we will explain it as following. The time  $T_1$  is denoted by  $T_{\uparrow\downarrow}$  for spin relaxation process from  $|\uparrow\rangle$  to  $|\downarrow\rangle$  and by  $T_{\downarrow\uparrow}$  for the process from  $|\downarrow\rangle$  to  $|\uparrow\rangle$ . Then we have the rate equation for  $\rho_{\uparrow\uparrow}$  as

$$\dot{\rho}_{\uparrow\uparrow}(t) = -\frac{1}{T_{\uparrow\downarrow}}\rho_{\uparrow\uparrow}(t) + \frac{1}{T_{\downarrow\uparrow}}\rho_{\downarrow\downarrow}(t), \quad (3.21)$$

and

$$\rho_{\downarrow\downarrow}(t) = 1 - \rho_{\uparrow\uparrow}(t). \quad (3.22)$$

By solving this differential equation with the initial condition  $\{\rho_{\uparrow\uparrow}(0), \rho_{\downarrow\downarrow}(0)\} = \{1, 0\}$ , we get:

$$\rho_{\uparrow\uparrow}(t) = 1 - \frac{1}{T_{\uparrow\downarrow} + T_{\downarrow\uparrow}} \left[ T_{\uparrow\downarrow} + T_{\downarrow\uparrow} \exp \left( -\frac{T_{\uparrow\downarrow} + T_{\downarrow\uparrow}}{T_{\uparrow\downarrow}T_{\downarrow\uparrow}} t \right) \right]. \quad (3.23)$$

We define

$$T_{eff} = \frac{T_{\uparrow\downarrow}T_{\downarrow\uparrow}}{T_{\uparrow\downarrow} + T_{\downarrow\uparrow}}, \quad (3.24)$$

which can be extracted from the TRRFL measurement directly. Considering the thermal equilibrium  $\rho_{\uparrow\uparrow}(\infty) = 0$  and Boltzmann distribution, we get

$$\frac{T_{\uparrow\downarrow}}{T_{\downarrow\uparrow}} = \exp \left( \frac{g_e \mu_B B_z}{K_B T} \right), \quad (3.25)$$

so that, by knowing  $T_{eff}$ , we can calculate  $T_{\uparrow\downarrow}$  and  $T_{\downarrow\uparrow}$  respectively.

Figure 3.8 (a) shows a set of TRRFL data for different magnetic fields, the extracted  $T_{eff}$  are recorded as the red circles in panel (b), and the corresponding  $T_{\uparrow\downarrow}$  are recorded as the red squares in panel (c). The highest measured  $T_{eff}$  of 17.3 ms at 2.2 Tesla corresponding to  $T_{\uparrow\downarrow}$  of 31.3 ms. The red curves in panel (b) and (c) are the fitted to the data using  $C * B^{-m}$ , and we get the  $m = 4.87(17)$  for panel (b) and  $m = 5.02(17)$  for panel (c), which imply the dynamics of spin relaxation we are studying here is dominated by phonon assisted SO coupling as we discussed in Subsection 3.2.2. We notice that, firstly, even with condition  $K_B T > g_e \mu_B B_z$ , we still have the  $T_1$  power dependence of  $B^{-5}$ ; secondly, our  $T_1$  results shown to be shorter than the average value from a QD ensemble measured in [54], the discrepancy may be due to the anisotropy enhanced spin-orbital coupling for our single QD case.

Another feature we would to show is that we could precisely calculate the spin-

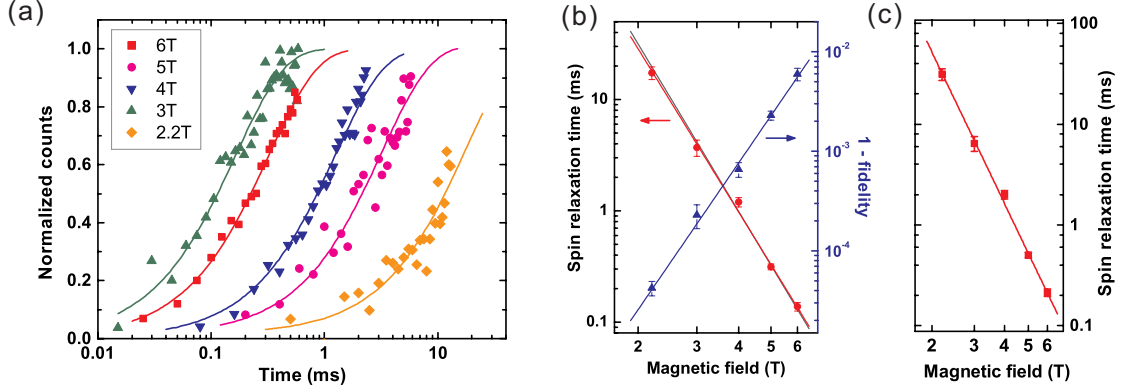


**Figure 3.8:** The  $n$ -shot TRRFL measurements for spin relaxation. (a) The TRRFL data under different magnetic fields. (b) The extracted  $T_{eff}$  shown as red circles from the data in panel (a). The red fitting curve gives the power dependence of about  $B^{-4.87}$ . As a comparison, the black curve corresponds to the power dependence of  $B^5$ . Blue triangle data are the calculated 1-fidelity for spin pumping. (c) The calculated  $T_{1\uparrow}$  from  $T_{eff}$  data of panel (b). The red fitting curve gives the power dependence of about  $B^{-5.02}$ .

pumping fidelity from our  $T_p$  and  $T_1$  measurements. The fidelity is defined as

$$Fidelity = 1 - T_p/T_{eff}. \quad (3.26)$$

The calculated  $T_p/T_{eff}$  data are shown as the blue triangles in Fig. 3.8 (b), and the maximum corresponding fidelity there is 99.996% at 2.2 Tesla.

As a short summary, we note that, in our  $T_1$  measurement, we didn't introduce any measurement induced back action, since we let electron relax its spin in the dark. Therefore, we have  $T_{BA} \rightarrow \infty$ . Overall, we fulfill the condition  $T_m < T_1 < T_{BA}$ , so that we can reveal the spin-relaxation dynamics.

### 3.3.3 Towards single-shot measurement of an electron spin

It is always of great interest to attempt fast readout of quantum states. The fine time resolutions of the  $n$ -shot measurements discussed above only work for resolving the statistical properties of the physical dynamics. If we want to record the real-time response from the system, single-shot measurement is required. Figure 3.9 illustrates the ideas for  $n$ -shot measurement and single-shot measurement, respectively. For  $n$ -shot measurement shown in panel (a). The time  $t_{m1}$  denotes the pulse duration of each shot there. One  $n$ -shot data is accumulated equivalently to the time duration of  $n \times t_{m1}$ . Therefore the high SNR and fine time resolution can be

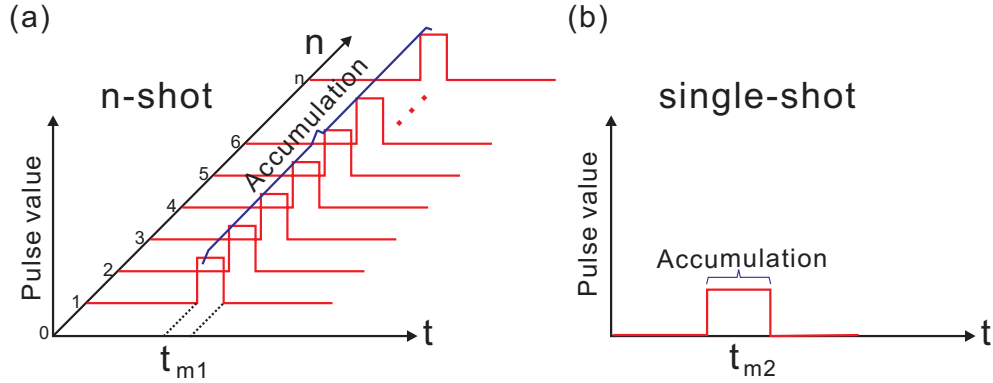


**Figure 3.9:** The schematic for the ideas of n-shot measurement and single-shot measurement. (a) The three dimensional pulse traces illustrate the n-shot data accumulation. (b) The two dimensional pulse trace illustrates the single-shot data accumulation.

achieved simultaneously by selecting big number of  $n$ . For single-shot measurement shown in panel (b), the pulse duration  $t_{m2}$  is the data-accumulation time as well as the measurement resolution, as a result, there is a trade off for reaching high SNR and fine time resolution at same time.

For calibrating our system for single-shot measurement, we switch off the magnetic field for spin-free transition probing as we did in Section 3.1. In Fig. 3.10 we present 100 ms worth of real time RFL counts with  $10 \mu\text{s}$ ,  $30 \mu\text{s}$  and  $50 \mu\text{s}$  time bin, respectively. For each set of data, the first 50 ms time trace is obtained when trion transition is resonant with the excitation laser at  $\sim 10$  times the saturation power. The second 50 ms part is obtained when the transition is far off resonance with the laser dictating the overall background level. Compared with SNR, the value of readout error is more convenient to indicate the readout ability in photon-count measurement. The readout error is defined as  $\epsilon = 0.5(\epsilon_{on} + \epsilon_{off})$  [55], where  $\epsilon_{on}$  ( $\epsilon_{off}$ ) is the fraction of declared to be off (on) since the count is below (above) the set threshold. With a threshold of 0.5 we deduce measurement fidelities ( $1 - \epsilon$ ) of 0.63, 0.77 and 0.84 for the  $10 \mu\text{s}$ ,  $30 \mu\text{s}$  and  $50 \mu\text{s}$  time bin, respectively. These numbers are satisfactory when compared with spin relaxation timescales, therefore the single-shot readout is in principle possible with sufficient margin with respect to all spin relaxation time of Fig. 3.8 (b). However, for finite magnetic fields the optically induced back action time sets the natural limit for a non-destructive readout in trionic transition of a single QD, where the measurement time is required much shorter than  $1 \mu\text{s}$ . In a word, for the single-shot measurement using our experimental setup right now, we are in the condition of  $T_{BA} < T_m < T_1$ , which implies no electron

spin information can be extracted by single-shot readout. There are two ways to solve this issue. The first one is to increase the RFL photon collection efficiency by using microcavity for example, so that the  $T_m$  can be reduced. When  $T_m < T_{BA}$ , the dynamics of back action can be resolved. The other solution is to avoid back action or to slow down its process. This solution is more powerful since it can lead to  $T_m < T_{BA} < T_1$  or  $T_m < T_1 < T_{BA}$ , and the second condition corresponds to the non-destructive measurement. Suppressing back action requires new QD structures, which is exactly what we would like to discuss from next chapter, we will propose one single-shot electron spin readout experiment in the system of coupled quantum dots pairs.

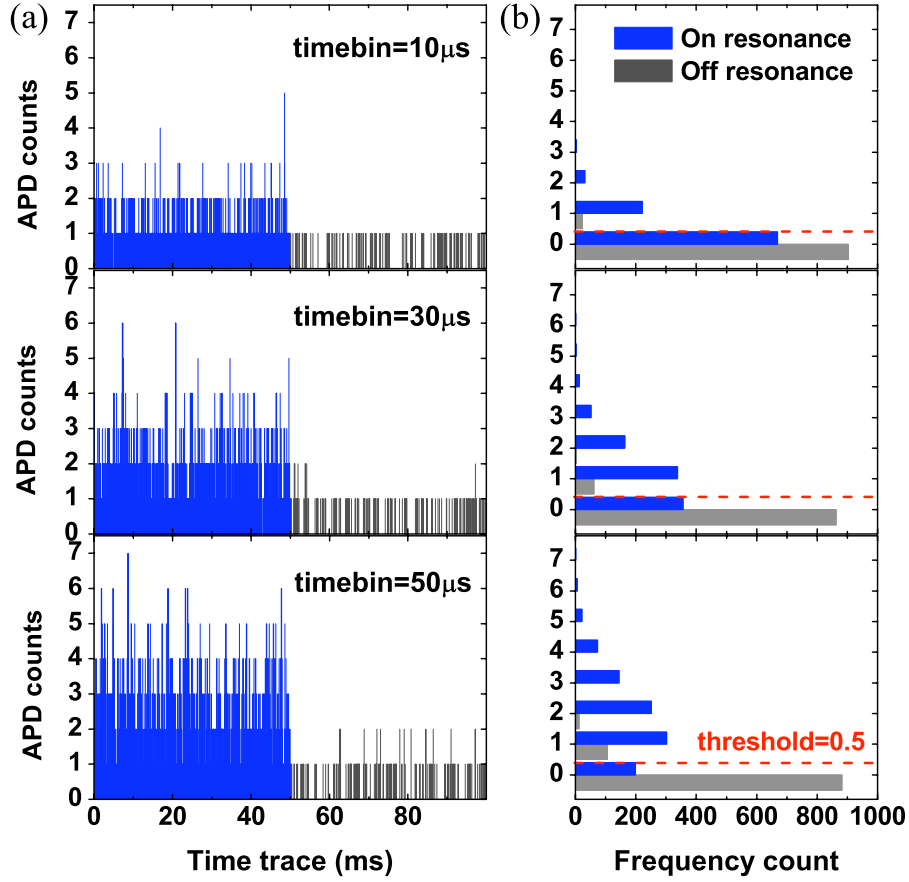


**Figure 3.10:** Single-shot readout for  $X^{1-}$  transition at zero magnetic field. (a) Real-time monitoring of the photon stream scattered from the  $X^{1-}$  transition at zero magnetic field (first 50 ms) and the background detection events (second 50 ms) for an integration time of 10, 30 and 50  $\mu$ s. (b) The corresponding histograms of detection events for each integration time bin. The threshold of 0.5 is indicated by the horizontal dashed lines.

## Chapter 4

# Charge and spin configurations in coherently coupled quantum dots

In this chapter, we start to investigate the optical properties of a system formed by two vertically stacked QDs, which has been discussed in Chapter 1 from the view of sample-growth technique. Instead of being two individual quantum systems, the two stacked QDs are coupled together by sharing the confined carriers, similarly to a two-atom molecule. Thereby, a pair of coupled QDs (CQDs) is also referred to a “Quantum-Dot Molecule”. The coupling strength corresponds to the rate of carriers’ tunneling through the potential barrier between two QDs. Due to this tunnel coupling, the original electronic energy levels of the two QDs are hybridized [56], resulting in rich spectral signatures [57, 58, 59, 60, 61]. Before the detailed discussion in this chapter, we would like to give an overview on how the rich spectral signatures of CQDs look like. Figure 4.1 presents a set of PL data from one dot of a coupled pair. There, each anti-crossing in the data indicates the strong electron-tunnel coupling for a certain charge and spin configuration. Our discussion in this chapter will be focused on revealing these charge and spin configurations. We will present our theoretical model, and then match the simulations to our experimental data to explain the dynamics involved. All these will help us to propose more sophisticated applications for near future study.

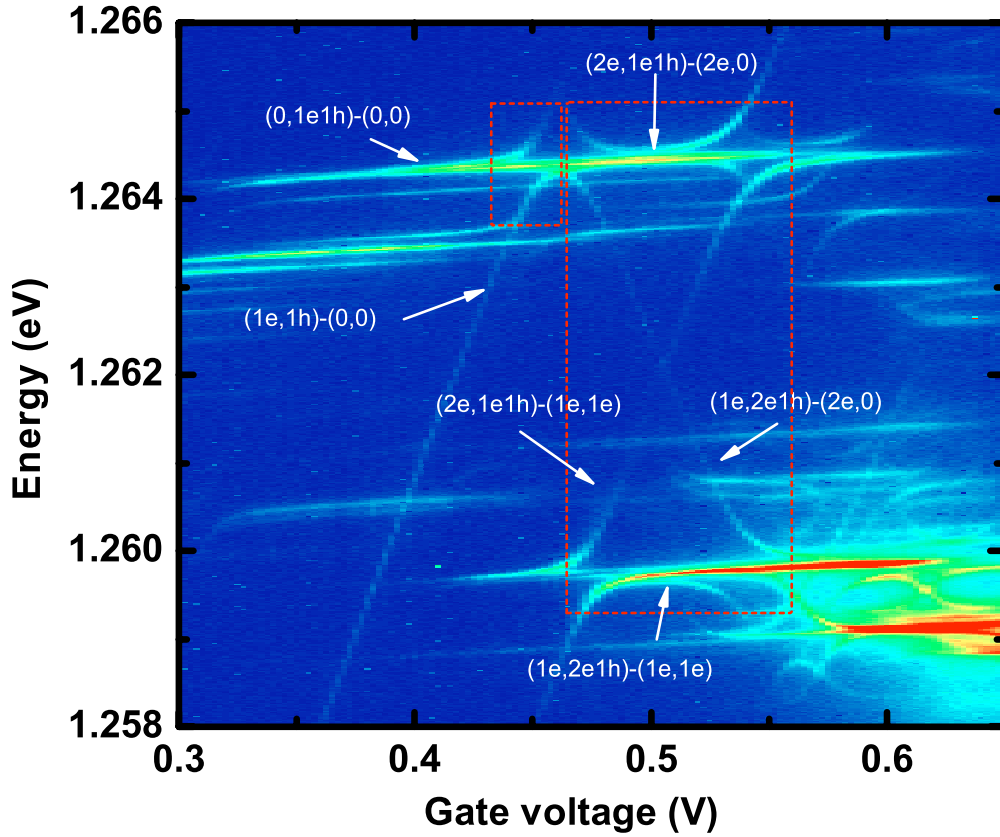


**Figure 4.1:** Gate sweep of photoluminescence spectrum for the red dot of a coupled quantum dots pair (CQD1) with the tunneling barrier of 13 nm. Two red dashed boxes indicate two studying areas which will be covered in the following text.

## 4.1 Samples and methods

The band-structure diagram of the gated CQDs is shown in Fig. 4.2 (a). The vertical stacked CQDs sample consists of two QD layers separated by a tunneling barrier (spacing layer) of thickness  $d_1$  and another tunneling barrier between the bottom QD layer and the back contact which is labelled  $d_2$ . The CQD1 and CQD2 covered in this thesis are from a wafer with tunneling barriers of  $d_1 = 13$  nm and  $d_2 = 30$  nm. As we discussed in Chapter 1, generally the QDs from the top layer are optically shifted to the red side of the QDs from the bottom layer, so we label the QDs from the top layer as the “Red(R)” dots and the QDs from the bottom layer as the “Blue(B)” dots. With this stack configuration, the paired QDs are preferably coupled by tunneling of conduction-band electrons.  $E_c$  and  $E_v$  in Fig. 4.2 (a) represent the conduction band



energy and valence band energy respectively;  $E_f$  is the fermi energy level;  $V_0$ , around  $-0.7$  V, is the conduction band offset of the Schottky contact. The positive gate voltage  $V_{Gate}$  was applied to reduce this band offset. In Fig. 4.2 (a), we also define a parameter  $\Delta$  as the s-shell electric level detuning of the blue dot with respect to the red dot. When  $V_{Gate}$  is increased,  $\Delta$  will be decreased, and  $V_{Gate}$  and  $\Delta$  are linearly dependent on each other,

$$V_{Gate}(\Delta) = -|a|\Delta + b. \quad (4.1)$$

Here  $a$  and  $b$  are constant parameters determined by the sample structure. Figure 4.2 (b) shows the CQDs schematic used in the following figures, which describes the charge configurations.

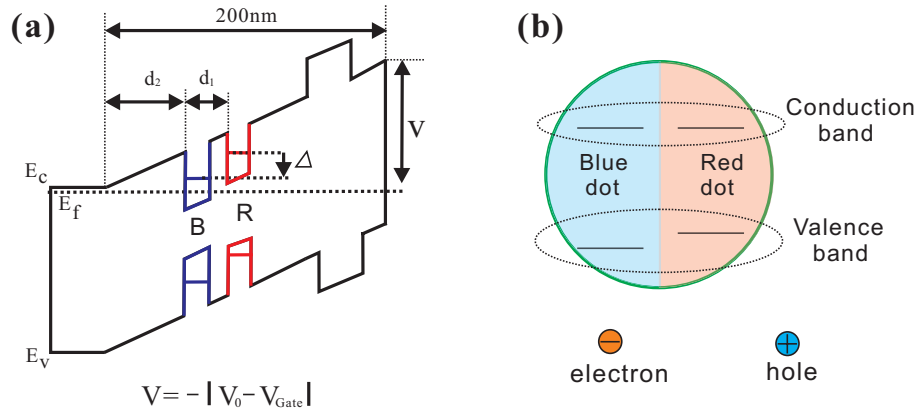


**Figure 4.2:** (a) The energy band diagram of the vertically stacked CQDs. Due to the different confinements, the two dots are labeled as “B”(blue) and “R” (red), respectively. (b) The CQDs schematic used in the following figures.

The measurements performed in this chapter are Photoluminescence (PL) and differential transmission (DT) at 4.2 K under zero external magnetic field. According to the discussion about the gate controlled PL in Chapter 1, the thick tunneling barrier  $d_2$ , and high power excitation will result in the overlap of charge plateaus. In CQDs, this will lead to more complicate spectrum which can not be observed in DT. However, DT provides much higher spectral resolution for unambiguously revealing the fine structures due to the spins. Although lacking for the rich spectrum, DT provides deterministic probing of the transition with static ground states. This is essential for any control experiments.

## 4.2 The basic interactions

The total Hamiltonian of the CQDs system is written as,

$$H_{tot} = H_0 + H^c + H_{e-h}^{ex}, \quad (4.2)$$

which contains the single particle energy  $H_0$ , the charge-charge Coulomb interaction  $H^c$  and the electron-hole exchange interaction  $H_{e-h}^{ex}$ .

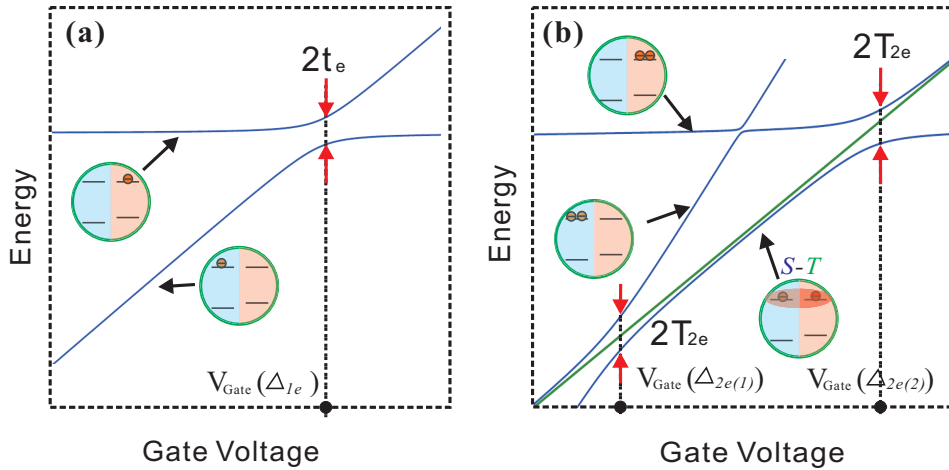


**Figure 4.3:** The schematic energy dispersion diagram for the singly charged (a) and doubly charged (b) CQDs ground states, respectively.

### 4.2.1 One-electron ground states: $1e$ system

The simplest case is single electron sitting in the coupled system. There is no Coulomb interaction and e-h exchange interaction. The coupling is given by the electron tunneling through the barrier. We define the electron states in the blue (B) dot and the red (R) dot as,

$$|1\rangle_{(1e)} = e_B^\dagger |0\rangle, \quad |2\rangle_{(1e)} = e_R^\dagger |0\rangle,$$

here  $e_{B(R)}^\dagger$  is the electron creation operator in blue (red) dot. The Hamiltonian of the system with the states above as the basis is,

$$H_{tot(1e)} = \begin{pmatrix} \varepsilon_B & t_e \\ t_e & \varepsilon_R \end{pmatrix} = \begin{pmatrix} \varepsilon_R & 0 \\ 0 & \varepsilon_R \end{pmatrix} + \underbrace{\begin{pmatrix} -\Delta & t_e \\ t_e & 0 \end{pmatrix}}_{H_{(1e)}}. \quad (4.3)$$

Here  $\varepsilon_{B(R)}$  is the single particle energy defined as  $\varepsilon_{B(R)} = \langle 0 | e_{B(R)} H_0 e_{B(R)}^\dagger | 0 \rangle$  and  $\varepsilon_B = \varepsilon_R - \Delta$ . Since the diagonal single particle energy term can be extracted as a constant part from the total Hamiltonian even for the multi-carriers cases, and it does not reflect the signature of the system, we will neglect this term in the following analysis. The off-diagonal element  $t_e$  is the single electron tunneling rate defined as  $t_e = \langle 0 | e_B H_{(1e)} e_R^\dagger | 0 \rangle$ . The eigenstates of  $H_{(1e)}$  are admixtures of the uncoupled states  $|1\rangle_{(1e)}$  and  $|2\rangle_{(1e)}$  due to non-zero off-diagonal term. We calculate eigenvalues of  $H_{(1e)}$  for a gate-voltage range and get an energy dispersion diagram as shown in Fig. 4.3 (a), which indicates the evolution of the eigenstates under gate control. The anti-crossing of the eigenstates is the signature of electron tunnel coupling. At the gate voltage  $V_{Gate}(\Delta_{1e})$ , where the two uncoupled states are resonant ( $\Delta_{1e} = 0$ ), the energy splitting between the two eigenstates indicates the coupling strength which is  $2t_e$  for the  $1e$  system. In the following discussions, we always indicate the anti-crossing by the resonance point of the uncoupled states.

#### 4.2.2 Two-electron ground states: $2e$ system

In the case of two-electron systems, the Coulomb interaction is included. The Coulomb Hamiltonian for the  $2e$  system is

$$H_{(2e)}^c = \frac{1}{|\mathbf{r}_{e1} - \mathbf{r}_{e2}|}, \quad (4.4)$$

and we define

$$V_{ij,kl}^{ab} = \int \int d\mathbf{r} d\mathbf{r}' \varphi_i^a(\mathbf{r}) \varphi_j^a(\mathbf{r}) H^c \varphi_k^b(\mathbf{r}') \varphi_l^b(\mathbf{r}'). \quad (4.5)$$

Here  $\varphi_i^a(\mathbf{r})$  is the single-particle envelope wavefunction on dot  $i = B, R$  for conduction band electrons ( $a, b = e$ ) or valence band holes ( $a, b = h$ ).

There are three distributions for electrons in this system (the position of the electron is given with respect to the center of mass of the electron wavefunction here): both electrons are in the blue dot ( $2e, 0$ ), both electrons are in the red dot ( $0, 2e$ ), and each electron in each dot of the pair ( $1e, 1e$ ). Due to the Pauli exclusion principle, if the two electrons are both on the ground level, they can only form spin singlet state in the cases of ( $2e, 0$ ) and ( $0, 2e$ ), but in the case of ( $1e, 1e$ ), there are four fundamental states. If we have  $(\sigma_B, \sigma_R)$  to denote the spin configuration of ( $1e, 1e$ ), the four states are  $(\uparrow, \downarrow)$ ,  $(\downarrow, \uparrow)$ ,  $(\uparrow, \uparrow)$  and  $(\downarrow, \downarrow)$ . Considering the spin is conserved during the carrier tunneling, the states  $(\uparrow, \downarrow)$  and  $(\downarrow, \uparrow)$  are coupled to

each other though the states  $(2e, 0)$  and  $(0, 2e)$ . In the subspace expanded by  $(\uparrow, \downarrow)$  and  $(\downarrow, \uparrow)$ , we can choose different basis consisting of the states  $\frac{1}{\sqrt{2}}[(\uparrow, \downarrow) - (\downarrow, \uparrow)]$  and  $\frac{1}{\sqrt{2}}[(\uparrow, \downarrow) + (\downarrow, \uparrow)]$ . Including  $(\uparrow\downarrow, 0)$  and  $(0, \uparrow\downarrow)$ , the six states form a complete basis for the system and can be classified into two categories by the symmetry. In order to see the symmetry more clearly, we have  $e_{n\sigma}^\dagger$  to denote the operator for creating spin  $\sigma(=\uparrow, \downarrow)$  state on electron  $n(=1, 2)$ , and  $e_{ni}^\dagger$  to denote the operator for placing electron  $n(=1, 2)$  in the dot  $i(=B, R)$ , and write down the six states under consideration of Fermion's statistical properties as:

$$\begin{aligned}
 (\uparrow\downarrow, 0) &= \frac{1}{\sqrt{2}}(e_{1\uparrow}^\dagger e_{2\downarrow}^\dagger - e_{1\downarrow}^\dagger e_{2\uparrow}^\dagger) \otimes e_{1B}^\dagger e_{2B}^\dagger |0\rangle, \\
 (0, \uparrow\downarrow) &= \frac{1}{\sqrt{2}}(e_{1\uparrow}^\dagger e_{2\downarrow}^\dagger - e_{1\downarrow}^\dagger e_{2\uparrow}^\dagger) \otimes e_{1R}^\dagger e_{2R}^\dagger |0\rangle, \\
 \frac{1}{\sqrt{2}}[(\uparrow, \downarrow) - (\downarrow, \uparrow)] &= \frac{1}{\sqrt{2}}(e_{1\uparrow}^\dagger e_{2\downarrow}^\dagger - e_{1\downarrow}^\dagger e_{2\uparrow}^\dagger) \otimes \frac{1}{\sqrt{2}}(e_{1B}^\dagger e_{2R}^\dagger + e_{1R}^\dagger e_{2B}^\dagger) |0\rangle, \\
 \frac{1}{\sqrt{2}}[(\uparrow, \downarrow) + (\downarrow, \uparrow)] &= \frac{1}{\sqrt{2}}(e_{1\uparrow}^\dagger e_{2\downarrow}^\dagger + e_{1\downarrow}^\dagger e_{2\uparrow}^\dagger) \otimes \frac{1}{\sqrt{2}}(e_{1B}^\dagger e_{2R}^\dagger - e_{1R}^\dagger e_{2B}^\dagger) |0\rangle, \\
 (\uparrow, \uparrow) &= e_{1\uparrow}^\dagger e_{2\uparrow}^\dagger \otimes \frac{1}{\sqrt{2}}(e_{1B}^\dagger e_{2R}^\dagger - e_{1R}^\dagger e_{2B}^\dagger) |0\rangle, \\
 (\downarrow, \downarrow) &= e_{1\downarrow}^\dagger e_{2\downarrow}^\dagger \otimes \frac{1}{\sqrt{2}}(e_{1B}^\dagger e_{2R}^\dagger + e_{1R}^\dagger e_{2B}^\dagger) |0\rangle.
 \end{aligned} \tag{4.6}$$

From these expressions, it is obvious that the first three states consist of an anti-symmetric spin part and a symmetric spatial part, the other three states consist of a symmetric spin part and an anti-symmetric spatial part. For simplicity, we write the six states in the following way:

$$\begin{aligned}
 |1\rangle_{(2e)} &= e_{B\uparrow}^\dagger e_{B\downarrow}^\dagger |0\rangle, \\
 |2\rangle_{(2e)} &= e_{R\uparrow}^\dagger e_{R\downarrow}^\dagger |0\rangle, \\
 |3\rangle_{(2e)} &= (1/\sqrt{2})(e_{B\uparrow}^\dagger e_{R\downarrow}^\dagger - e_{B\downarrow}^\dagger e_{R\uparrow}^\dagger) |0\rangle, \\
 |4\rangle_{(2e)} &= (1/\sqrt{2})(e_{B\uparrow}^\dagger e_{R\downarrow}^\dagger + e_{B\downarrow}^\dagger e_{R\uparrow}^\dagger) |0\rangle, \\
 |5\rangle_{(2e)} &= e_{B\uparrow}^\dagger e_{R\uparrow}^\dagger |0\rangle, \\
 |6\rangle_{(2e)} &= e_{B\downarrow}^\dagger e_{R\downarrow}^\dagger |0\rangle.
 \end{aligned}$$

Here, we denote  $e_{i\sigma}^\dagger = e_{n\sigma}^\dagger \otimes e_{ni}^\dagger$ . Table 4.1 records calculated elements of Hamiltonian  $H_{(2e)}$  with the six states shown above as the basis. Clearly, the states of two symmetries are well separated into two isolated diagonal blocks of the matrix, which implies the symmetries are conserved in this  $2e$  system. The states  $|4\rangle_{(2e)}$ ,  $|5\rangle_{(2e)}$

and  $|6\rangle_{(2e)}$  are linked to the triplet states  $|T_0\rangle$ ,  $|T_+\rangle$  and  $|T_-\rangle$  respectively, which are energetically degenerate and do not get involved in  $(2e, 0) - (1e, 1e) - (0, 2e)$  coherent coupling. At certain values of  $\Delta$ ,  $\Delta_{2e(1)} (= V_{BB} - V_{BR})$  and  $\Delta_{2e(2)} (= V_{BR} - V_{RR})$ , resonance between the states  $|1\rangle_{(2e)}$  and  $|3\rangle_{(2e)}$  and resonance between the states  $|3\rangle_{(2e)}$  and  $|2\rangle_{(2e)}$  will occur, respectively, the coupling strength for both of the cases is  $2T_{2e}$ ,

$$T_{2e} = \sqrt{2}(t_e + V_{BB,BR}^{ee}) \simeq \sqrt{2}(t_e + V_{RR,RB}^{ee}), \quad (4.7)$$

which indicates the tunnel-coupling events involving two electrons. Figure 4.3 (b) is a simulation showing how the eigenstates of the  $2e$  system evolve under the gate voltage control.

$H_{(2e)}$	$ 1\rangle_{(2e)}$	$ 2\rangle_{(2e)}$	$ 3\rangle_{(2e)}$	$ 4\rangle_{(2e)}$	$ 5\rangle_{(2e)}$	$ 6\rangle_{(2e)}$
$_{(2e)}\langle 1 $	$V_{BB} - 2\Delta$	$J^{ee}$	$T_{2e}$	0	0	0
$_{(2e)}\langle 2 $	$J^{ee}$	$V_{RR}$	$T_{2e}$	0	0	0
$_{(2e)}\langle 3 $	$T_{2e}$	$T_{2e}$	$+J^{ee} + V_{BR}$ $-\Delta$	0	0	0
$_{(2e)}\langle 4 $	0	0	0	$-J^{ee} + V_{BR}$ $-\Delta$	0	0
$_{(2e)}\langle 5 $	0	0	0	0	$-J^{ee} + V_{BR}$ $-\Delta$	0
$_{(2e)}\langle 6 $	0	0	0	0	0	$-J^{ee} + V_{BR}$ $-\Delta$

**Table 4.1:** Matrix elements of the Hamiltonian  $H_{(2e)}$  with the states from  $|1\rangle_{(2e)}$  to  $|6\rangle_{(2e)}$  as the basis.  $V_{BB} = V_{BB,BB}^{ee}$ ,  $V_{RR} = V_{RR,RR}^{ee}$  and  $V_{BR} = V_{BB,RR}^{ee}$  are charge-charge direct Coulomb interactions.  $J^{ee} (= V_{BR,BR}^{ee})$  is the electron-electron Coulomb exchange interaction which couples the first two singlet states where the two electrons are in the same dot, and also contributes the S-T splitting. It blue shifts the (1e,1e) singlet state, but red shift the triplet states.

Further estimate of the magnitudes of parameters  $V_{ij,kl}^{ab}$  and  $t_e$  requires the information of the carriers' wavefunctions. For simplicity, we considered the dot in a model [58] with parabolic confinement in the lateral directions and InAs/GaAs band offsets in the vertical direction (z direction). We just show the off-diagonal elements  $J^{ee}$  and  $T_{2e}(t_e)$  since they determine the coupling. We get

$$J^{ee} = V_{BR,BR}^{ee} \approx \exp(-2\kappa_e l) V_{BB,RR}^{ee}, \quad (4.8)$$

$$t_e = 2\varepsilon_e \exp(-2\kappa_e l), \quad (4.9)$$

here  $\kappa_e$  is the inverse decay length for electron,  $l$  is the thickness of the GaAs tunneling layer from the top of the blue dot to the bottom of the red dot, and  $\varepsilon_e$  is

the single electron energy in the dot. The relation we get between  $J^{ee}$  and  $t_e$  is

$$J^{ee} \approx t_e \times \frac{V_{BB,RR}^{ee}}{2\varepsilon_e}. \quad (4.10)$$

Normally,  $V_{BB,RR}^{ee} \approx 10 \text{ meV}$  and  $2\varepsilon_e \gtrsim 1 \text{ eV}$ , so  $J^{ee} \lesssim t_e/100$ . What we would like to note from above are:

1. We made the assumption that the wavefunctions of the carriers in the dot have a very small dependence on the gate voltage (the level detuning  $\Delta$  or the vertical electric field), so that we neglected this dependence. From the measured spectrums in Fig. 4.1, each intra-dot charge plateau shows the common linear dependence of the DC-stark shift on the gate voltage. This linear dependence indicates the permanent vertical dipole in the dot, and gives evidence that the wavefunctions are essentially static with the changing voltage, or at least the center of mass of the wavefunction is stable. These are the clues of strong quantum confinements of the QDs in their growth directions.
2. With the assumption of static wavefunctions, we get constant  $t_e$  and Coulomb terms, especially the Coulomb term  $J^{ee}$ , which contributes the constant part of the singlet-triplet (S-T) splitting of the  $(1e, 1e)$  case. Although  $t_e$  is constant, its effect increases the S-T splitting in the vicinity of the resonance points such as  $V_{Gate}(\Delta_{2e(1)})$  and  $V_{Gate}(\Delta_{2e(2)})$  in Fig. 4.3 (b), and keeps decreasing with the gate running away from the resonance. Moreover,  $t_e$ 's effect has different signs on the different sides of the resonance, but  $J^{ee}$  always raises the energy of the  $(1e, 1e)$  singlet state and lowers the energy of triplet states. In Fig. 4.3 (b), between the two resonances, the triplet (green lines) are energetically higher than the singlet (blue line), there  $t_e$ 's effect dominates. In most of the case,  $J^{ee}$  is neglected in the calculations. [58, 59, 60]
3. There is another view of  $J^{ee}$ . As we see in Tab. 4.1,  $J^{ee}$  is the coupling term for states  $(2e, 0)$  and  $(0, 2e)$ , there the coupling should be the second order electron tunneling process which is expected to be very small.
4. From the experimental experience, we estimate  $V_{BB,BB}^{ee} = V_{RR,RR}^{ee} \approx 20 \text{ meV}$  and  $V_{BB,RR}^{ee} \approx 10 \text{ meV}$ , therefore, we calculate  $\Delta_{2e(1)} \approx 10 \text{ meV}$  and  $\Delta_{2e(2)} \approx -10 \text{ meV}$ .

All the signatures of the  $2e$  system can be labeled as singlet or triplet, since

the electron tunneling dominates the coupling mechanism of the system. This interaction can also be named “kinetic exchange interaction” [59]. Up to now, the singlet-triplet (S-T) basis is demonstrated as the proper representation of the  $2e$  system.

#### 4.2.3 Direct and indirect excitons: $1e1h$ system

Now we switch to the case of one electron and one hole in the CQDs. Instead of the kinetic exchange of electrons, the electron-hole exchange dominates the  $1e1h$  system. In our sample, due to the relatively long distance from the red dot layer to the Schottky contact as compared to the distance from the blue dot layer to the red dot layer, the hole has much longer resident time in the red dot compared with the blue dot. The excitons studied following are the direct exciton  $(0, 1e1h)$  with both one electron and one hole in the red dot, and the indirect exciton  $(1e, 1h)$  with one electron in the blue dot but one hole in the red dot. Tunneling of the electron between red and blue dots results in the coherent coupling of the  $1e1h$  system. Thereby we have direct and indirect electron-hole exchange interactions, respectively. We will see that the indirect one is negligible.

The general form of the electron-hole exchange interaction is proportional to the integral [23]

$$H_{e-h}^{ex} \propto \int \int d\mathbf{r}_1 d\mathbf{r}_2 \Psi_X^*(\mathbf{r}_e = \mathbf{r}_1, \mathbf{r}_h = \mathbf{r}_2) \frac{1}{|\mathbf{r}_1 - \mathbf{r}_2|} \Psi_X(\mathbf{r}_e = \mathbf{r}_2, \mathbf{r}_h = \mathbf{r}_1). \quad (4.11)$$

$\Psi_X$  is the wavefunction of the exciton,  $\mathbf{r}_1$  and  $\mathbf{r}_2$  can be either in the same dot or in different dots. In fact, this integral is proportional to the the overlap of the electron and hole wavefunctions [62]. From the view of the carriers' spins, the Hamiltonian of the electron-hole interaction of an exciton formed by a hole with spin  $J_h$  and an electron with spin  $S_e$  is given by [23]

$$H_{e-h}^{ex} = - \sum_{i=x,y,z} (a_i J_{h,i} S_{e,i} + b_i J_{h,i}^3 S_{e,i}). \quad (4.12)$$

As we discussed in Chapter 1, the spin states concerned here are  $J_h = \pm 3/2$  for heavy holes and  $S_e = \pm 1/2$  for electrons, and the angular momentum projections of the exciton states are  $M_z = \pm 1, \pm 2$ . Only the states with  $M_z = \pm 1$  are optically allowed, denoted by “bright states”, while, the states with  $M_z = \pm 2$  are denoted by “dark states”. Considering the indirect and direct exciton with different spin configurations, there are eight states to describe the  $1e1h$  system,

$$\begin{aligned}
 |1\rangle_{(1e1h)} &= e_{B\downarrow}^\dagger h_{R\uparrow}^\dagger |0\rangle, & |5\rangle_{(1e1h)} &= e_{B\uparrow}^\dagger h_{R\uparrow}^\dagger |0\rangle, \\
 |2\rangle_{(1e1h)} &= e_{R\downarrow}^\dagger h_{R\uparrow}^\dagger |0\rangle = B_+^\dagger |0\rangle, & |6\rangle_{(1e1h)} &= e_{R\uparrow}^\dagger h_{R\uparrow}^\dagger |0\rangle = D_+^\dagger |0\rangle, \\
 |3\rangle_{(1e1h)} &= e_{B\uparrow}^\dagger h_{R\downarrow}^\dagger |0\rangle, & |7\rangle_{(1e1h)} &= e_{B\downarrow}^\dagger h_{R\downarrow}^\dagger |0\rangle, \\
 |4\rangle_{(1e1h)} &= e_{R\uparrow}^\dagger h_{R\downarrow}^\dagger |0\rangle = B_-^\dagger |0\rangle, & |8\rangle_{(1e1h)} &= e_{R\downarrow}^\dagger h_{R\downarrow}^\dagger |0\rangle = D_-^\dagger |0\rangle.
 \end{aligned}$$

Here  $h_{i\sigma}^\dagger$  is the operator for generating a hole state with spin  $\sigma(=\uparrow, \downarrow)$  in the dot  $i(= B, R)$ ,  $B_\pm^\dagger |0\rangle$  and  $D_\pm^\dagger |0\rangle$  are the operators for generating bright states with  $M_z = \pm 1$  and dark states with  $M_z = \pm 2$  respectively in the red dot.

Equation (4.12) can be written in a more detailed form:

$$\begin{aligned}
 H_{e-h}^{ex} &= -\frac{1}{2} \left[ \underbrace{\frac{3}{2}(a_z + \frac{9}{4}b_z)}_{\delta_0} \sigma_z^h \sigma_z^e + \right. \\
 &\quad \left. + \underbrace{\frac{3}{4}(b_x - b_y)}_{\delta_1} (\sigma_{3+}^h \sigma_-^e + \sigma_{3-}^h \sigma_+^e) + \underbrace{\frac{3}{4}(b_x + b_y)}_{\delta_2} (\sigma_{3+}^h \sigma_+^e + \sigma_{3-}^h \sigma_-^e) \right] \quad (4.13)
 \end{aligned}$$

The spin operators used in the equation above are defined as:

$$\begin{aligned}
 \sigma_z^h |\pm 3/2\rangle_{J_h} &= \pm |\pm 3/2\rangle_{J_h}, & \sigma_z^e |\pm 1/2\rangle_{S_e} &= \pm |\pm 1/2\rangle_{S_e}, \\
 \sigma_{3+}^h | - 3/2\rangle_{J_h} &= | + 3/2\rangle_{J_h}, & \sigma_{3+}^h | + 3/2\rangle_{J_h} &= 0, \\
 \sigma_{3-}^h | + 3/2\rangle_{J_h} &= | - 3/2\rangle_{J_h}, & \sigma_{3-}^h | - 3/2\rangle_{J_h} &= 0, \\
 \sigma_+^e | - 1/2\rangle_{S_e} &= | + 1/2\rangle_{S_e}, & \sigma_+^e | + 1/2\rangle_{S_e} &= 0, \\
 \sigma_-^e | + 1/2\rangle_{S_e} &= | - 1/2\rangle_{S_e}, & \sigma_-^e | - 1/2\rangle_{S_e} &= 0.
 \end{aligned}$$

The Hamiltonian of the  $1e1h$  system, defined in Eq. (4.2), is calculated below, neglecting the constant single particle energies of one electron and one hole,

$$H_{(1e1h)} = \begin{pmatrix} H_{(1e1h)B} & 0 \\ 0 & H_{(1e1h)D} \end{pmatrix}. \quad (4.14)$$

Including indirect and direct excitons, the two diagonal blocks  $H_{(1e1h)B}$  and  $H_{(1e1h)D}$  are for bright states and dark states respectively, and their matrix elements are recorded in Tab. 4.2 and 4.3. The off-diagonal blocks in Eq. (4.14) are zero under zero in-plane external magnetic field. We show the simulation of the eigenstates evolving



under the gate voltage control for the  $1e1h$  system in Fig. 4.4 (a). Because the  $1e1h$  system is an excitonic system, and the corresponding ground state is the empty QD state, so that the optical transitions directly reflect the eigenstates information of the system. We carry out PL measurements on the red dot of CQD1, and present the data in Fig. 4.1. The area, which corresponds to the  $1e1h$  situation, is selected in Fig. 4.1 by a small dashed box, and is re-presented in Fig. 4.4 (b) for more analysis.

$H_{(1e1h)B}$	$ 1\rangle_{(1e1h)}$	$ 2\rangle_{(1e1h)}$	$ 3\rangle_{(1e1h)}$	$ 4\rangle_{(1e1h)}$
$(1e1h)\langle 1 $	$V_{BR} + \frac{1}{2}\delta_0^{BR} - \Delta$	$t_{e(1e1h)}$	$-\frac{1}{2}\delta_1^{BR}$	0
$(1e1h)\langle 2 $	$t_{e(1e1h)}$	$V_{RR} + \frac{1}{2}\delta_0^{RR}$	0	$-\frac{1}{2}\delta_1^{RR}$
$(1e1h)\langle 3 $	$-\frac{1}{2}\delta_1^{BR}$	0	$V_{BR} + \frac{1}{2}\delta_0^{BR} - \Delta$	$t_{e(1e1h)}$
$(1e1h)\langle 4 $	0	$-\frac{1}{2}\delta_1^{RR}$	$t_{e(1e1h)}$	$V_{RR} + \frac{1}{2}\delta_0^{RR}$

**Table 4.2:** Matrix elements of the diagonal block  $H_{(1e1h)B}$  of the Hamiltonian  $H_{(1e1h)}$  with the states from  $|1\rangle_{(1e1h)}$  to  $|4\rangle_{(1e1h)}$  as the basis.  $V_{BR} = -V_{BB,RR}^{eh} + d_i \frac{V}{L}$  and  $V_{RR} = -V_{RR,RR}^{eh} + d_d \frac{V}{L}$  are charge-charge direct Coulomb interactions, here  $d_i$  and  $d_d$  are permanent electric dipoles for the indirect exciton and direct exciton respectively,  $V$  is the effective voltage between the back contact and the Schottky contact of the sample defined in Fig. 4.2 (a), and  $L$  is the sample thickness.  $\delta_{0,1}^{BR}$  is the e-h exchange interaction term  $\delta_{0,1}$  defined in Eq. (4.13) for the indirect exciton, and  $\delta_{0,1}^{RR}$  is for the direct exciton in the red dot.  $t_{e(1e1h)} = t_e - V_{BR,RR}^{eh}$  is the tunneling rate for single electron in system  $1e1h$ .

$H_{(1e1h)D}$	$ 5\rangle_{(1e1h)}$	$ 6\rangle_{(1e1h)}$	$ 7\rangle_{(1e1h)}$	$ 8\rangle_{(1e1h)}$
$(1e1h)\langle 5 $	$V_{BR} - \frac{1}{2}\delta_0^{BR} - \Delta$	$t_{e(1e1h)}$	$-\frac{1}{2}\delta_2^{BR}$	0
$(1e1h)\langle 6 $	$t_{e(1e1h)}$	$V_{RR} - \frac{1}{2}\delta_0^{RR}$	0	$-\frac{1}{2}\delta_2^{RR}$
$(1e1h)\langle 7 $	$-\frac{1}{2}\delta_2^{BR}$	0	$V_{BR} - \frac{1}{2}\delta_0^{BR} - \Delta$	$t_{e(1e1h)}$
$(1e1h)\langle 8 $	0	$-\frac{1}{2}\delta_2^{RR}$	$t_{e(1e1h)}$	$V_{RR} - \frac{1}{2}\delta_0^{RR}$

**Table 4.3:** Matrix elements of the diagonal block  $H_{(1e1h)D}$  of the Hamiltonian  $H_{(1e1h)}$  with the states from  $|5\rangle_{(1e1h)}$  to  $|8\rangle_{(1e1h)}$  as the basis.  $\delta_2^{BR}$  is the e-h exchange interaction term  $\delta_2$  defined in Eq. (4.13) for the indirect exciton, and  $\delta_2^{RR}$  is for direct exciton in the red dot.

About the Hamiltonian shown in the table and the data in figures, we have some notes,

1. The eight basis states were written in a simple form. In the actual calculation, the Fermi statistics were considered in the same way as for the  $2e$  system.
2. In Fig. 4.4 (a), we neglected the indirect e-h exchange interaction terms  $\delta_{0,1,2}^{BR}$ , since the indirect overlap of the electron and hole wavefunctions are much smaller than the direct overlap. The interaction ratio of indirect to direct is about 1 : 1000. Normally,  $\delta_0^{RR}$  is in the order of  $100\mu$  eV [59, 60, 63] and  $\delta_{1,2}^{RR}$  is in the order of  $10\mu$  eV [23], and we can thereby safely neglect  $\delta_{0,1,2}^{BR}$ . In the following discussions,  $\delta_{0,1,2}$  will be used in stead of  $\delta_{0,1,2}^{RR}$ .

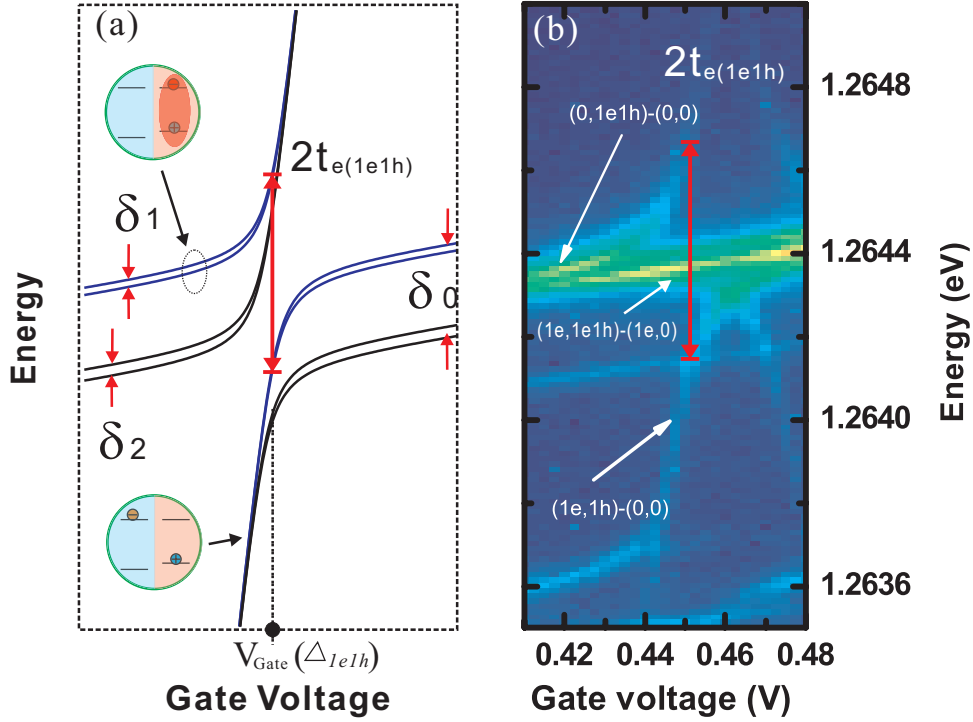


**Figure 4.4:** The energy dispersion for the  $1e1h$  system. (a) The simulated evolution of eigenvalues of Hamiltonian  $H_{1e1h}$  under gate control. The blue and black curves correspond to the bright and dark exciton transitions, respectively. The parameters are set as  $\delta_0 = 230 \mu\text{eV}$ ,  $\delta_1 = 20 \mu\text{eV}$  and  $\delta_2 = 30 \mu\text{eV}$ , the tunneling rate  $t_{e(1e1h)} = 256 \mu\text{eV}$  comes from the PL measurement in panel (b). (b) The zoom-in figure of the selected area within the small red dashed box in Fig. 4.1. The direct- and indirect- exciton transitions and the coherent coupling can be revealed from this PL measurement. The strong passing-through PL data comes from the  $3e1h$  system, which does not interact with the  $1e1h$  system. The overlap is due to the charge fluctuation in PL measurement.

3. By seen in Eq. (4.14) and Tab. 4.2 and 4.3, the exchange terms  $\delta_{0,1,2}$  determine the fine structures of excitonic states. For the direct excitons,  $\delta_0$  is the global diagonal energy detuning between bright states (states 2 and 4) and dark states (states 6 and 8).  $\delta_1$  mixes the two bright states to form two new eigenstates (blue lines in Fig. 4.4 (a)), which are optically coupled to the ground state (empty dot) by two orthogonal linear lights with the energy detuning  $\delta_1$ . And this splitting is normally referred to X-Y splitting. Similarly,  $\delta_2$  mixes the two dark states to form two new eigenstates (black lines in Fig. 4.4 (a)) with the energy detuning  $\delta_2$ , but they are still optically dark. Since we neglected the indirect e-h exchange terms, there is no fine structures for the indirect excitons.
4. Unfortunately, the resolution for PL is not sufficient to resolve the bright fine

structure, in our simulation, we set  $\delta_1 = 20 \mu\text{eV}$  according to our DT measurements on another charge-spin configuration, which will be discussed in next section. For the case of dark-exciton fine structure, we do not have the optical access to probe it, so we estimate  $\delta_0 \approx 230 \mu\text{eV}$  [60] and set  $\delta_2$  as  $30 \mu\text{eV}$  in simulation, which will not change our analysis on bright states.

5. The resonant coupling strengths of the bright and dark states are both  $2t_{e(1e1h)}$ . According to our calculation model, we have the formula,

$$t_{e(1e1h)} = t_e - V_{BR,RR}^{eh}. \quad (4.15)$$

We extract  $t_{e(1e1h)}$  as about  $257 \mu\text{eV}$  from the bright states in PL measurement shown in Fig. 4.4 (b) and apply this value in our simulation in Fig. 4.4 (a).

6. Without resolving the fine structures, we observe three branches in gate-sweep PL measurements in the  $1e1h$  resonance area. As shown in Fig. 4.4 (b), the two anti-crossing branches belong to the  $1e1h$  system in agreement with our simulation. However, the passing-through PL branch belongs to another charge-spin configurations. The non-interacting overlap between different charge configurations is due to the charge fluctuation in PL measurement. This passing-through PL branch might correspond to the transition between the excited state of  $(2e, 1e1h)$  and the ground state of  $(2e, 0)$
7. From the experimental experience, we have the estimate  $V_{RR,RR}^{eh} \approx 24 \text{ meV}$  and  $V_{BB,RR}^{eh} \approx 10 \text{ meV}$ , therefore, we estimate  $\Delta_{1e1h} = -V_{BB,RR}^{eh} + V_{RR,RR}^{eh} \approx 14 \text{ meV}$ .

We have already discussed three cases for the basic interactions in the CQDs system. Besides the linear dependence of the permanent dipole to the external electric field, Coulomb interactions are the constant parts of the energy structures, they determine the fundamental signatures of the charge configurations. The inter-dot tunneling is the main mechanism for the coherent coupling of the system, the so called kinetic exchange interaction can form singlet-triplet states precisely describing the  $2e$  system. The intra-dot electron-hole exchange interaction is the spin-spin interaction, and determines the intra-dot energy fine structures. The e-h exchange interaction is proportional to the overlap of the carriers' wavefunctions, so the inter-dot e-h exchange interaction is normally negligible.

### 4.3 Optical Transitions of the Multi-charge System

In last section, except the case of the  $1e1h$  system, the other two charge configurations correspond to the optical ground states, which are more interesting for the applications of quantum control. In QIP, both single-electrons spin and double-electron spins are proposed to be the candidates for qubits. In this section, we will experimentally study the ground-state dynamics we modeled in last section through the optical transitions with their excited states. The  $3e1h$  system, as the excitation of the  $2e$  system will be discussed first, since it is only observable feature left in PL data (Fig. 4.1). The  $2e1h$  system, as the excitation of the  $1e$  system will be discussed secondly, and it is the only coupling feature we can observe in DT measurement, implying the  $2e1h$  as the only deterministic coupling case in our CQDs structure.

#### 4.3.1 Doubly charged exciton: $3e1h$ system

In our PL data (Fig. 4.1), except the feature of the  $1e1h$  system, we have the other impressive “X” shape feature indicating the case of doubly charged exciton, the  $3e1h$  system. The detailed charge configurations involved are  $(2e,1e1h)$  and  $(1e,2e1h)$ . Considering the spin freedom, we have in total eight states to span the space of the  $3e1h$ ,

$$\begin{aligned}
 |1\rangle_{(3e1h)} &= e_{B\downarrow}^\dagger (e_{R\uparrow}^\dagger e_{R\downarrow}^\dagger) h_{R\uparrow}^\dagger |0\rangle, & |5\rangle_{(3e1h)} &= e_{B\uparrow}^\dagger (e_{R\uparrow}^\dagger e_{R\downarrow}^\dagger) h_{R\uparrow}^\dagger |0\rangle, \\
 |2\rangle_{(3e1h)} &= (e_{B\uparrow}^\dagger e_{B\downarrow}^\dagger) e_{R\downarrow}^\dagger h_{R\uparrow}^\dagger |0\rangle, & |6\rangle_{(1e1h)} &= (e_{B\uparrow}^\dagger e_{B\downarrow}^\dagger) e_{R\uparrow}^\dagger h_{R\uparrow}^\dagger |0\rangle, \\
 |3\rangle_{(3e1h)} &= e_{B\uparrow}^\dagger (e_{R\uparrow}^\dagger e_{R\downarrow}^\dagger) h_{R\downarrow}^\dagger |0\rangle, & |7\rangle_{(3e1h)} &= e_{B\downarrow}^\dagger (e_{R\uparrow}^\dagger e_{R\downarrow}^\dagger) h_{R\downarrow}^\dagger |0\rangle, \\
 |4\rangle_{(3e1h)} &= (e_{B\uparrow}^\dagger e_{B\downarrow}^\dagger) e_{R\uparrow}^\dagger h_{R\downarrow}^\dagger |0\rangle, & |8\rangle_{(3e1h)} &= (e_{B\uparrow}^\dagger e_{B\downarrow}^\dagger) e_{R\downarrow}^\dagger h_{R\downarrow}^\dagger |0\rangle.
 \end{aligned}$$

Here, the two creation operators  $e_{i\uparrow}^\dagger e_{i\downarrow}^\dagger$  ( $i = B, R$ ) are bracketed above to indicate creating an intra-dot spin-singlet state.

The interactions involved in the  $3e1h$  system are very similar to the  $1e1h$  system. Firstly, There are always two of the three electrons forming a singlet which does not contribute to the electron-hole exchange interaction, so that the remaining electron and the hole form the direct or indirect excitons and dominate the electron-hole exchange interactions in the  $3e1h$  system. Secondly, only one of the three electrons gets involved in the tunneling event due to spin-conversation and the *Pauli blockade*. For example, the coupling between states  $|3\rangle_{(3e1h)}$  and  $|4\rangle_{(3e1h)}$  can only be mediated by a spin-down electron, and there is only one spin-down electron in the system,

i.e.  $(\uparrow\downarrow, \uparrow\downarrow) \longleftrightarrow (\uparrow, \downarrow \uparrow\downarrow)$ . Therefore, the Hamiltonian of the  $3e1h$  has the same formula as the  $1e1h$ ,

$$H_{(3e1h)} = \begin{pmatrix} H_{(3e1h)B} & 0 \\ 0 & H_{(3e1h)D} \end{pmatrix}, \quad (4.16)$$

neglecting the constant single particle energies of three electrons and one hole. Including direct and indirect doubled charged excitons, the two diagonal blocks  $H_{(3e1h)B}$  and  $H_{(3e1h)D}$  are for bright excitons and dark excitons respectively, and their matrix elements are recorded in Tab. 4.4 and 4.5.

$H_{(3e1h)B}$	$ 1\rangle_{(3e1h)}$	$ 2\rangle_{(3e1h)}$	$ 3\rangle_{(3e1h)}$	$ 4\rangle_{(3e1h)}$
$(3e1h)\langle 1 $	$V_{BRRR} + \frac{1}{2}\delta_0^{BR} - \Delta$	$t_{e(3e1h)}$	$-\frac{1}{2}\delta_1^{BR}$	0
$(3e1h)\langle 2 $	$t_{e(3e1h)}$	$V_{BRRR} + \frac{1}{2}\delta_0^{RR} - 2\Delta$	0	$-\frac{1}{2}\delta_1^{RR}$
$(3e1h)\langle 3 $	$-\frac{1}{2}\delta_1^{BR}$	0	$V_{BRRR} + \frac{1}{2}\delta_0^{BR} - \Delta$	$t_{e(3e1h)}$
$(4e1h)\langle 4 $	0	$-\frac{1}{2}\delta_1^{RR}$	$t_{e(3e1h)}$	$V_{BRRR} + \frac{1}{2}\delta_0^{RR} - 2\Delta$

**Table 4.4:** Matrix elements of the diagonal block  $H_{(3e1h)B}$  of the Hamiltonian  $H_{(3e1h)}$  with the states from  $|1\rangle_{(3e1h)}$  to  $|4\rangle_{(3e1h)}$  as the basis.  $V_{BRRR} = -V_{BB,RR}^{eh} - 2V_{RR,RR}^{eh} + 2V_{BB,RR}^{ee} + V_{RR,RR}^{ee} + d_i \frac{V}{L}$  and  $V_{BBRR} = -2V_{BB,RR}^{eh} - V_{RR,RR}^{eh} + 2V_{BB,RR}^{ee} + V_{BB,BB}^{ee} + d_d \frac{V}{L}$  are charge-charge direct Coulomb interactions, here  $d_i$  and  $d_d$  are permanent electric dipoles for the indirect exciton and direct exciton respectively,  $V$  is the effective voltage between the back contact and the Schottky contact of the sample defined in Fig. 4.2 (a), and  $L$  is the sample thickness.  $\delta_{0,1}^{BR}$  is the e-h exchange interaction term  $\delta_{0,1}$  defined in Eq. (4.13) for the indirect exciton, and  $\delta_{0,1}^{RR}$  is for the direct exciton in the red dot.  $t_{e(3e1h)} = t_e + V_{BR,RR}^{ee} + V_{BR,BB}^{ee} - V_{BR,RR}^{eh}$  is the tunneling rate for single electron in the  $3e1h$  system.

$H_{(3e1h)D}$	$ 5\rangle_{(3e1h)}$	$ 6\rangle_{(3e1h)}$	$ 7\rangle_{(3e1h)}$	$ 8\rangle_{(3e1h)}$
$(3e1h)\langle 5 $	$V_{BRRR} - \frac{1}{2}\delta_0^{BR} - \Delta$	$t_{e(3e1h)}$	$-\frac{1}{2}\delta_2^{BR}$	0
$(3e1h)\langle 6 $	$t_{e(3e1h)}$	$V_{BRRR} - \frac{1}{2}\delta_0^{RR} - 2\Delta$	0	$-\frac{1}{2}\delta_2^{RR}$
$(3e1h)\langle 7 $	$-\frac{1}{2}\delta_2^{BR}$	0	$V_{BRRR} - \frac{1}{2}\delta_0^{BR} - \Delta$	$t_{e(3e1h)}$
$(3e1h)\langle 8 $	0	$-\frac{1}{2}\delta_2^{RR}$	$t_{e(3e1h)}$	$V_{BRRR} - \frac{1}{2}\delta_0^{RR} - 2\Delta$

**Table 4.5:** Matrix elements of the diagonal block  $H_{(3e1h)D}$  of the Hamiltonian  $H_{(3e1h)}$  with the states from  $|5\rangle_{(3e1h)}$  to  $|8\rangle_{(3e1h)}$  as the basis.  $\delta_2^{BR}$  is the e-h exchange interaction term  $\delta_2$  defined in Eq. (4.13) for the indirect exciton, and  $\delta_2^{RR}$  is for direct exciton in the red dot.

We calculate eigenvalues of the Hamiltonian  $H_{(3e1h)}$  for a range of gate voltage

to show the evolution of the eigenstates under gate control, and present this calculation in the upper part of Fig. 4.5 (a). Neglecting  $\delta_{1,2}^{BR}$ , we have the fine structures on states (2e,1e1h). The location of the anti-crossing for the  $3e1h$  system is the resonance point of the uncoupled doubly charged direct excitons and indirect excitons,  $\Delta_{3e1h} = V_{BBRR} - V_{BRRR}$ . With the estimate,  $V_{BB,RR}^{eh} \approx V_{BB,RR}^{ee} \approx 10$  meV,  $V_{RR,RR}^{ee} \approx V_{BB,BB}^{ee} \approx 20$  meV and  $V_{RR,RR}^{eh} \approx 24$  meV, we calculate  $\Delta_{3e1h} \approx 14$  mV. As we mentioned at the beginning of this section, we are interested in the optical transitions. Here, the ground states of the  $3e1h$  system are the two-electron states. We include the  $2e$  states in Fig. 4.5 (a) so that we can clearly map the transitions. We notice that the anti-crossings for the  $2e$  system occurs at  $\Delta_{2e(1)} = 10$  mV and  $\Delta_{2e(2)} = -10$  meV, according to Eq. 4.1, we have

$$V_{Gate}(\Delta_{3e1h}) < V_{Gate}(\Delta_{2e(1)}) < V_{Gate}(\Delta_{2e(2)}). \quad (4.17)$$

As a result, in Fig 4.5 (a) we have the displacement of the anti-crossings along the gate-voltage dimension.

In Fig 4.5 (a), without resolving the fine structures and lifting the spin degeneracy, we have six groups of optical transitions between the excited states and ground states labeled from ① to ⑥. The corresponding transition energies are calculated and shown in Fig 4.5 (b), which do match our observations for the PL measurement shown in Fig 4.5 (c), which is the zoom-in figure of the area selected by the big red dashed box in Fig 4.1. About these optical transitions, we have some notes:

1. The displacement of the eigenstate anti-crossings in the  $3e1h$  and  $2e$  configurations results in the “X” shape optical transitions. The coupling strengths for both cases can be extracted. Both of the two anti-crossings at lower gate voltage come from the excited states ( $3e1h$ ), and the corresponding tunnel coupling strength is  $2t_{e(3e1h)}$ . From our calculation model, we have the formula,

$$\begin{aligned} t_{e(3e1h)} &= t_e + V_{BR,RR}^{ee} + V_{BR,BB}^{ee} - V_{BR,RR}^{eh} \\ &\approx t_e + 2V_{BR,BB}^{ee} - V_{BR,RR}^{eh}. \end{aligned} \quad (4.18)$$

Both of the two anti-crossings at higher gate voltage come from the ground states ( $2e$ ), and the corresponding tunnel coupling strength is  $2T_e$ . From our PL measurement, we extract  $t_{e(3e1h)} \approx 295$   $\mu$ eV and  $T_e \approx 476$   $\mu$ eV, respectively. Together with  $t_{e(1e1h)} \approx 257$   $\mu$ eV extracted from PL measurement in last section and the equations (4.7), (4.15) and (4.18), we can also extract

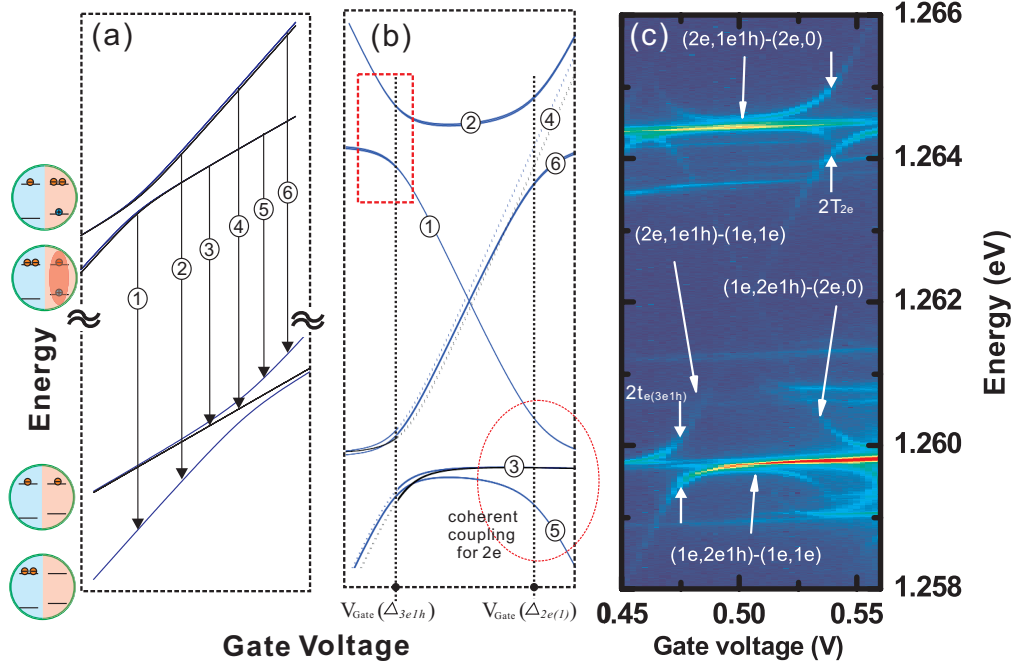


**Figure 4.5:** The energy dispersion for the  $3e1h$  system. (a) The simulated evolutions of eigenvalues of both the excited state Hamiltonian  $H_{3e1h}$  and the ground state Hamiltonian  $H_{2e}$  under gate control. For the excited states, the blue and black curves correspond to doubly charged bright and dark excitons, respectively. For the ground states, the blue and black curves correspond to singlet states and triplet states, respectively. (b) The calculated energies for the six group of transitions labeled in panel (a), blue and black curves correspond to the transitions from bright and dark excited states, respectively. The dashed curves indicates the weak and undetected signal. The red dashed circle indicates the data area where the coherent coupling of the  $2e$  ground states can be fully revealed. The red dashed box indicates a data area for later discussions. The parameters used are  $\delta_0 = 230 \mu\text{eV}$ ,  $\delta_1 = 20 \mu\text{eV}$  and  $\delta_2 = 30 \mu\text{eV}$ , the tunneling rate  $t_{e(3e1h)} = 295 \mu\text{eV}$  and  $T_e = 476 \mu\text{eV}$  are extracted from the PL measurement in panel (c). (c) The zoom-in figure of the selected area within the big red dashed box in Fig. 4.1.

the pure single-electron tunneling rate  $t_e \approx 317 \mu\text{eV}$  and the Coulomb terms  $V_{BR,RR}^{ee} \approx V_{BR,BB}^{ee} \approx 19 \mu\text{eV}$  and  $V_{BR,RR}^{eh} \approx 60 \mu\text{eV}$ .

2. The direct and indirect excitons defined for the  $3e1h$  system here are with respect to the unpaired electron and the red-dot hole for the simplicity of the modeling, however the actual transitions can involve the hole and one electron from the two-electron pair, and the definitions of bright and dark states are relative as well. For example, according to our nomenclature, state  $|5\rangle_{(3e1h)} = (\uparrow, 2e \uparrow)$  is a doubly charged indirect dark exciton, but it can optically decay to the state  $(\uparrow, \uparrow)$  through intra-dot recombination involving the spin-down hole

and the spin-up electron from the intra-dot singlet.

3. Keeping our nomenclature about the excitons for the  $3e1h$  system, all the dark states optically decay to the electron spin triplet states,

$$|5\rangle_{(3e1h)} = (\uparrow, \uparrow \underline{\downarrow\uparrow}) \longrightarrow (\uparrow, \uparrow) = |T_+\rangle, \quad (4.19)$$

$$|6\rangle_{(3e1h)} = (\uparrow \underline{\downarrow}, \uparrow \underline{\uparrow}) \longrightarrow (\uparrow, \uparrow) = |T_+\rangle, \quad (4.20)$$

$$|7\rangle_{(3e1h)} = (\downarrow, \downarrow \underline{\uparrow\downarrow}) \longrightarrow (\downarrow, \downarrow) = |T_-\rangle, \quad (4.21)$$

$$|8\rangle_{(3e1h)} = (\downarrow \underline{\uparrow}, \downarrow \underline{\downarrow}) \longrightarrow (\downarrow, \downarrow) = |T_-\rangle, \quad (4.22)$$

here, the underlined spins are involved in the transitions. As a result, the optical decays ①, ②, ⑤ and ⑥ in Fig. 4.5 (a) and (b) do not involve doubly charged dark excitons, because the ground states are the electron spin singlet states.

4. As shown in Fig. 4.5 (a), optical decays ③ and ④ are expected to end up with the electron spin triplet states. Investigating our PL data in Fig. 4.5 (c), for the gate-voltage values larger than  $V_{Gate}(\Delta_{3e1h})$ , transition ③ is clearly observed but transition ④ is extremely weak or undetected.

For the case of transition ④, after the  $3e1h$  resonance, the excited states are dominated by the state components with the charge configuration of  $(2e, 1e1h)$ , which include the doubly charged direct bright excitons  $|2\rangle_{(3e1h)}$  and  $|4\rangle_{(3e1h)}$  and the doubly charged direct dark excitons  $|6\rangle_{(3e1h)}$  and  $|8\rangle_{(3e1h)}$ . The intra-dot transitions are only possible for the bright states,

$$|2\rangle_{(3e1h)} = (\uparrow\downarrow, \underline{\downarrow\uparrow}) \longrightarrow (\uparrow\downarrow, 0) = |S_{2,0}\rangle, \quad (4.23)$$

$$|4\rangle_{(3e1h)} = (\uparrow\downarrow, \underline{\uparrow\downarrow}) \longrightarrow (\uparrow\downarrow, 0) = |S_{2,0}\rangle. \quad (4.24)$$

The singlet ground states are in conflict with the triplet requirement, as a result, the intra-dot transitions are strongly suppressed. This situation could be perfect for studying the inter-dot transitions, as a matter of fact, the undetected result convinces the inter-dot transitions are negligible.

Whereas, when transition ④ is strongly suppressed, the excited states of transition ③ are dominated by the state components with the charge configuration of  $(1e, 2e1h)$ , which are the doubly charged indirect excitons  $|1\rangle_{(3e1h)}$ ,  $|3\rangle_{(3e1h)}$ ,



$|5\rangle_{(3e1h)}$  and  $|7\rangle_{(3e1h)}$ . The intra-dot transitions,

$$|1\rangle_{(3e1h)} = (\downarrow, \uparrow \underline{\downarrow\uparrow}) \longrightarrow (\downarrow, \uparrow) = \frac{1}{\sqrt{2}}(|T_0\rangle - |S_{1,1}\rangle), \quad (4.25)$$

$$|3\rangle_{(3e1h)} = (\uparrow, \downarrow \underline{\uparrow\downarrow}) \longrightarrow (\uparrow, \downarrow) = \frac{1}{\sqrt{2}}(|T_0\rangle + |S_{1,1}\rangle) \quad (4.26)$$

have 50% probability to fulfill the transitions ③ and 50% probability to be suppressed. The transitions shown in Eq. (4.19) and (4.21) fully meet the requirements of transition ③. Therefore, we can observe the strong PL signal for transition ③, which link to the electron triplet states in CQDs system. In Fig. 4.5 (b), a red dashed circle indicate an area where the optical transitions ①, ③ and ⑤ can fully reveal the coherent coupling of the  $2e$  ground states.

From our calculation model, the  $3e1h$  resonance point is where the two groups of transitions ③ and ④ swap their excited states. In the case of the gate voltage being smaller than  $V_{Gate}(\Delta_{3e1h})$ , transition ④ will become stronger, while transition ③ will fade away with the gate voltage decreased.

5. In Fig. 4.5 (c), the passing-through signal between transitions ① and ②, ② and ⑥, ⑤ and ⑥ might come from the  $1e1h$  charge configuration. The overlap between different charge configurations is due to the charge fluctuations in PL measurements.

Up to now, we have already explained the main features of the PL data shown in Fig. 4.1 for CQD1. Especially, we revealed the  $2e$  ground state coupling through optical transitions from the  $3e1h$  system. We also carry out PL measurements on other CQDs from the same wafer and realize that the PL we discussed above is very typical for this wafer. They always show the coupling features for the  $1e1h$  and  $3e1h$  transitions. The drawbacks of PL measurements are the low spectral resolution and charge fluctuation. For unambiguous study of the CQDs system, we move on to DT measurement.

### 4.3.2 Singly charged exciton: $2e1h$ system

Our original idea for doing DT measurement is to reveal the fine structures which can not be resolved in PL measurements and then to investigate further applications. However the only tunnel-coupling event we observed from DT is for the  $2e1h$  charge configuration, which is not observed in PL measurement with our samples of 13

nm spacing layer, but it has been observed with the sample of 15 nm spacing layer [60, 64].

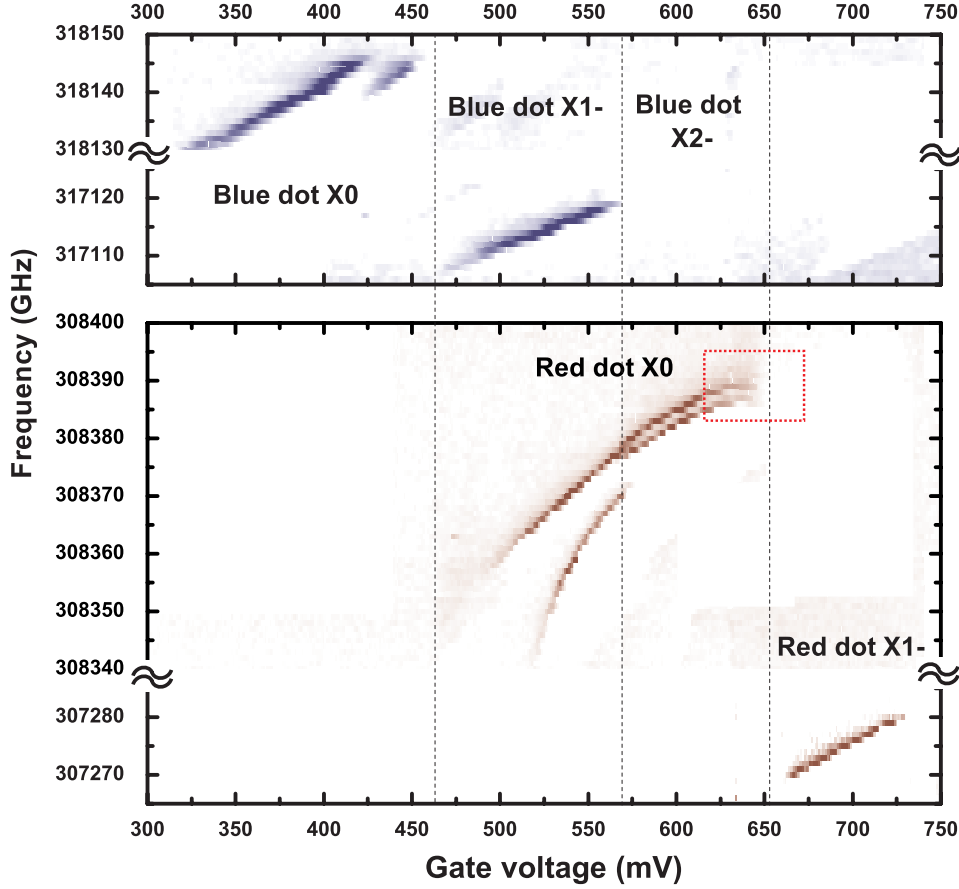


**Figure 4.6:** Two dimensional DT scan for both the blue dot and red dot of CQD2 under zero magnetic field. The vertical dashes lines mark the gate-voltage range for different charge configurations in CQD2. The red dashed box select a data area for later discussions in the text.

Figure 4.6 is the full map of two dimensional DT measurement on both blue and red dots of CQD2, which has the similar PL data as CQD1. Here, we have the unambiguous and static ground-state charge configurations for CQDs system. We notice that there is no overlap between the case of blue dot being singly charged and the case of red bot being singly charged, hence there is no single-electron tunnel coupling for the  $1e$  system in CQD2. As a result, within the gate-voltage range 460 mV~570 mV, the anti-crossing observed must come from the electron tunnel coupling in excited states which have the  $2e1h$  charge configuration.

Although both carrying two electrons, the tunnel coupling for the  $2e1h$  system

is different from the  $2e$  system. Both the kinetic exchange interaction and the e-h exchange interaction determine the coupling behavior in the case of the  $2e1h$ . Let's recall the analysis of symmetry for the  $2e$  system, there the triplet states were well separated from the singlet states, as shown in Tab. 4.1. From the view of singlet-triplet basis, when an extra hole is added in the red dot (for example a hole with spin  $\uparrow$ ), we get the off-diagonal element of the matrix for the Hamiltonian  ${}_{(2e)}\langle 3|h_{R\uparrow}(H_{(2e1h)})h_{R\uparrow}^\dagger|4\rangle_{(2e)} = -\frac{1}{2}\delta_0$ , which is not zero any more, so  $(1e, 1e1h)$  singlet is mixed with  $(1e, 1e1h)$  triplet state  $T_0$ , the symmetry is broken. Even more, considering the different hole spin states, there will be more off-diagonal elements with  $\delta_1$  and  $\delta_2$  to mix singlets and triplets even further. Therefore the singlet-triplet basis can not properly describe the  $2e1h$  system. The twelve more fundamental states are used here as the basis.

$$\begin{aligned}
 |1\rangle_{(2e1h)} &= e_{B\uparrow}^\dagger e_{B\downarrow}^\dagger h_{R\uparrow}^\dagger |0\rangle, & |7\rangle_{(2e1h)} &= e_{B\uparrow}^\dagger e_{B\downarrow}^\dagger h_{R\downarrow}^\dagger |0\rangle, \\
 |2\rangle_{(2e1h)} &= e_{R\uparrow}^\dagger e_{R\downarrow}^\dagger h_{R\uparrow}^\dagger |0\rangle, & |8\rangle_{(2e1h)} &= e_{R\uparrow}^\dagger e_{R\downarrow}^\dagger h_{R\downarrow}^\dagger |0\rangle, \\
 |3\rangle_{(2e1h)} &= e_{B\uparrow}^\dagger e_{R\downarrow}^\dagger h_{R\uparrow}^\dagger |0\rangle, & |9\rangle_{(2e1h)} &= e_{B\uparrow}^\dagger e_{R\downarrow}^\dagger h_{R\downarrow}^\dagger |0\rangle, \\
 |4\rangle_{(2e1h)} &= e_{B\downarrow}^\dagger e_{R\uparrow}^\dagger h_{R\uparrow}^\dagger |0\rangle, & |10\rangle_{(2e1h)} &= e_{B\downarrow}^\dagger e_{R\uparrow}^\dagger h_{R\downarrow}^\dagger |0\rangle, \\
 |5\rangle_{(2e1h)} &= e_{B\uparrow}^\dagger e_{R\uparrow}^\dagger h_{R\uparrow}^\dagger |0\rangle, & |11\rangle_{(2e1h)} &= e_{B\uparrow}^\dagger e_{R\uparrow}^\dagger h_{R\downarrow}^\dagger |0\rangle, \\
 |6\rangle_{(2e1h)} &= e_{B\downarrow}^\dagger e_{R\downarrow}^\dagger h_{R\uparrow}^\dagger |0\rangle, & |12\rangle_{(2e1h)} &= e_{B\downarrow}^\dagger e_{R\downarrow}^\dagger h_{R\downarrow}^\dagger |0\rangle.
 \end{aligned}$$

The Hamiltonian of the  $2e1h$  system, defined in Eq. (4.2), is calculated below, neglecting the constant single particle energies of two electron and one hole,

$$H_{(2e1h)} = \begin{pmatrix} H_{(2e1h)\uparrow} & H_{(2e1h)\uparrow\leftrightarrow\downarrow} \\ H_{(2e1h)\uparrow\leftrightarrow\downarrow}^* & H_{(2e1h)\downarrow} \end{pmatrix}. \quad (4.27)$$

The diagonal blocks  $H_{(2e1h)\uparrow}$  and  $H_{(2e1h)\downarrow}$  and off-diagonal block  $H_{(2e1h)\uparrow\leftrightarrow\downarrow}$  are recorded in Tab. 4.6, 4.7 and 4.8, respectively.

Following the same route as our previous discussions for other charge configurations, we calculate eigenvalues of the Hamiltonian  $H_{(2e1h)}$  for a range of gate voltage. Together with the  $(1e,0)$  ground states, we show the evolution of eigenstates for both the excited states and the ground states under gate control in Fig. 4.7 (a). According to the static charge configurations revealed by DT measurement, the transitions between the  $2e1h$  and  $1e$  are only available within a gate-voltage range close to  $V_{Gate}(\Delta_{2e1h(1)})$  but far from  $V_{Gate}(\Delta_{2e1h(2)})$  as indicated by a light-yellow window in

$H_{(2e1h)\uparrow}$	$ 1\rangle_{(2e1h)}$	$ 2\rangle_{(2e1h)}$	$ 3\rangle_{(2e1h)}$	$ 4\rangle_{(2e1h)}$	$ 5\rangle_{(2e1h)}$	$ 6\rangle_{(2e1h)}$
$(2e1h)\langle 1 $	$V_{BBR} - 2\Delta$	$J^{ee}$	$t_{e(2e1h)}$	$-t_{e(2e1h)}$	0	0
$(2e1h)\langle 2 $	$J^{ee}$	$V_{RRR}$	$t_{e(2e1h)}$	$-t_{e(2e1h)}$	0	0
$(2e1h)\langle 3 $	$t_{e(2e1h)}$	$t_{e(2e1h)}$	$V_{BRR} + \frac{1}{2}\delta_0$ $-\Delta$	$-J^{ee}$	0	0
$(2e1h)\langle 4 $	$-t_{e(2e1h)}$	$-t_{e(2e1h)}$	$-J^{ee}$	$V_{BRR} - \frac{1}{2}\delta_0$ $-\Delta$	0	0
$(2e1h)\langle 5 $	0	0	0	0	$V_{BRR} - \frac{1}{2}\delta_0$ $-J^{ee} - \Delta$	0
$(2e1h)\langle 6 $	0	0	0	0	0	$V_{BRR} + \frac{1}{2}\delta_0$ $-J^{ee} - \Delta$

**Table 4.6:** Matrix elements of the diagonal block  $H_{(2e1h)\uparrow}$  of the Hamiltonian  $H_{(2e1h)}$  with the states from  $|1\rangle_{(2e1h)}$  to  $|6\rangle_{(2e1h)}$  as the basis.  $V_{BBR} = V_{BB,BB}^{ee} - 2V_{BB,RR}^{eh} + 2d_i\frac{V}{L}$ ,  $V_{RRR} = V_{RR,RR}^{ee} - 2V_{RR,RR}^{eh} + 2d_d\frac{V}{L}$  and  $V_{BRR} = V_{BB,RR}^{ee} - V_{BB,RR}^{eh} - V_{RR,RR}^{eh} + d_i\frac{V}{L} + d_d\frac{V}{L}$  are charge-charge direct Coulomb interactions, here  $d_i$ ,  $d_d$ ,  $V$  and  $L$  have the same definitions as in Tab. 4.2.  $t_{e(2e1h)} = t_e + V_{BB,BR}^{ee} - V_{BR,RR}^{eh} \approx t_e + V_{RR,BR}^{ee} - V_{BR,RR}^{eh}$  is the tunneling rate for single electron in the  $2e1h$  system.

$H_{(2e1h)\downarrow}$	$ 7\rangle_{(2e1h)}$	$ 8\rangle_{(2e1h)}$	$ 9\rangle_{(2e1h)}$	$ 10\rangle_{(2e1h)}$	$ 11\rangle_{(2e1h)}$	$ 12\rangle_{(2e1h)}$
$(2e1h)\langle 7 $	$V_{BBR} - 2\Delta$	$J^{ee}$	$t_{e(2e1h)}$	$-t_{e(2e1h)}$	0	0
$(2e1h)\langle 8 $	$J^{ee}$	$V_{RRR}$	$t_{e(2e1h)}$	$-t_{e(2e1h)}$	0	0
$(2e1h)\langle 9 $	$t_{e(2e1h)}$	$t_{e(2e1h)}$	$V_{BRR} - \frac{1}{2}\delta_0$ $-\Delta$	$-J^{ee}$	0	0
$(2e1h)\langle 10 $	$-t_{e(2e1h)}$	$-t_{e(2e1h)}$	$-J^{ee}$	$V_{BRR} + \frac{1}{2}\delta_0$ $-\Delta$	0	0
$(2e1h)\langle 11 $	0	0	0	0	$V_{BRR} + \frac{1}{2}\delta_0$ $-J^{ee} - \Delta$	0
$(2e1h)\langle 12 $	0	0	0	0	0	$V_{BRR} - \frac{1}{2}\delta_0$ $-J^{ee} - \Delta$

**Table 4.7:** Matrix elements of the diagonal block  $H_{(2e1h)\downarrow}$  of the Hamiltonian  $H_{(2e1h)}$  with the states from  $|7\rangle_{(2e1h)}$  to  $|12\rangle_{(2e1h)}$  as the basis.

Fig. 4.7 (a). The calculated transitions are presented in Fig. 4.7 (b). The corresponding DT observation is shown in Fig. 4.7 (c), which only reveal the coupling structures matching the transitions within the select area in Fig. 4.7 (b) by a red dashed box. About these transitions, we have some notes,

1. The  $2e1h$  system is more complicated than the others discussed previously, due to the interplay between kinetic exchange interaction and e-h exchange interaction, each eigenstate of the Hamiltonian  $H_{(2e1h)}$  is the admixture of the twelve states we defined above. From the view of direct excitons, states  $|2\rangle_{(2e1h)}$ ,  $|3\rangle_{(2e1h)}$ ,  $|6\rangle_{(2e1h)}$ ,  $|8\rangle_{(2e1h)}$ ,  $|10\rangle_{(2e1h)}$  and  $|11\rangle_{(2e1h)}$  are linked to the bright transitions, while states  $|4\rangle_{(2e1h)}$ ,  $|5\rangle_{(2e1h)}$ ,  $|9\rangle_{(2e1h)}$  and  $|12\rangle_{(2e1h)}$  are linked to the dark transitions. Due to the electron tunnel coupling, dark state

$H_{(2e1h)\uparrow\leftrightarrow\downarrow}$	$ 7\rangle_{(2e1h)}$	$ 8\rangle_{(2e1h)}$	$ 9\rangle_{(2e1h)}$	$ 10\rangle_{(2e1h)}$	$ 11\rangle_{(2e1h)}$	$ 12\rangle_{(2e1h)}$
$(2e1h)\langle 1 $	0	0	0	0	0	0
$(2e1h)\langle 2 $	0	0	0	0	0	0
$(2e1h)\langle 3 $	0	0	0	0	$-\frac{1}{2}\delta_1$	0
$(2e1h)\langle 4 $	0	0	0	0	0	$-\frac{1}{2}\delta_2$
$(2e1h)\langle 5 $	0	0	$-\frac{1}{2}\delta_2$	0	0	0
$(2e1h)\langle 6 $	0	0	0	$-\frac{1}{2}\delta_1$	0	0

**Table 4.8:** Matrix elements of the off-diagonal block  $H_{(2e1h)\uparrow\leftrightarrow\downarrow}$  of the Hamiltonian  $H_{(2e1h)}$ .

$|4\rangle_{(2e1h)}$  ( $|9\rangle_{(2e1h)}$ ) is mixed with bright states  $|2\rangle_{(2e1h)}$  and  $|3\rangle_{(2e1h)}$  ( $|8\rangle_{(2e1h)}$  and  $|10\rangle_{(2e1h)}$ ). Since the gate-voltage range we have the  $2e1h$  system in DT measurements is far from the  $V_{Gate}(\Delta_{2e1h(2)})$ , the coupling between  $|4\rangle_{(2e1h)}$  and  $|2\rangle_{(2e1h)}$  ( $|9\rangle_{(2e1h)}$  and  $|8\rangle_{(2e1h)}$ ) is negligible. Although the coupling term  $J_{ee}$  between  $|4\rangle_{(2e1h)}$  and  $|3\rangle_{(2e1h)}$  ( $|9\rangle_{(2e1h)}$  and  $|10\rangle_{(2e1h)}$ ) is very small, it is still finite, and results in the bright-dark hybridisation<sup>1</sup>. The brightening of dark state  $|5\rangle_{(2e1h)}$  ( $|12\rangle_{(2e1h)}$ ) is realized by coupling to state  $|9\rangle_{(2e1h)}$  ( $|4\rangle_{(2e1h)}$ ) via e-h exchange interaction  $\delta_2$ . Some signatures of brightened dark states were observed in the work by Falt *et. al.* [60]. We didn't observe any brightened dark transitions in DT, so the simulated dark transitions are indicated by dashed curves in Fig. 4.7 (b).

2. In order to extract the fine-structure coupling strength  $\delta_1$  from the combined interaction, we need to switch off the kinetic exchange interaction. It can be done by change the charge state of the ground states to disable the transitions forming the  $2e1h$  states. In Fig. 4.7 (c), when the gate voltage is switched from the gate-voltage range for (1e,0) to the range for (2e,0), the behavior of the two transitions are switched from the anti-crossing to the X-Y splitting. There,  $\delta_1$  is extracted to be about 5 GHz ( $\approx 20 \mu\text{eV}$ ). Although the value is for CQD2, from our experience on this wafer, this number is very typical, and could be used as a good estimate for other CQDs. The other coupling strengths  $\delta_{0,2}$  are not revealed in our measurements.
3. The tunneling rate defined for the  $2e1h$  system is calculated from the Hamiltonian  $H_{(2e1h)}$ ,

$$t_{e(2e1h)} = t_e + V_{BB,BR}^{ee} - V_{BR,RR}^{eh} \approx t_e + V_{RR,BR}^{ee} - V_{BR,RR}^{eh}. \quad (4.28)$$

<sup>1</sup>We notice that, the coupling between  $|4\rangle_{(2e1h)}$  and  $|3\rangle_{(2e1h)}$  is equivalent to  $|4\rangle_{(2e1h)} \leftrightarrow |1\rangle_{(2e1h)} \leftrightarrow |3\rangle_{(2e1h)}$  via second order electron tunneling.

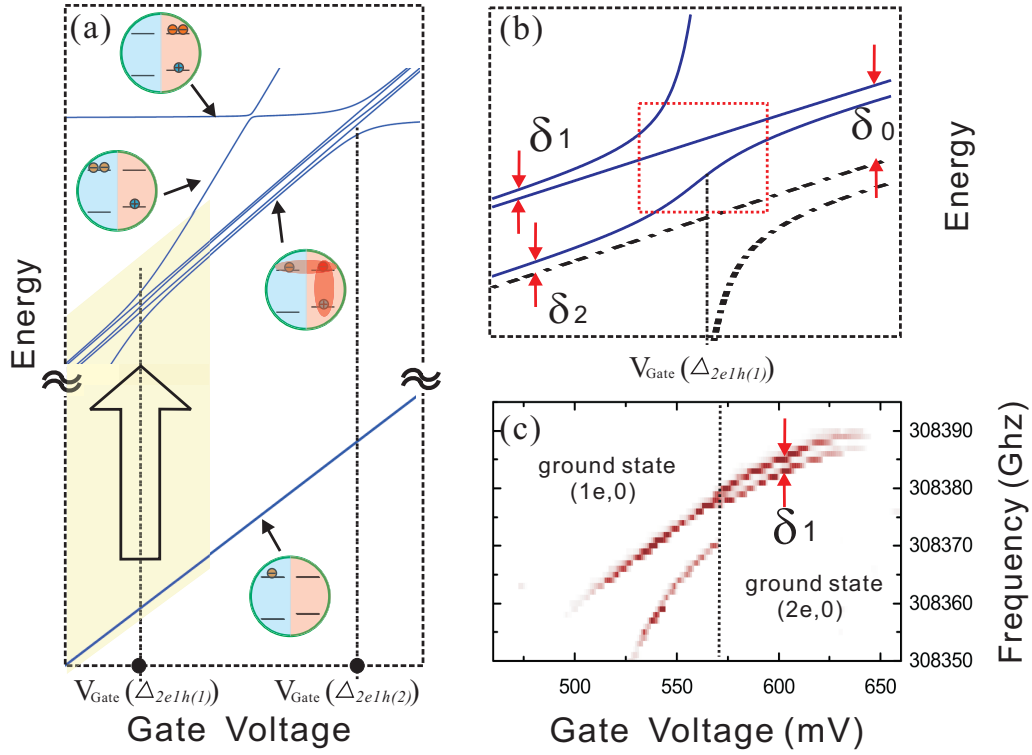


**Figure 4.7:** The energy dispersion for the  $2e1h$  system. (a) The simulated evolutions of eigenvalues of the excited state Hamiltonian  $H_{2e1h}$  and the ground state  $(1e,0)$  under gate control. The light-yellow window indicates the transitions involved in DT measurement. (b) The calculated energies for the of transitions, blue curves correspond to the transitions of the bright states. The dashed black curves indicates the transitions of the dark states. The red dashed box indicates the area matching the observation of DT. (c) The DT measurements on the neutral red dot of CQD2 with the blue dot singly and doubly charged as the ground states.

We notice that, due to the intra-dot e-h exchange interaction, the anti-crossing we observed only involves single-electron tunneling events. Because of the resident hole with a certain spin state in the red dot, tunnelings for different electron spins need to cost different energies. If one of two electron spins is energetically favorable, the other one will be not.

4. The resonance points for the  $2e1h$  system are calculated as,  $\Delta_{2e1h(1)} = V_{BRR} - V_{BRR} \approx 24$  meV and  $\Delta_{2e1h(2)} = V_{BRR} - V_{RRR} \approx 4$  meV, with the typical estimate on Coulomb terms,  $V_{BBRR}^{eh} \approx 10$  meV,  $V_{RRRR}^{eh} \approx 24$  meV,  $V_{BBRR}^{ee} \approx 10$  meV and  $V_{BBBB}^{ee} \approx 20$  meV.
5. Besides the  $2e1h$  transitions, we also observe some small features for the  $3e1h$  transitions from DT data in Fig. 4.6. In Fig. 4.8, we compare the two selected areas from Fig. 4.5 (b) and Fig. 4.6, and confirm the transitions observed

corresponding to the transition ①. At the gate voltage 630 mV, we start to see the nonlinear slope which implies the start of the anti-crossing. Unfortunately, the  $(2e, 0)$  charge configuration switches to  $(2e, 1e)$  after 640 mV, otherwise, we would have chance to reveal the resonance of the  $3e1h$  system.

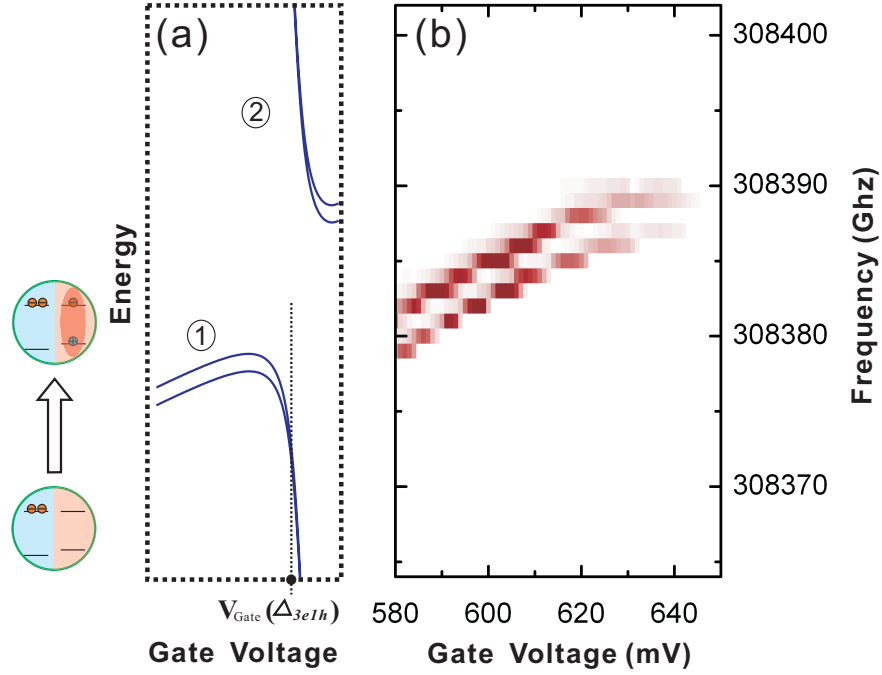


**Figure 4.8:** The DT data for the  $3e1h$  system. (a) The select area from Fig. 4.5 (b), (b) The select area from Fig. 4.6.

It is not too surprising that DT reveals totally different charge and spin configurations from PL measurements. In PL measurements, we excite the system using above-band excitation, a large number of electrons and holes are created in the host material. Consequently, they effectively build an internal electric field which lower down the level arm of the band structure, so that all the charge states can happen at smaller gate voltage compared with the cases in DT measurement. This effect is not stable, therefore, different charge states can have overlaps. That results in the much richer spectrum observed in PL. But as we mentioned at the beginning of this section, DT provides the information of static states, which are more important for the deterministic control of the quantum system.

## 4.4 The gate-voltage map for charge and spin configurations in CQDs

As the last section of this chapter, we summarize charge and spin configurations which are relevant to our CQDs system and mark them on the axis of gate voltage. So that we can have a full picture about where and how the coherent coupling happens.

In last two sections, we estimated the values of  $\Delta$  for all the resonance points. They are:  $\Delta_e \approx 0$  meV,  $\Delta_{2e(1)} \approx 10$  meV,  $\Delta_{2e(2)} \approx -10$  meV,  $\Delta_{1e1h} \approx 14$  meV,  $\Delta_{3e1h} \approx 14$  meV,  $\Delta_{2e1h(1)} \approx 24$  meV and  $\Delta_{2e1h(2)} \approx 4$  meV. According to the definition of  $V_{Gate}(\Delta)$  in Eq. (4.1), we have:

$$\begin{aligned} V_{Gate}(\Delta_{2e1h(1)}) &< V_{Gate}(\Delta_{1e1h}) \approx V_{Gate}(\Delta_{3e1h}) < \\ &< V_{Gate}(\Delta_{2e(1)}) < V_{Gate}(\Delta_{2e1h(2)}) < V_{Gate}(\Delta_e). \end{aligned} \quad (4.29)$$

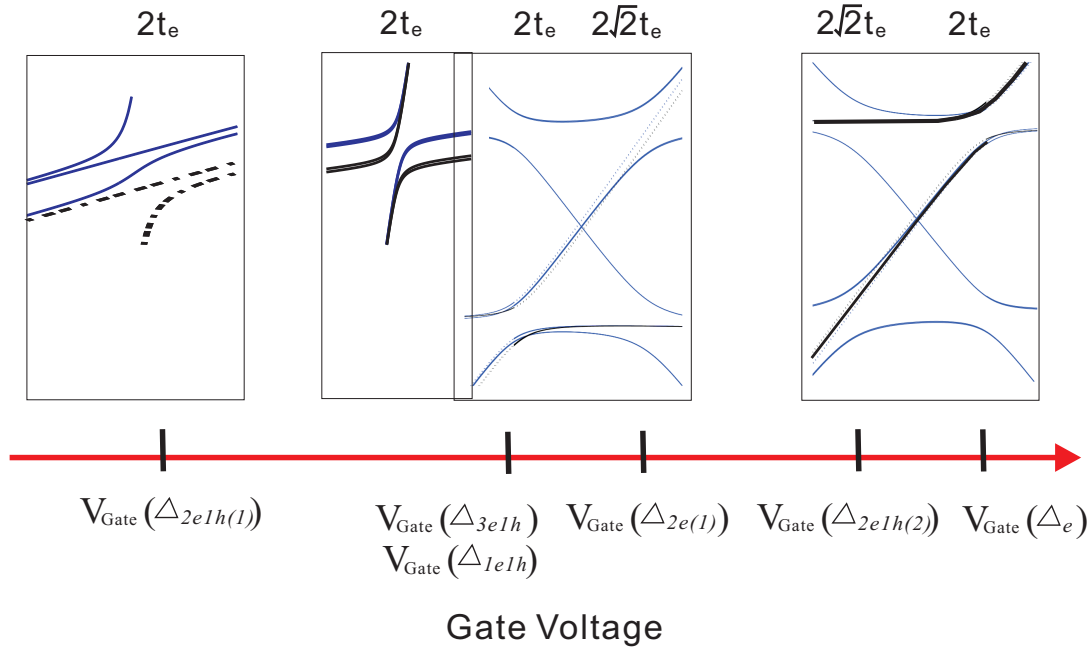


**Figure 4.9:** Gate-voltage map for charge and spin configurations involved in coherent coupling in CQDs system. The tunneling rates are indicated by neglecting the Coulomb terms for better qualitative comparison between different tunnel couplings.

We mark these gate voltages qualitatively on the axis and link them to the corresponding optical transition patterns as shown in Fig. 4.9, so that we can get a map for indicating the relative position for each coupling in CQDs system. We can also label the tunneling rate for each resonance point onto the map. As we did in Fig. 4.9,



for better qualitative comparison, we neglect the Coulomb terms in the tunneling rate here and use  $2t_e$  and  $2\sqrt{2}t_e$  to indicate the cases of single-electron tunneling and two-electron tunneling, respectively. Eventually, a pair of the resonance gate voltage and the corresponding tunneling rate becomes a joint signature for a certain charge and spin configuration in CQDs. For example, by observing the PL data in Fig. 4.1, we can immediately identify the two main features corresponding to the  $1e1h$  transitions and the  $3e1h$  transitions, respectively.

Moreover, since  $V_{Gate}(\Delta_{1e1h}) \approx V_{Gate}(\Delta_{3e1h})$ , from the map, the  $1e1h$  transitions and the  $3e1h$  transitions are supposed to have overlaps in the spectrum, which can provide us a feasible explanation for the unpredicted passing-through PL data in both transition patters.



## Chapter 5

# Outlook

### 5.1 Towards single-shot measurement of an electron spin

We notice that the title of this section is identical to the one of subsection 3.3.3, since we will continue the previous discussion here by proposing one solution to the question left before. The question is about how to make the back-action time ( $T_{BA}$ ) much longer than the characteristic time for the dynamics we want to probe. Meanwhile, the measurement time ( $T_m$ ) is required to be small enough for resolving the dynamics and big enough for good SNR. As we learnt in subsection 3.3.2, in single QDs, the spin-relaxation time  $T_1$  can be tens of millisecond, and the RFL measurement time ( $T_m$ ) with good SNR can be tens of microsecond. The only obstacle there is the back-action time which is with the order of one microsecond. The back action in single QD is due to the hyperfine interaction and the heavy-light hole mixing. The hyperfine interaction can be suppressed by increasing the external magnetic field, however the hole mixing is independent on magnetic field. There is a solution can be used to suppress both of them, that is to reduce the wavefunction overlap of the hole and the target electron. The CQDs provide us a system where the target electron can be placed in one dot and optical transitions can be probed in the other dot. The similar idea for probing the charge state, named as “charge sensing”, has been realized by Falt *et. al.* [60]. For probing the spin states, Kim *et. al.* [17] have demonstrated this idea using DT measurement and showing no significant back action within the measurement time scale. But for probing the spin dynamics, DT readout is not as fast as RFL readout, therefore, we propose a single-shot RFL measurement in CQDs for single-spin readout.

For demonstrating the feasibility of our proposal, we give an overview on how to identify the spin states and suppress the measurement induced back action in CQDs.

As we learnt from subsection 4.3.2, if we select the single electron in blue dot as the target electron, the corresponding optical transitions in red dot are shown in Fig. 4.6. Setting the gate voltage at 565 mV where blue dot is in single-electron cotunneling regime, we carry out DT measurements under swept magnetic field. The idea here is to use magnetic field lifting the spin degeneracy. Staying in cotunneling regime is to make sure we have the visible signal in spite of any possible spin pumping effects. The measured data are shown in Fig. 5.1 (b). The corresponding simulations for the excited states and ground states are shown in Fig. 5.1 (a).

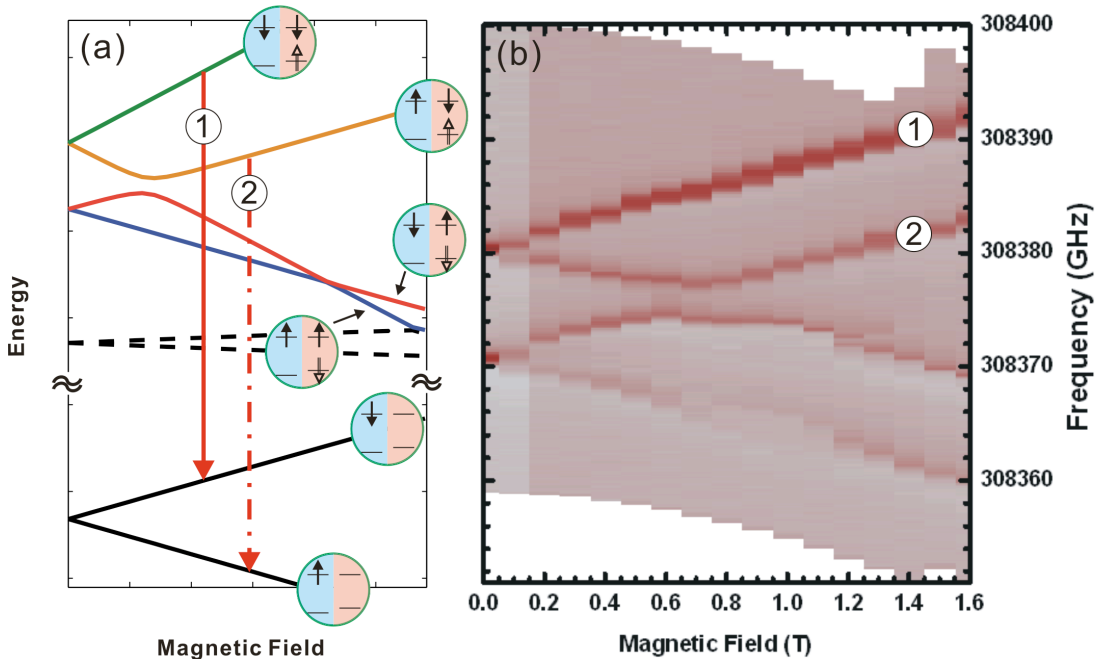


**Figure 5.1:** Magnetic sweep of DT on red dot of a CQDs pair. (a) The simulation for the excited states and ground states involved in  $2e1h$  transitions with fixed gate voltage but swept magnetic field. The dashed black curves indicate the splitting for intra-dot dark states which are negligible for optical transitions. (b) Magnetic sweep of DT on red dot of CQD2 at 565 mV with the magnetic field range from 0 to 1.6 Tesla. the diamagnetic shift is subtracted from the data.

We indicate relevant states by using their most possible state components in Fig. 5.1 (a). Considering transitions ① and ②, they both correspond to the  $\sigma_+$  transition. In the case of single QDs, this two transitions are degenerate in magnetic field. However, the observation from CQDs suggests the electron tunnel coupling altering the electron wavefunction, so that the two transitions are distinguishable. The energy splitting of them is consistent with the splitting we observed in DT for two

bright transitions under zero magnetic field, there the kinetic exchange interaction dominates the splitting. Compared with transition ①, the weak signal of transition ② does not necessarily suggest a weak spin-pumping effect, since state  $(\uparrow, \downarrow\uparrow)$  could mix with state  $(\uparrow\downarrow, \uparrow)$  via electron tunneling coupling, and state  $(\uparrow\downarrow, \uparrow)$  is optically non-favorable for DT due to its indirect excitation. Whereas, transition ① has the excited state with two parallel electron spins, due to Pauli exclusion principle, two electrons repel each other, therefore, both the mixing with other states and the potential spin pumping are suppressed. According to these analysis, when we probe transition ①, we expect the time scale for  $T_{BA}$  is much larger than spin-relaxation time  $T_1$ . In principle, recording real-time stamps of single electron spin dynamics dominated by spin relaxation can be achieved by single-shot RFL readout with a comfortable timebin for good SNR in CQDs system. For seeing that, we still need more investigations on CQDs system. For calibration, N-shot measurements are suggested for statistically revealing the dynamics expected and unexpected.

## 5.2 Probing nuclear-spin dynamics using resonance fluorescence

The studies on dynamics of nuclear spin in QDs always have great impacts on both QIP applications and the fundamental research for mesoscopic system. For competing the drawback of the electron-spin dephasing, which is induced by the nuclear-spin fluctuation, several experiments were carried out to polarize the nuclear spin for suppressing their fluctuations [65, 66, 67, 68, 69, 70, 71]. Our recent work [25] revealed a bi-directional polarization mechanism for the nuclear spin using resonant laser driving a singly charged QD. More interestingly, we observed similar phenomena by resonantly driving the neutral QDs. Those phenomena could not yet be well explained by our model applied in the case of singly charged QDs. Most of those measurements were done by DT. We suggest RFL measurements on the studies of nuclear-spin dynamics, both the fast RFL readout and spectrum resolving can provide us insightful information for approaching the eventual understanding. We would like to show one measurement of spectrum, which is applied for revealing the change of the resonance for a transition interacting with the nuclear-spin reservoir. Under 6 Tesla magnetic field, we measure the RFL spectrum of  $X^0$  transition for a series of laser frequencies. With the laser frequency dunned from small value to big value, we extract the effective Rabi frequencies by measuring the frequency

separation between the central Mollow peak and a side Mollow peak, we plot data in Fig. 5.2. What we observed is that, the separation gets smaller when we are approaching the resonance, once we reach the resonance, the resonant condition will be kept for about 2 GHz laser frequency detuning, which is expected as the result of polarizing nuclear spin forming a compensate magnetic field to the laser detuning. After reaching one critical frequency point, the resonance will be lost abruptly. RFL spectrum measurements can unambiguously reveal the resonance, so that we are convinced the the transition is resonantly locked onto the laser for a 2 GHz tuning range. However, there are still plenty of features in this measurement even beyond our current phenomenological understanding. Those are worthy of more investigations in the near future.

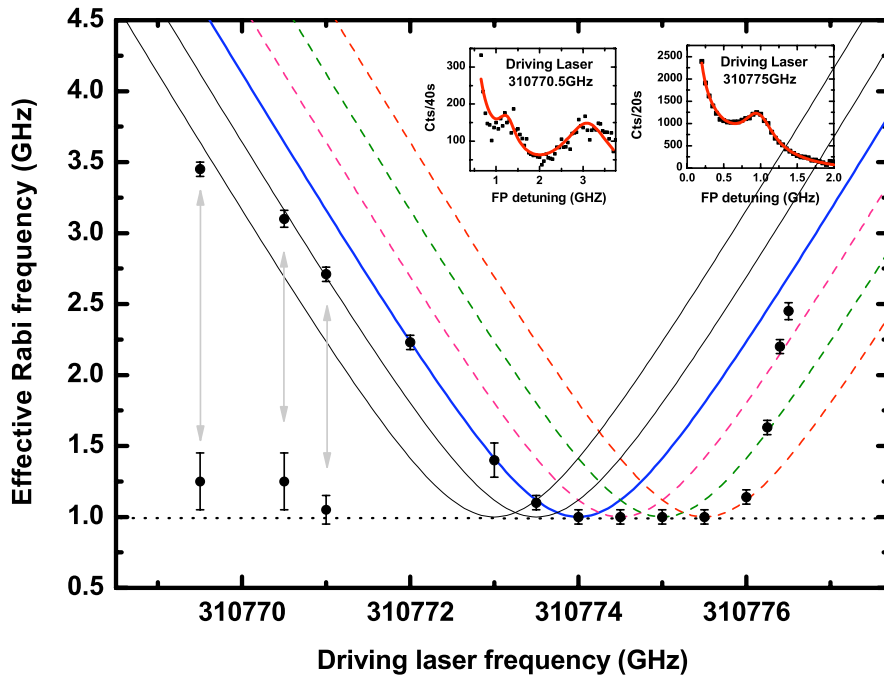


**Figure 5.2:** Extracted effective Rabi frequencies from  $X^0$  RFL spectrum measurements for a laser tuning from lower frequency to higher frequency under 6 Tesla magnetic field. The laser power is about 412 nW. The calculated quadratic curves indicate the expected Rabi frequencies respect to the previous one without any effects from environment. The two inserts show the raw spectrum data measured for two laser frequencies of being far detuned and being resonant, respectively.

### 5.3 More in the near future

The CQDs provide us a more complicate and challengeable system. The study of the multi-electron spin states, especially the two-electron singlets and triplets, are drawing more and more attentions due to their useful properties with respect to spin-related dephasing [72, 73], as seen in recent experiments in electrically controlled CQDs [74, 71]. For the case of self-assembled CQDs, our plan is to realize the preparation, manipulation [75] and readout of singlet-triplet states. RFL will be used there as a powerful technique to reveal the dynamics of multi-spin states via n-shot or single-shot measurements. Base on the singlet-triplet states, we will investigate the coherent generation of photon pairs from CQDs carrying electron-spin information towards the photon-electron entanglement and the photon-photon entanglement. We are also interested in investigating the the two-qubit logic gates based on dipole-dipole interaction between charged excitons in CQDs [76] for quantum computation.





# Summary

In this work, firstly, we demonstrated the spin-resolved resonance fluorescence from a single quantum dot. Under zero magnetic field, two electron spins are degenerate, so the Mollow triplet is the characteristic spectrum for resonance fluorescence photons. We measured the Mollow-triplet spectrum under the control of laser power and laser frequency, respectively. In the case of power control, we extracted the transition linewidth  $\Gamma$  from the sideband spectrum, and compared it with the spontaneous emission rate  $\Gamma_{sp}$  extracted from life time measurements. As a result, an upper bound of the dephasing rate is estimated as 80 MHz. Together with the small laser background contribution ( $< 2\%$ ) and the photon anti-bunching behavior in  $g^{(2)}$  measurements, we claimed the sideband emissions are background-free and near transform-limited single photons. Under nonzero magnetic field, the spin degeneracy is lifted. If the single driving laser couples two spin transitions with different strengths, the Mollow quintuplet can be observed in the spectrum with split sideband tagged by two spin states.

Secondly, instead of resolving the spectrum, we probed the optical transitions by counting resonantly scattered photons with moderate excitation power. Compared with the differential transmission technique, resonance fluorescence readout provides better SNR with the same measurement time scale. We carried out n-shot time-resolved resonance fluorescence measurements on spin-selective transitions to reveal the electron spin dynamics of the measurement induced back action and the spin relaxation. The characteristic time  $T_{BA}$  for the back action was studied under the control of gate voltage, laser frequency, laser power and external magnetic field, respectively. Especially the magnetic field dependence identifies the hyperfine interaction dominating the back action up to 0.6 Tesla, and the heavy-light hole mixing dominating the case of higher field. The spin relaxation time scale  $T_1$  was also studied under different magnetic fields. As a result, the phonon assisted spin-orbit interaction is identified to dominate the spin-flip precess by mixing the ground

states under the magnetic fields larger than 2 Tesla. Then, we analyzed time scales  $T_m$ ,  $T_{BA}$  and  $T_1$  to investigate the possibility for pursuing single-shot spin readout. It turns out that, with our current setup, for the case of single quantum dots system, the condition is  $T_{BA} < T_m < T_1$ , which implies no electron spin information can be extracted. The ultimate solution is to suppress the back action. Coupled quantum dots system is expected to provide this solution.

Thirdly, we had a comprehensive study on charge-spin configurations in the coupled quantum dots system. We established a theoretical model and matched the simulations to the spectrum we observed from both PL and DT measurements and explained the electron tunnel coupling events involved.

At the end, we propose a single-shot spin readout measurement base on the (1e,1e1h) charge-spin configurations in coupled quantum dots system.

# Bibliography

- [1] Qiang Zhang, Alexander Goebel, Claudia Wagenknecht, Yu-Ao Chen, Bo Zhao, Tao Yang, Alois Mair, Jörg Schmiedmayer, and Jian-Wei Pan. Experimental quantum teleportation of a two-qubit composite system. *Nature Physics*, 2:678, Oct 2006.
- [2] J. Kim, O. Benson, H. Kan, and Y. Yamamoto. A single-photon turnstile device. *Nature*, 397:500, Feb 1999.
- [3] P. Michler, A. Kiraz, C. Becher, W. V. Schoenfeld, P. M. Petroff, Lidong Zhang, E. Hu, and A. Imamoglu. A quantum dot single-photon turnstile device. *Science*, 290:2282, Dec 2000.
- [4] Matthew Pelton, Charles Santori, Jelena Vučković, Bingyang Zhang, Glenn S Solomon, Jocelyn Plant, and Yoshihisa Yamamoto. Efficient source of single photons a single quantum dot in a micropost microcavity. *Physical Review Letters*, 89:233602, Nov 2002.
- [5] Charles Santori, David Fattal, Jelena Vučković, Glenn S Solomon, and Yoshihisa Yamamoto. Indistinguishing photons from a single-photon device. *Nature*, 419:594, Oct 2002.
- [6] Charles Santori, David Fattal, Jelena Vuckovic, Glenn S Solomon, and Yoshihisa Yamamoto. Single-photon generation with InAs quantum dots. *New Journal of Physics*, 6:89, Jul 2004.
- [7] A. Nick Vamivakas, Yong Zhao, Chao-Yang Lu, and Mete Atatüre. Spin-resolved quantum-dot resonance fluorescence. *Nature Physics*, 5:198, Jan 2009.
- [8] E. B. Flagg, A. Muller, J. W. Robertson, S. Founta, D. G. Deppe, M. Xiao, W. Ma., G. J. Salamo, and C. K. Shih. Resonantly driven coherent oscillations in a solid-state quantum emitter. *Nature Physics*, 5(3):203, Jan 2009.

- [9] A. Muller, E. B. Flagg, P. Bianucci, X. Y. Wang, D. G. Deppe, W. Ma, J. Zhang, G. J. Salamo, M. Xiao, and C. K. Shih. Resonance fluorescence from a coherently driven semiconductor quantum dot in a cavity. *Physical Review Letters*, 99(18):187402, 2007.
- [10] Serkan Ates, Sven Markus Ulrich, Stephan Reizenstein, Andreas Loeffler, Alfred Forchel, and Peter Michler. Indistinguishable photons from the resonance fluorescence of a single quantum dot in a microcavity. *arXiv*, quant-ph:0902.3612, Feb 2009.
- [11] Alexander Högele, Martin Kroner, Stefan Seidl, Khaled Karrai, Mete Atatüre, Jan Dreiser, Atac Imamoglu, Richard J Warburton, Antonio Badolato, Brian D Gerardot, and Pierre M Petroff. Spin-selective optical absorption of singly charged excitons in a quantum dot. *Applied Physics Letters*, 86(22):221905, Jan 2005.
- [12] Mete Atatüre, Jan Dreiser, Antonio Badolato, Alexander Högele, Khaled Karrai, and Atac Imamoglu. Quantum-dot spin-state preparation with near-unity fidelity. *Science*, 312(5773):551, Apr 2006.
- [13] Jan Dreiser, Mete Atatüre, Christophe Galland, Tina Müller, Antonio Badolato, and Atac Imamoglu. Optical investigations of quantum dot spin dynamics as a function of external electric and magnetic fields. *Physical Review B*, 77(7):15, Feb 2008.
- [14] David Press, Thaddeus D Ladd, Bingyang Zhang, and Yoshihisa Yamamoto. Complete quantum control of a single quantum dot spin using ultrafast optical pulses. *Nature*, 456(7219):218, Nov 2008.
- [15] J. Berezovsky, M. H. Mikkelsen, O. Gywat, N. G. Stoltz, L. A. Coldren, and D. D. Awschalom. Nondestructive optical measurements of a single electron spin in a quantum dot. *Science*, 314(5807):1916, Dec 2006.
- [16] M. Atatüre, J. Dreiser, A. Badolato, and A. Imamoglu. Observation of faraday rotation from a single confined spin. *Nature Physics*, 3(2):101, 2007.
- [17] Danny Kim, Sophia E Economou, Ștefan C Bădescu, Michael Scheibner, Allan S Bracker, Mark Bashkansky, Thomas L Reinecke, and Daniel Gammon. Optical spin initialization and nondestructive measurement in a quantum dot molecule. *Physical Review Letters*, 101(23):236804, Dec 2008.

- [18] J. A. Venables, G. D. T. Spiller, and M. Hanbucken. Nucleation and growth of thin films. *Reports on Progress in Physics*, 47(4):399, 1984.
- [19] J. M. Garcia, T. Mankad, P. O. Holtz, P. J. Wellman, and P. M. Petroff. Electronic states tuning of InAs self-assembled quantum dots. *Applied Physics Letters*, 72(24):3172–3174, 1998.
- [20] Mete Atature. Quantum optics with quantum-dot spins. *Habilitationsschrift, ETH*, 2007.
- [21] R Warburton, C Schafflein, D Haft, F Bickel, A Lorke, K Karrai, J Garcia, W Schoenfeld, and P Petroff. Optical emission from a charge-tunable quantum ring. *Nature*, 405(6789):926, Jun 2000.
- [22] Jan Dreiser. Optical study, preparation and measurement of a single quantum-dot spin. *PhD dissertation, ETH*, 2007.
- [23] M. Bayer, G. Ortner, O. Stern, A. Kuther, A. A. Gorbunov, A. Forchel, T. L. Reinecke, S. N. Walck, J. P. Reithmaier, F. Kloppe, and F. Schäfer. Fine structure of neutral and charged excitons in self-assembled In(Ga)As/(Al)GaAs quantum dots. *Physical Review B*, 65(19):23, May 2002.
- [24] Xiaodong Xu, Bo Sun, Paul R Berman, Duncan G Steel, Allan S Bracker, Dan Gammon, and L. J Sham. Coherent population trapping of an electron spin in a single negatively charged quantum dot. *Nature Physics*, 4(9):692, Sep 2008.
- [25] C. Latta, A. Hoge, Y. Zhao, A. N. Vamivakas, P. Maletinsky, M. Kroner, J. Dreiser, I. Carusotto, A. Badolato, D. Schuh, W. Wegscheider, M. Atature, and A. Imamoglu. Confluence of resonant laser excitation and bidirectional quantum-dot nuclear-spin polarization. *Nature Physics*, advance online publication, Aug 2009. 10.1038/nphys1363.
- [26] Xiaodong Xu, Wang Yao, Bo Sun, Duncan G Steel, Allan S Bracker, Daniel Gammon, and L J Sham. Optically controlled locking of the nuclear field via coherent dark-state spectroscopy. *Nature*, 459(7250):1105, Jun 2009.
- [27] Brian D Gerardot, Daniel Brunner, Paul A Dalgarno, Patrik Öhberg, Stefan Seidl, Martin Kroner, Khaled Karrai, Nick G Stoltz, Pierre M Petroff, and Richard J Warburton. Optical pumping of a single hole spin in a quantum dot. *Nature*, 451(7177):441, Jan 2008.

- [28] Daniel Brunner, Brian D. Gerardot, Paul A. Dalgarno, Gunter Wust, Khaled Karrai, Nick G. Stoltz, Pierre M. Petroff, and Richard J. Warburton. A Coherent Single-Hole Spin in a Semiconductor. *Science*, 325(5936):70, 2009.
- [29] K. Karrai and R. J. Warburton. Optical transmission and reflection spectroscopy of single quantum dots. *Superlattices and Microstructures*, 33(5-6):311, 2003.
- [30] B. R. Mollow. Power spectrum of light scattered by two-level systems. *Physical Review*, 188(5):1969, 1969.
- [31] Marlan O. Scully and M. Suhail Zubairy. *Quantum Optics*. Cambridge University Press, Cambridge, 2000.
- [32] Rodney Loudon. *The Quantum Theory of Light*. Oxford university press, Oxford, 2000.
- [33] Melvin Lax. Formal theory of quantum fluctuations from a driven state. *Physical Review*, 129(5):2342, Mar 1963.
- [34] J. Eberly and P. W. Milonni. *Quantum Optics*. Encyclopedia of Physical Science and Technology, Vol 11. Academic Press, 1987.
- [35] Claude Cohen-Tannoudji, Jacques Dupont-Roc, Gilbert Grynberg. *Atom-Photon Interactions*. WILEY-VCH Verlag GmbH & Co. KGaA, Weinheim, 2004.
- [36] D. Walls and G. Milburn. *Quantum Optics*. Springer, Berlin, 1994.
- [37] J. Berezovsky, M. H. Mikkelsen, N. G. Stoltz, L. A. Coldren, and D. D. Awschalom. Picosecond Coherent Optical Manipulation of a Single Electron Spin in a Quantum Dot. *Science*, 320(5874):349, 2008.
- [38] X Xu, B Sun, P. R Berman, D. G Steel, A. S Bracker, D Gammon, and L. J Sham. Coherent optical spectroscopy of a strongly driven quantum dot. *Science*, 317(5840):929–932, Aug 2007.
- [39] Gregor Jundt, Lucio Robledo, Alexander Hoge, Stefan Falt, and Atac Imamoglu. Observation of dressed excitonic states in a single quantum dot. *Physical Review Letters*, 100(17):177401, 2008.

- [40] Thomas Unold, Kerstin Mueller, Christoph Lienau, Thomas Elsaesser, and Andreas D. Wieck. Optical stark effect in a quantum dot: Ultrafast control of single exciton polarizations. *Physical Review Letters*, 92(15):157401, Apr 2004.
- [41] A. Kiraz, M. Atatüre, and A. Imamoglu. Quantum-dot single-photon sources: Prospects for applications in linear optics quantum-information processing. *Physical Review A*, 69(3):032305, Mar 2004.
- [42] A. Aspect, G. Roger, S. Reynaud, J. Dalibard, and C. Cohen-Tannoudji. Time correlations between the two sidebands of the resonance fluorescence triplet. *Physical Review Letters*, 45(8):617, Aug 1980.
- [43] A. N. Vamivakas, M. Atatüre, J Dreiser, S. T. Yilmaz, A. Badolato, A. K. Swan, B. B. Goldberg, A. Imamoglu, and M. S. Ünlü. Strong extinction of a far-field laser beam by a single quantum dot. *Nano Letters*, 7:2892, May 2007.
- [44] I. A. Merkulov, Al. L. Efros, and M. Rosen. Electron spin relaxation by nuclei in semiconductor quantum dots. *Physical Review B*, 65(20):205309, Apr 2002.
- [45] Changxue Deng and Xuedong Hu. Electron-spin dephasing via hyperfine interaction in a quantum dot: An equation-of-motion calculation of electron-spin correlation functions. *Physical Review B*, 78(24):245301, 2008.
- [46] P. Maletinsky, A. Badolato, and A. Imamoglu. Dynamics of quantum dot nuclear spin polarization controlled by a single electron. *Physical Review Letters*, 99(5):056804, 2007.
- [47] Alexander V. Khaetskii and Yuli V. Nazarov. Spin relaxation in semiconductor quantum dots. *Physical Review B*, 61(19):12639, May 2000.
- [48] R. Hanson, L. P. Kouwenhoven, J. R. Petta, S. Tarucha, and L. M. K. Vandersypen. Spins in few-electron quantum dots. *Reviews of Modern Physics*, 79(4):1217, 2007.
- [49] Alexander V. Khaetskii and Yuli V. Nazarov. Spin-flip transitions between zeeman sublevels in semiconductor quantum dots. *Physical Review B*, 64(12):125316, Sep 2001.
- [50] Sigurdur I. Erlingsson and Yuli V. Nazarov. Hyperfine-mediated transitions between a zeeman split doublet in gaas quantum dots: The role of the internal field. *Physical Review B*, 66(15):155327, Oct 2002.

- [51] D. V. Averin and Yu. V. Nazarov. Virtual electron diffusion during quantum tunneling of the electric charge. *Physical Review Letters*, 65(19):2446, Nov 1990.
- [52] J. M. Smith, P. A. Dalgarno, R. J. Warburton, A. O. Govorov, K. Karrai, B. D. Gerardot, and P. M. Petroff. Voltage control of the spin dynamics of an exciton in a semiconductor quantum dot. *Physical Review Letters*, 94(19):197402, May 2005.
- [53] Gabriel Bester, Selvakumar Nair, and Alex Zunger. Pseudopotential calculation of the excitonic fine structure of million-atom self-assembled  $\text{In}_{1-x}\text{Ga}_x\text{As}/\text{GaAs}$  quantum dots. *Physical Review B*, 67(16):161306, Apr 2003.
- [54] M Kroutvar, Y Ducommun, Dominik Heiss, M Bichler, D Schuh, G Abstreiter, and J J Finley. Optically programmable electron spin memory using semiconductor quantum dots. *Nature*, 432(7013):81, Nov 2004.
- [55] A. H. Myerson, D. J. Szwer, S. C. Webster, D. T. C. Allcock, M. J. Curtis, G. Imreh, J. A. Sherman, D. N. Stacey, A. M. Steane, and D. M. Lucas. High-fidelity readout of trapped-ion qubits. *Physical Review Letters*, 100(20):200502, 2008.
- [56] H. J. Krenner, M. Sabathil, E. C. Clark, A. Kress, D. Schuh, M. Bichler, G. Abstreiter, and J. J. Finley. Direct observation of controlled coupling in an individual quantum dot molecule. *Physical Review Letters*, 94(5):057402, Feb 2005.
- [57] H. J. Krenner, E. C. Clark, T. Nakaoka, M. Bichler, C. Scheurer, G. Abstreiter, and J. J. Finley. Optically probing spin and charge interactions in a tunable artificial molecule. *Physical Review Letters*, 97(7):076403, 2006.
- [58] E. A. Stinaff, M. Scheibner, A. S. Bracker, I. V. Ponomarev, V. L. Korenev, M. E. Ware, M. F. Doty, T. L. Reinecke, and D. Gammon. Optical Signatures of Coupled Quantum Dots. *Science*, 311(5761):636, 2006.
- [59] M. Scheibner, M. F. Doty, I. V. Ponomarev, A. S. Bracker, E. A. Stinaff, V. L. Korenev, T. L. Reinecke, and D. Gammon. Spin fine structure of optically excited quantum dot molecules. *Physical Review B*, 75(24):245318, 2007.
- [60] Stefan Falt, Mete Atatüre, Hakan E. Türeci, Yong Zhao, Antonio Badolato, and Atac Imamoglu. Strong electron-hole exchange in coherently coupled quantum dots. *Physical Review Letters*, 100(10):106401, 2008.



- [61] M Scheibner, M Yakes, A. S Bracker, I. V Ponomarev, M. F Doty, C. S Hellberg, L. J Whitman, T. L Reinecke, and D Gammon. Optically mapping the electronic structure of coupled quantum dots. *Nature Physics*, 4(4):291, Apr 2008.
- [62] T. Takagahara. Effects of dielectric confinement and electron-hole exchange interaction on excitonic states in semiconductor quantum dots. *Physical Review B*, 47(8):4569, Feb 1993.
- [63] M. F. Doty, M. Scheibner, A. S. Bracker, I. V. Ponomarev, T. L. Reinecke, and D. Gammon. Optical spectra of doubly charged quantum dot molecules in electric and magnetic fields. *Physical Review B (Condensed Matter and Materials Physics)*, 78(11):115316, 2008.
- [64] L Robledo, J Elzerman, G Jundt, M Atature, A Hoge, S Falt, and A Imamoglu. Conditional dynamics of interacting quantum dots. *Science*, 320(5877):772, May 2008.
- [65] D. Gammon, Al. L. Efros, T. A. Kennedy, M. Rosen, D. S. Katzer, D. Park, S. W. Brown, V. L. Korenev, and I. A. Merkulov. Electron and nuclear spin interactions in the optical spectra of single gaas quantum dots. *Physical Review Letters*, 86(22):5176, May 2001.
- [66] B. Eble, O. Krebs, A. Lemaitre, K. Kowalik, A. Kudelski, P. Voisin, B. Urbaszek, X. Marie, and T. Amand. Dynamic nuclear polarization of a single charge-tunable inas/gaas quantum dot. *Physical Review B*, 74(8):081306, 2006.
- [67] F. H. L Koppens, C Buizert, K. J Tielrooij, I. T Vink, K. C Nowack, T Meunier, L. P Kouwenhoven, and L. M. K Vandersypen. Driven coherent oscillations of a single electron spin in a quantum dot. *Nature*, 442(7104):766, Aug 2006.
- [68] C. W. Lai, P. Maletinsky, A. Badolato, and A. Imamoglu. Knight-field-enabled nuclear spin polarization in single quantum dots. *Physical Review Letters*, 96(16):167403, 2006.
- [69] P. Maletinsky, C. W. Lai, A. Badolato, and A. Imamoglu. Nonlinear dynamics of quantum dot nuclear spins. *Physical Review B*, 75(3):035409, 2007.
- [70] A. I. Tartakovskii, T. Wright, A. Russell, V. I. Fal'ko, A. B. Van'kov, J. Skiba-Szymanska, I. Drouzas, R. S. Kolodka, M. S. Skolnick, P. W. Fry, A. Tahraoui,

- H.-Y. Liu, and M. Hopkinson. Nuclear spin switch in semiconductor quantum dots. *Physical Review Letters*, 98(2):026806, 2007.
- [71] D. J. Reilly, J. M. Taylor, J. R. Petta, C. M. Marcus, M. P. Hanson, and A. C. Gossard. Suppressing Spin Qubit Dephasing by Nuclear State Preparation. *Science*, 321(5890):817, 2008.
- [72] P. Zanardi and M. Rasetti. Noiseless quantum codes. *Physical Review Letters*, 79(17):3306, Oct 1997.
- [73] D. A. Lidar, I. L. Chuang, and K. B. Whaley. Decoherence-free subspaces for quantum computation. *Physical Review Letters*, 81(12):2594, Sep 1998.
- [74] J. R. Petta, A. C. Johnson, J. M. Taylor, E. A. Laird, A. Yacoby, M. D. Lukin, C. M. Marcus, M. P. Hanson, and A. C. Gossard. Coherent Manipulation of Coupled Electron Spins in Semiconductor Quantum Dots. *Science*, 309(5744):2180, 2005.
- [75] Hakan E. Tureci, J. M. Taylor, and A. Imamoglu. Coherent optical manipulation of triplet-singlet states in coupled quantum dots. *Physical Review B*, 75(23):235313, 2007.
- [76] T. Calarco, A. Datta, P. Fedichev, E. Pazy, and P. Zoller. Spin-based all-optical quantum computation with quantum dots: Understanding and suppressing decoherence. *Physical Review A*, 68(1):012310, Jul 2003.

# List of Figures

1.1	Illustrated formation of self-assembled InAs/GaAs QDs . . . . .	3
1.2	Schematic diagram of the steps in the PCI technique for blue-shifting the emission from QDs . . . . .	3
1.3	Schematic diagram of the stacking of quantum dots . . . . .	4
1.4	Band structure diagram for single QD and coupled QDs . . . . .	5
1.5	Processes in a photoluminescence experiment with an exciton ( $X^0$ ) in single QD and a trion ( $X^{1-}$ ) in single QD . . . . .	6
1.6	Typical photoluminescence spectrum from a single quantum dot with tentative identification of transitions . . . . .	7
1.7	Schematic of the charge controlling device . . . . .	8
1.8	Voltage sweep of photoluminescence spectrum for different samples .	9
1.9	Resonant excitation of singly charge QD . . . . .	11
1.10	Detecting coherently scattered photons by differential transmission .	12
1.11	Typical DT data for $X^{1-}$ transition . . . . .	13
2.1	Simulations for time delay $\tau$ dependence of resonance fluorescence second correlation function for zero detuning and different Rabi fre- quencies . . . . .	19
2.2	Schematic of dressed states for a two-level system resonantly driven by a single mode light field . . . . .	21
2.3	Degenerate two two-level systems in singly charged QD, and control- measure interface of QD operating system . . . . .	24
2.4	Tunable CW laser frequency and power control system and Fabry Perot cavity based high resolution spectrometer . . . . .	25
2.5	Laser frequency stabilization. . . . .	26
2.6	The measured transmission linewidth of the FP cavity . . . . .	27

2.7	The experimental scheme for $g^{(2)}$ and photon lifetime measurements.	28
2.8	Power dependent resonance fluorescence . . . . .	29
2.9	Indirect and direct life-time measurement . . . . .	30
2.10	Dependence of resonance fluorescence on laser detuning . . . . .	31
2.11	Spin-selective dynamic Stark effect . . . . .	33
2.12	Mollow quintuplet and spin-resolved fluorescence . . . . .	34
2.13	Second-order correlation function for RFL . . . . .	35
3.1	The integrated resonance fluorescence from the $X^{1-}$ transition as a function of laser detuning . . . . .	40
3.2	The systematic calibrations of the transition readout using reso- nance fluorescence as a function of laser power . . . . .	41
3.3	Electron spin pumping and time-resolved resonance fluorescence measurement . . . . .	48
3.4	Dependence of the spin-pumping rate as a function of the excitation laser frequency detuning for a fixed laser power . . . . .	50
3.5	Dependence of the spin-pumping rate as a function of the excitation laser power . . . . .	51
3.6	The magnetic field dependence of the spin-pumping rate with a fixed laser power . . . . .	52
3.7	The n-shot TRRFL measurement for electron spin relaxation . . . .	53
3.8	The n-shot TRRFL measurements for spin relaxation . . . . .	55
3.9	The schematic for the ideas of n-shot measurement and single-shot measurement . . . . .	56
3.10	Single-shot readout for $X^{1-}$ transition at zero magnetic field . . . .	58
4.1	Gate sweep of photoluminescence spectrum for the red dot of a coupled quantum dots pair (CQD1) with the tunneling barrier of 13 nm . . . . .	60
4.2	The energy band diagram of the vertically stacked CQDs. . . . .	61
4.3	The schematic energy dispersion diagram for the singly charged and doubly charged CQDs ground states . . . . .	62
4.4	The energy dispersion for the $1e1h$ system . . . . .	70
4.5	The energy dispersion for the $3e1h$ system . . . . .	75

4.6	Two dimensional DT scan for both the blue dot and red dot of CQD2 under zero magnetic field . . . . .	78
4.7	The energy dispersion for the $2e1h$ system . . . . .	82
4.8	The DT data for the $3e1h$ system . . . . .	83
4.9	Gate-voltage map for charge and spin configurations involved in coherent coupling in CQDs system . . . . .	84
5.1	Magnetic sweep of DT on red dot of a CQDs pair . . . . .	88
5.2	Extracted effective Rabi frequencies from $X^0$ RFL spectrum measurements for a laser tuning from lower frequency to higher frequency under 6 Tesla magnetic field . . . . .	90



# List of Tables

4.1	Matrix elements of the Hamiltonian $H_{(2e)}$ with the states from $ 1\rangle_{(2e)}$ to $ 6\rangle_{(2e)}$ as the basis . . . . .	65
4.2	Matrix elements of the diagonal block $H_{(1e1h)B}$ of the Hamiltonian $H_{(1e1h)}$ with the states from $ 1\rangle_{(1e1h)}$ to $ 4\rangle_{(1e1h)}$ as the basis. . . . .	69
4.3	Matrix elements of the diagonal block $H_{(1e1h)D}$ of the Hamiltonian $H_{(1e1h)}$ with the states from $ 5\rangle_{(1e1h)}$ to $ 8\rangle_{(1e1h)}$ as the basis . . . . .	69
4.4	Matrix elements of the diagonal block $H_{(3e1h)B}$ of the Hamiltonian $H_{(3e1h)}$ with the states from $ 1\rangle_{(3e1h)}$ to $ 4\rangle_{(3e1h)}$ as the basis . . . . .	73
4.5	Matrix elements of the diagonal block $H_{(3e1h)D}$ of the Hamiltonian $H_{(3e1h)}$ with the states from $ 5\rangle_{(3e1h)}$ to $ 8\rangle_{(3e1h)}$ as the basis . . . . .	73
4.6	Matrix elements of the diagonal block $H_{(2e1h)\uparrow}$ of the Hamiltonian $H_{(2e1h)}$ with the states from $ 1\rangle_{(2e1h)}$ to $ 6\rangle_{(2e1h)}$ as the basis . . . . .	80
4.7	Matrix elements of the diagonal block $H_{(2e1h)\downarrow}$ of the Hamiltonian $H_{(2e1h)}$ with the states from $ 7\rangle_{(2e1h)}$ to $ 12\rangle_{(2e1h)}$ as the basis . . . . .	80
4.8	Matrix elements of the off-diagonal block $H_{(2e1h)\uparrow\leftrightarrow\downarrow}$ of the Hamiltonian $H_{(2e1h)}$ . . . . .	81





# List of publications

1. C.-Y. Lu, **Y. Zhao**, A. N. Vamivakas, C. Matthiesen, S. Faelt, A. Badolato and M. Atatüre. Direct Measurement of Quantum Dot Spin Dynamics using Time-Resolved Resonance Fluorescence. *arXiv*, 0908.0292v1 [cond-mat.mes-hall] (2009).
2. C. Latta, A. Hoge, **Y. Zhao**, A. N. Vamivakas, P. Maletinsky, M. Kroner, J. Dreiser, I. Carusotto, A. Badolato, D. Schuh, W. Wegscheider, M. Atatüre, and A. Imamoglu. Confluence of resonant laser excitation and bidirectional quantum-dot nuclear-spin polarization. *Nature Physics*, advance online publication, 10.1038/nphys1363. (2009).
3. A. Nick Vamivakas\*, **Yong Zhao\***, Chao-Yang Lu and Mete Atatüre, “Spin-resolved quantum-dot resonance fluorescence”, *Nature Physics*, **5**, 198 (2009).
4. Stefan Falt, Mete Atatüre, Hakan E. Tureci, **Yong Zhao**, Antonio Badolato, and Atac Imamoglu. Strong electron-hole exchange in coherently coupled quantum dots. *Physical Review Letters*, **100**, 106401 (2008).
5. Zhen-Sheng Yuan, Yu-Ao Chen, Shuai Chen, Bo Zhao, Markus Koch, Thorsten Strassel, **Yong Zhao**, Gan-Jun Zhu, Jorg Schmiedmayer, and Jian-Wei Pan. Synchronized Independent Narrow-Band Single Photons and Efficient Generation of Photonic Entanglement. *Physical Review Letters* **98**, 180503 (2007).

\*These authors contributed equally to this work.



# Acknowledgement

Right this moment, I would like to express my deep appreciation to my supervisors, my colleagues and my family for their guidance, trust, support and love during my three years journey for pursuing the degree of Doctor in Natural Sciences.

I would like to express my gratitude to Prof. Jian-Wei Pan for his continuous guidance, support and steady trust through this three years. He taught me with wisdom, rich knowledge, insight and a deep understanding of physics. More over, at every important moment of my study, life, even the future career, Prof. Pan is always willing to give me his great advice and encouragement.

I am indebted to Dr. Mete Atatüre, my second supervisor. He treat me not only as his first PhD student, but also as his friend and even his younger brother. The two-year study with him in Cavendish Lab is the most fruitful period I ever have. The most efficient way for me to get more understanding in physics is to chat with him. Not only the physics, he also passed me his enthusiasm and commitment to the research. What I have learnt from him will definitely deeply influence my future life.

I am very grateful to Prof. Atac Imamoglu for offering me the opportunity to get my first knowledge of quantum dots in Quantum Photonic group in ETH. I also especially thank Prof. Peter Schmelcher and Prof. Peter Michler to be my examiners of my viva.

I will never forget the members of our AMOP/MESS group in west Cambridge. Dr. Nick Vamivakas and Chaoyang Lu are my best buddies in quantum dots subject. Without their helps, none of the results in this thesis can be achieved. I would like to thank Dr. Laurent Lombez and Dr. Yury Alaverdyan for sharing their knowledge, research experience and delighted time with me. I would also like to thank Tina Muller and Clemens Matthiesen for their kind helps in the lab work and on the revision of my thesis.

My deep appreciation also goes to my former and present colleagues in QUO

group in Physikalisches Institut, Uni. Heidelberg. I want to thank Prof. Shuai Chen, Dr. Zhen-Sheng Yuan, Dr. Yu-Ao Chen, Dr. Bo Zhao, Prof. Kai Chen, Prof. Youjin Deng, and Dr. Thorsten Strassel for insightful discussions about my project. I especially thank Dr. Fan Yang, Xiaohui Bao, Dr. Cheming Lee and Xiaofan Xu for their assistance and support during my thesis writing.

For the colleagues outside the institute, I want to thank Dr. Stefan Fält and Dr. Antonio Badolato for tutoring me in the cleanroom and sharing their expertise.

I would also like to send my many thanks to Mrs. Claudia Wallenwein, Mrs. Anna Schmadel, Mrs. Gesine Heinzelmann and Mrs. Pam Hadder for their continuous administration helps throughout years.

Finally and most importantly, I would like to thank my family, my wife Ya Su and my parents for their patience, understanding, endless love and support, without them I would have never made it this far and would have never been able to face any kinds of challenges fully with courage and confidence.